

# **Magnetic flux emergence in the solar photosphere**

Dissertation  
zur Erlangung des Doktorgrades  
der Mathematisch-Naturwissenschaftlichen Fakultäten  
der Georg-August-Universität zu Göttingen

vorgelegt von  
**Chun Ming Mark Cheung**  
aus Hong Kong

Göttingen 2006

## **Bibliografische Information Der Deutschen Bibliothek**

Die Deutsche Bibliothek verzeichnet diese Publikation in der Deutschen Nationalbibliografie; detaillierte bibliografische Daten sind im Internet über <http://dnb.ddb.de> abrufbar.

D7

Referent: Prof. Dr. F. Kneer

Korreferent: Prof. Dr. M. Schüssler

Tag der mündlichen Prüfung: 27 Februar 2006

Copyright © Copernicus GmbH 2006

ISBN 3-936586-51-9

Copernicus GmbH, Katlenburg-Lindau

Druck: Schaltungsdienst Lange, Berlin

Printed in Germany

# Contents

<b>Contents</b>	<b>3</b>
<b>Summary</b>	<b>7</b>
<b>1 Introduction</b>	<b>9</b>
1.1 Global properties of magnetic flux emergence . . . . .	9
1.2 Small-scale properties of magnetic flux emergence . . . . .	12
1.3 The buoyant rise of magnetic flux tubes . . . . .	14
1.4 Research program of the present thesis . . . . .	15
<b>2 Moving magnetic flux tubes: fragmentation, vortex streets and the limit of the approximation of thin flux tubes</b>	<b>17</b>
2.1 Background . . . . .	17
2.2 Equations, numerical method and initial conditions . . . . .	17
2.2.1 Equations . . . . .	17
2.2.2 Initial conditions . . . . .	18
2.2.2.1 Background stratification . . . . .	18
2.2.2.2 Initial magnetic profile of the flux tube . . . . .	19
2.2.3 Numerical method . . . . .	20
2.2.4 Tracking the flux tube . . . . .	20
2.3 Simulation results . . . . .	21
2.3.1 Dependence on Reynolds number . . . . .	21
2.3.1.1 Structure of the wake . . . . .	22
2.3.1.2 Flux retention and field diffusion . . . . .	23
2.3.2 Dependence of flux retention on twist . . . . .	26
2.3.3 Evolution of twist in the flux tube . . . . .	27
2.4 Comparison with a thin flux tube model . . . . .	28
2.4.1 Thin flux tube model . . . . .	29
2.4.2 Modelling the motion of the main tube . . . . .	32
2.4.3 The asymmetric rise of magnetic flux tubes and their trailing vortex streets . . . . .	34
2.5 Exploring the limits of the thin flux tube approximation . . . . .	35
2.6 Conclusions . . . . .	38

<b>3</b>	<b>Simulation of near-surface convection and the photosphere</b>	<b>41</b>
3.1	The radiative MHD equations . . . . .	43
3.1.1	The equations of magnetohydrodynamics . . . . .	43
3.1.2	Equation of state . . . . .	44
3.1.3	Numerical treatment of the MHD equations . . . . .	44
3.1.4	Radiative Transfer Equation . . . . .	45
3.1.5	Numerical treatment of the RTE . . . . .	47
3.2	Simulation setup . . . . .	48
3.3	Properties of near-surface convection and the photosphere . . . . .	49
3.3.1	Topology of near-surface convection . . . . .	50
3.3.2	Logarithmic temperature and density gradients . . . . .	51
3.3.3	Specific entropy distribution . . . . .	53
3.4	The structure of the reversed granulation in the photosphere . . . . .	55
<b>4</b>	<b>Photospheric flux emergence: 2-dimensional simulations</b>	<b>63</b>
4.1	Simulation setup . . . . .	63
4.1.1	Boundary conditions . . . . .	63
4.1.2	Initial conditions . . . . .	65
4.2	Simulation results . . . . .	66
4.2.1	Dependence of emergence morphology on twist . . . . .	66
4.2.2	Intensification of emerging magnetic fields by radiative cooling . . . . .	69
4.2.3	Dependence of emerged flux on twist . . . . .	72
<b>5</b>	<b>Photospheric flux emergence: 3-dimensional simulations</b>	<b>75</b>
5.1	Simulation setup . . . . .	75
5.1.1	Boundary conditions . . . . .	75
5.1.2	Initial conditions . . . . .	75
5.2	Influence of convection on flux emergence . . . . .	76
5.3	Observational signatures . . . . .	83
5.3.1	Quiescent flux emergence . . . . .	83
5.3.1.1	Surface evolution of emerged field: cancellation, coalescence and secondary emergence . . . . .	87
5.3.2	Emergence of strong magnetic field . . . . .	92
5.3.2.1	The relation between field strength and zenith angle . . . . .	93
5.3.2.2	Anomalous transient dark lane . . . . .	97
5.4	Emergence of an arched magnetic flux tube . . . . .	99
5.4.1	Appearance of bright grains at the footpoints of the loop . . . . .	101
5.4.2	Detection of an ephemeral region . . . . .	106
<b>6</b>	<b>Concluding remarks</b>	<b>113</b>
	<b>Bibliography</b>	<b>115</b>
<b>A</b>	<b>Calculation of important thermodynamic quantities</b>	<b>121</b>
A.1	Specific entropy . . . . .	121
A.2	The Jacobian matrix . . . . .	121
A.3	Specific heats $c_v$ and $c_p$ . . . . .	122



A.4	Adiabatic temperature gradient . . . . .	123
A.5	Chandrasekhar's adiabatic exponents . . . . .	123
<b>B</b>	<b>Diffusion of a magnetic structure with a Gaussian profile</b>	<b>125</b>
<b>C</b>	<b>Magnetic field extrapolation</b>	<b>127</b>
C.1	Potential field . . . . .	127
C.2	Linear force-free field . . . . .	128
	<b>Publications</b>	<b>131</b>
	<b>Acknowledgements</b>	<b>133</b>
	<b>Lebenslauf</b>	<b>135</b>



# Summary

Observations indicate that magnetic fields emerge into the photosphere of the Sun as bundles of magnetic flux, also referred to as magnetic flux tubes. In this dissertation, this phenomenon is studied by means of numerical simulations.

- Idealized two-dimensional magnetohydrodynamics (MHD) simulations of the rise of individual horizontal magnetic flux tubes through an initially static, stratified medium were carried out. The buoyant rise, fragmentation, and vortex shedding of magnetic flux tubes were studied.
- Three-dimensional radiative hydrodynamics simulations were carried out to study the properties and dynamics of near-surface convection and the photosphere in the quiet Sun. The convection zone and the photosphere are, respectively, super- and sub-adiabatically stratified. The granulation pattern of the quiet Sun consists of relatively hot and bright cells (granules) separated by cool and dark intercellular boundaries at optical depth unity. With increasing geometrical height and decreasing optical depth, the pattern of temperature fluctuations reverses, so that the intercellular boundaries become hotter than the cellular regions. This *reversed granulation* pattern results from the radiative heating and cooling of convecting plasma overturning in the stably stratified photosphere.
- To model magnetic flux emergence, we carried out radiative MHD simulations of buoyant magnetic flux tubes, initially embedded in the near-surface layers of the convection zone. The results from the simulations highlight the importance of radiative energy exchange and magneto-convection on the properties of emerging magnetic flux.
- The observational signatures of magnetic flux emergence in our simulations agree qualitatively and quantitatively with observations of emerging flux regions. Flux tubes with a longitudinal flux of about  $10^{18}$  Mx evolve passively with the convective flow and magnetic flux preferentially emerges in the form of horizontal fields through the interior of granules. Within a granulation time scale ( $\sim 5$  min), the emerged flux is expelled to the intergranular downflow network.
- The emergence of an arched flux tube carrying a longitudinal flux of about  $10^{19}$  Mx can lead to the transient appearance of an anomalous dark lane, which has a life time of about 10 min and is spatially coincident with upflows at the emergence site. The appearance of bright grains flanking the ends of the transient darkening is associated with the development of downflows at the photospheric footpoints of the arched flux tube.

- Synthetic magnetograms for the previous emergence event were produced. The appearance of the surface field depends on the spatial resolution and effective noise level in the magnetograms. At a resolution of about 1 Mm, the evolution of the surface flux in the synthetic magnetograms is akin to that of an ephemeral region.

# 1 Introduction

Solar magnetic fields on the surface of Sun exist and evolve over a wide range of length- and time-scales. The most prominent magnetic features on the solar surface are sunspots. Beginning with the work of Schwabe (1843), it has been established that the number of sunspots appearing on the solar surface follows, on average, an 11-year cycle. Our knowledge of the existence of solar magnetic fields began with the work of Hale and his co-workers (Hale 1908, Hale et al. 1919), who used the Zeeman effect to explain the splitting of spectral lines forming in sunspots. Since this discovery, understanding solar magnetism has been, and continues to be, one of the main challenges of astrophysics.

In order to explain solar magnetism, we need to address the questions of the origin of magnetic fields and equally importantly, how the fields appear and then evolve on the solar surface. The study of magnetic flux emergence is key to reaching this goal.

## 1.1 Global properties of magnetic flux emergence

Sunspots do not reside on the solar surface as isolated magnetic structures in a non-magnetic background. Between the sunspot and the quiet Sun, there is a whole hierarchy of magnetic features including pores, micropores, plages and faculae. An *active region* is an extended bipolar configuration on the solar surface resulting from the emergence of magnetic fields. In terms of the amount of magnetic flux in each polarity, there is a continuous spectrum of active region sizes (Hagenaar et al. 2003). Although a partitioning of the flux spectrum for the sake of classification may seem somewhat arbitrary, it allows us to conveniently refer to active regions of different sizes. *Large active regions* have polarities containing a flux of  $5 \times 10^{21} - 4 \times 10^{22}$  Mx and contain sunspots. In large active regions, the magnetic flux is shared amongst a whole hierarchy of magnetic features including spots, pores, micropores, plages and faculae. Large active regions have lifetimes of up to months. *Small active regions*, which contain a flux of  $1 \times 10^{20} - 5 \times 10^{21}$  Mx in each polarity, may consist of pores and smaller magnetic features but lack sunspots. Small active regions may persist for up to days to weeks. *Ephemeral active regions* have even less flux ( $3 \times 10^{18}$  to  $1 \times 10^{20}$  Mx), and have lifetimes of only hours to days (Zwaan 1987). Often, ephemeral active regions are simply referred to as ephemeral regions.

The characteristic timescale for the emergence of flux is only a fraction of the lifetime of an active region. For instance, almost all the flux of a large active regions emerges within the first 4 days of their development (Zwaan 1985, Hagenaar 2001).

Systematic studies of sunspots and active regions reveal important global properties of solar magnetic activity. The following points summarize the observed properties of large and small active regions (excluding ephemeral active regions).

- In the majority of cases, sunspots appear as bipolar pairs. Within an 11-year sunspot cycle, the east-west orientation of bipolar pairs in one hemisphere remains the same. Within the same cycle, sunspot pairs appearing in the northern and southern hemisphere have opposite east-west orientations. In the same hemisphere, the east-west orientation of sunspot pairs reverses during the minimum of the 11-year sunspot number cycle. As such, the magnetic cycle in the Sun has a 22-year period. These results are collectively known as *Hale's polarity laws* (Hale et al. 1919).
- The axis of a sunspot pair is tilted with respect to parallels of latitude, with the leading spot closest to the equator. This is known as *Joy's law* (Hale et al. 1919).
- The appearance of sunspot pairs is confined to two latitudinal bands between  $8^\circ$  and  $27^\circ$  on either side of the equator. At the beginning of each sunspot number cycle, the sunspot pairs tend to appear at higher latitudes. In the course of the sunspot number cycle, the mean appearance latitude of sunspot pairs migrates equatorward (Spörer 1890). A well-known visual expression of this effect is Maunder's (1922) *Butterfly diagram*.
- The amplitude of the 11-year sunspot cycle is modulated. The maximum number of spots during the peak of the cycle, as well as the length of the cycle vary. In particular, historical records show that in the past, there have been time intervals of reduced sunspot number spanning several 11-year periods. The most famous example is the Maunder Minimum, which occurred between the years 1640 and 1710 (Eddy 1976).
- Systematic asymmetries in terms of morphology and proper motion exist between the leading and following polarities of pairs of sunspot groups (Zwaan 1985, van Driel-Gesztelyi and Petrovay 1990, Petrovay et al. 1990).

The small sizes and short life-times of ephemeral active regions make them difficult to identify and to track. To study their global properties, one requires full-disk magnetograms of high resolution and high cadence. As a result, there are very few studies in the literature addressing this problem. Recent studies using data from the Michelson Interferometer (MDI) onboard the *SOHO* spacecraft have provided important information about the global properties of ephemeral regions (Hagenaar 2001, Hagenaar et al. 2003). Hagenaar (2001) performed a study of 38,000 ephemeral regions and found that roughly 60% of the regions follow Hale's polarity law. In comparison, 95% of large active regions follow Hale's law. More recently, Hagenaar et al. (2003) show that the emergence frequency of bipolar regions on the solar surface strongly increases with decreasing flux, a trend that is independent of the phase of the cycle. For instance, ephemeral regions with a flux of  $10^{19}$  Mx are about  $10^4 - 10^5$  times more frequent than active regions with  $10^{21}$  Mx. Over the course of the solar cycle, the emergence frequency of active regions varies. Their analysis suggests that the variation of the emergence frequency of ephemeral regions is in antiphase with the variation of the emergence frequency of larger active regions. Furthermore, the emergence frequency of ephemeral regions varies by a factor of about 1.5 over the cycle, which is about one order of magnitude smaller than the corresponding factor for large active regions.

The fact that almost all large active regions follow Hale's law is suggestive of a global-scale structuring of magnetic fields in the solar interior. Since the period of the magnetic cycle of sunspots is much shorter than the lifetime of the Sun, one is motivated to construct dynamo models to explain the solar cycle. Although a number of models exist, there remains a lack of consensus regarding which type of model provides the most encompassing and robust description (Charbonneau 2005). In addition to the global solar dynamo, it has been proposed that other dynamo mechanisms operate to produce magnetic fields at smaller length scales and shorter timescales. For instance, based on the analysis of ephemeral regions described in the previous paragraph, Hagenaar et al. (2003) proposed a scenario in which ephemeral regions with fluxes below  $30 \times 10^{18}$  Mx originate from a small-scale turbulent dynamo, whose operation is largely decoupled from the global-scale dynamo responsible for large active regions.

With regards to theoretical work which addresses the global-scale evolution of solar magnetic activity, two bodies of work deserve special mention. The first of these, the *flux tube models*, take as their basic assumption that the azimuthal field of the Sun is stored in the form of discrete, toroidal magnetic flux tubes in the overshoot layer underlying the convection zone. A magnetic flux tube is essentially an idealization of a bundle of magnetic flux. As the result of an instability, parts of the flux tube rise towards the surface by means of magnetic buoyancy (Parker 1955). In the case that the cross-sectional radius of the flux tube is much smaller than all the other relevant lengthscales in the system, the flux tube may be described by *Thin Flux Tube Approximation* (Roberts and Webb 1978, Spruit 1981), which models each individual flux tube as a one-dimensional entity (see Section 2.4).

Flux tube models take as the basic assumption the existence of toroidal flux tubes in the overshoot layer. Given such an assumption, this paradigm provides a self-consistent model of storage, instability and eruption of flux tube from the overshoot layer through the convection zone (Schüssler et al. 1994). Numerical simulations of the dynamical evolution of toroidal flux tubes carried out in this framework have been very successful at reproducing, and explaining the emergence latitudes of active regions, their tilt angles as well as the asymmetry between leading and following polarities (D'Silva and Choudhuri 1991, Fan et al. 1993, Moreno-Insertis et al. 1994, Fan et al. 1994, Caligari et al. 1995). In addition, stochastic fluctuations of the field strength of flux tubes stored in the overshoot layer can reproduce time intervals of extended low sunspot number similar to the Maunder Minimum (Schmitt et al. 1996).

The second body of work in the literature that we would like to mention is the class of *surface flux transport models*, which began with the work of Leighton (1964). These models describe the time evolution of the radial component of magnetic fields on the solar surface. The basic building blocks of such models which aim to explain the solar cycle are (1) the emergence of bipolar regions following Hale's law and Joy's law; and (2) the supergranular diffusion of the surface fields. Considering these two effects alone, Leighton (1964) argued that there must be a reversal of the sign of the flux in the polar caps between each 11-year cycle. The reason for this is the preferential cancellation of field of leading polarities on both sides of the equator, which leaves behind a net flux of the following polarity in each hemisphere. The supergranular diffusion of the remnant flux cancels and eventually replaces the polar flux from the previous cycle. Subsequent observational and theoretical work has indeed confirmed this prediction. The additional inclusion of

advection of surface flux by differential rotation and by the poleward meridional flow has improved the correspondence between observation and modelling (see review paper by Sheeley, 2005). By incorporating all these ingredients, surface flux transport models have been successful in reproducing the reversal in the signed flux of the polar caps between successive 11-year cycles (Baumann et al. 2004).

Surface flux transport models and flux tube models are complementary. There exists, however, strong connections between the two. While Joy's law is a *basic assumption* of flux transport models, it is a *consequence* of thin flux tube models. Simulations of rising toroidal flux tubes (for a range of magnetic field strengths) naturally reproduces Joy's law because the Coriolis force rotates the rising loops. Another assumption of flux transport models is that the surface field of active regions be advected by the surface motion in a passive manner. This requires that the field at the surface be *dynamically disconnected* from their roots in the solar interior. The work of Schüssler and Rempel (2005) indicates that the dynamical disconnection process is a robust feature of the post-emergence evolution of active regions. One desirable feature that is common to these two types of models is that they make testable predictions. Neither is tailor-made to describe only solar magnetic activity. While maintaining their basic structures and assumptions, both can be (and have been) applied to model magnetic activity on other stars (Schüssler et al. 1996, Granzer et al. 2000, Schrijver and Title 2001, Schrijver et al. 2003, Holzwarth and Schüssler 2003a,b).

## 1.2 Small-scale properties of magnetic flux emergence

A thorough understanding of the fine structure of solar magnetic fields is as important as an understanding of the dynamics at the global scale. As in the previous section, we first present an overview of observed small-scale phenomena before discussing their underlying theoretical aspects.

Observations of the birth of an active region indicates that the total flux in each polarity of region is not the consequence of the emergence of a coherent, monolithic flux bundle. Rather, it builds up as the result of many small flux bundles emerging simultaneously or in succession. An Emerging Flux Region (EFR) is the area on the solar surface where these emergence events take place (Zirin 1972, Zwaan 1985). The onset of the birth of an active region is characterized by the appearance of a compact and very bright plage. The plage consists of magnetic flux elements of opposite polarity, which move apart at an initial velocity of about  $2 \text{ km s}^{-1}$ . New flux continues to emerge near the polarity inversion line. The orientation of the emerging field is not random. Rather, they are roughly aligned along the axis connecting the two polarities. This regularity leads to an accumulation of flux in both polarities. If sufficient flux has emerged, pores and possibly sunspots appear. These tend to be formed near the leading and following edges of the expanding plage (see Zwaan 1985, and references within).

The granulation pattern in an EFR may appear different than that of the quiet Sun. In quiet-Sun granulation, bright granules correspond to upflows whereas the dark intergranular boundaries are consists of downflow lanes and vertices. Transient dark alignments in the central part of an EFR have been detected in intensity maps of both the continuum and in the cores of photospheric spectral lines (Bray et al. 1984, Brants and Steenbeek



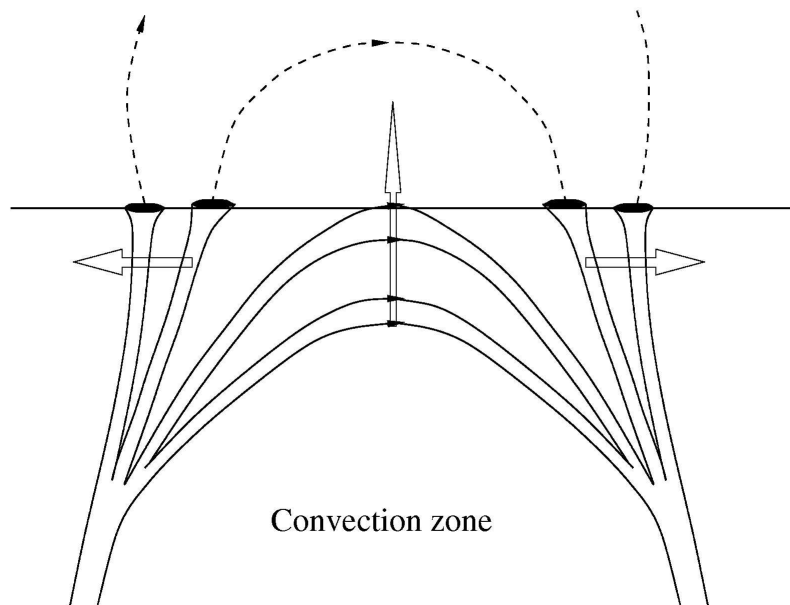


Figure 1.1: Model of an Emerging Flux Region (EFR). In this model, sunspots form as a consequence of the successive emergence of flux bundles at the surface. These flux bundles are connected deeper below the surface (adapted from Zwaan 1985).

1985, Zwaan 1985, Strous and Zwaan 1999). The darkenings are roughly aligned along the axis connecting the two polarities of the active region and typically last about 10 minutes. In the continuum, they are darker than the intergranular boundaries but the spectral lines show upwards Doppler velocities beyond  $0.5 \text{ km s}^{-1}$ . By estimating the diameter and strength of emerging flux bundles that lead to the appearance of dark alignments in an EFR, Brants and Steenbeek (1985) calculated that each bundle contains a longitudinal flux of about  $10^{19} \text{ Mx}$ . This value is in agreement to the estimate given by Born (1974), who inspected the total flux in an active region and counted the number of arch filaments seen in  $\text{H}\alpha$ .

On the basis of the observations previously summarized, Zwaan (1978, 1985) constructed a heuristic model of an EFR at and below the solar surface. Fig. 1.1 shows a sketch adopted from his model. In this figure, the solid arrows show the orientation of field lines and the outlined arrows show the motion of flux tubes. In his model, flux emerges as a collection of arched flux tubes rising through the convection zone. Deep in the convection zone, the flux tubes connect to the same roots. Near the surface, however, they are separated from each other. In this model, the transient dark alignments in the observations correspond to positions where the apices of the flux tubes emerge at the surface. In his interpretation, the alignments are dark because the horizontal magnetic fields suppress turbulent heat exchange. After the horizontal top of a tube has emerged,

the photospheric footpoints of the tubes separate and the field at the footpoints become increasingly vertical. The coalescence of the vertical flux elements in each polarity may lead to sufficient flux to be accumulated for the formation of pores and sunspots.

Subsequent observations of EFRs tend to support many aspects of Zwaan’s heuristic model. Strous and Zwaan (1999) performed a statistical analysis of over two hundred emergence events in a single EFR. They found that emerging flux is characterized by the transient appearance of dark alignments between the polarities. Often, they observed the appearance of faculae at the ends of the dark alignments. The faculae are typically associated with downflows. More recently, full Stokes observations carried out by Lites et al. (1998) and by Kubo et al. (2003) have supported a number of aspects of Zwaan’s model. They report the detection of horizontal fields with strengths of about 200 – 600 G. As the newly emerged flux move away from the emergence site, the fields become vertical and obtain strengths in excess of 1,000 G.

As pointed out by Schüssler (1990), magnetic fields that have just emerged at the surface are initially in a dynamical state. *Flux expulsion* (see Schüssler 1990, and references within) sweeps the emerged magnetic flux from the granules to the intergranular downflow network, leading to an intensification of the magnetic field. Due to the presence of radiative cooling, the intensification of the field is not limited by the equipartition value (at the surface,  $B_{\text{eq}} = v\sqrt{4\pi\rho} \approx 450 - 700$  G) of the convective flow. The cooling of the magnetic region in an intergranular downflow accelerates the downflow, which further increases the magnetic field strength. This mechanism makes it possible for the magnetic fields to reach superequipartition field strengths in the kilogauss range.

### 1.3 The buoyant rise of magnetic flux tubes

As the observations at global scales and at smaller scales indicate, the most conspicuous form of flux emergence at the photosphere is due to the arrival of coherent magnetic flux bundles at the surface. This motivates the investigation of the detailed dynamics related to the rise of buoyant magnetic flux tubes.

At present, the demand on computational resources is still far too great to carry out realistic 3-dimensional magnetohydrodynamic (MHD) simulations of a flux tube rising across the convection zone until it emerges at the photosphere, even more so if one wants to include its further rise into the upper solar atmosphere. This is due to the extremely wide range of length and time scales involved in the process and to the complicated mixture of physical phenomena associated with the rise of the tube in its different phases (e.g., turbulent convection, radiative transfer, magnetic reconnection). A possibility to make progress in spite of these limitations is to perform idealized simulations to address different aspects of the problem separately.

A branch in this undertaking is devoted to the basic magnetohydrodynamics of buoyant flux tubes rising in stratified and (otherwise) unmagnetized media studied by way of 2D or 3D numerical experiments (see review by Fan, 2004). One example is an initially horizontal magnetic flux tube embedded in a stratified layer. The tube is endowed with a density deficit with respect to the surroundings, so that it rises and, in doing so, it expands, displaces the surrounding medium and develops a trailing wake. A number of results, obtained mostly for 2D (more precisely, 2.5D) configurations, concern the conversion of the

rising magnetic tube into pairs of vortex tubes. These experiments focus on the evolution in a vertical plane normal to the axis of the tube and use the simplifying assumption of independence of all quantities (scalars or vectors) with respect to the coordinate along that axis. When the magnetic field in the horizontal tube is purely longitudinal (i.e., has no components in the plane normal to the tube axis), an initially cylindrical tube, after rising a height equivalent to a few times the tube diameter, splits into two roughly mirror-symmetric vortex rolls. The rolls have vorticity of opposite signs pointing in the direction of the tube axis and separate horizontally from each other. This behavior had been noted in an early paper by Schüssler (1979) and was analyzed by Longcope et al. (1996) who showed that the motion of the resulting vortex tubes could be explained as a result of the combined action of the buoyancy and lift forces on them.

Another branch of study has been the emergence of magnetic flux tubes into the solar atmosphere. Since Forbes and Priest (1984) and Shibata et al. (1989), a substantial body of work has appeared in the literature presenting results of magneto-hydrodynamics (MHD) simulations of this phenomenon. The focus of most studies in the literature has been on the evolution of the emerging magnetic field in the chromosphere and in the corona. Typically, these simulations ignore convection as well as energy exchange via radiative transfer in the underlying layers. Nevertheless, simulations of flux emergence into the corona have been successful in reproducing many observed features (see, for example Archontis et al. 2004, Isobe et al. 2005).

This dissertation focuses on a different aspect of the problem. We wish to study in detail the effects of convecting flows and radiative transfer on emerging magnetic flux. To this end, we restrict our attention to flux emergence from the near-surface layer of the convection zone into the photosphere.

## 1.4 Research program of the present thesis

This thesis presents an investigation of the emergence of magnetic flux into the photosphere. As explained in the preceding discussion, the study of the global properties as well as the fine structure of flux emergence is important for our generally understanding of solar magnetism. We take a step-wise approach to help us study the many aspects of the problem.

The rest of the thesis is structured as follows. In Chapter 2, we present a study of the rise of magnetic flux tubes in an idealized stratified layer by means of two-dimensional MHD simulations. Special emphasis is placed on studying the fragmentation of the rising tube, its trailing wake and the formation of a vortex street in the high-Reynolds number regime. Furthermore, we evaluate the relevance of the thin flux tube approximation with regards to describing the evolution of magnetic flux tubes in the simulations.

Before we proceed to study flux emergence in the photosphere, it is important that we are familiar with the properties of the quiet Sun. In Chapter 3, we study the properties of the photosphere as well as the near-surface layers of the convection zone in the absence of magnetic fields. This is done by means of carrying out a radiative hydrodynamics simulation using the *MPS/University of Chicago Radiative MHD* code (Vögler 2003, Vögler et al. 2005). This code allows us to realistically model those layers in the Sun by treating the effects of radiative transfer and partial ionization. After a description of the

governing equations and the numerical methods implemented in MURaM to solve these equations, we present an analysis of the properties of the quiet-Sun atmosphere. One of the topics treated is the structure of the reversed granulation of the photosphere.

In Chapter 4, we present results from two-dimensional simulations of flux emergence into the photosphere. Emphasis is placed on studying the effect of radiative cooling on an emerging flux tube. To simplify the analysis, the simulations neglect the presence of convective flows.

In Chapter 5, we finally include the effects of convection. This chapter presents results of the emergence of buoyant magnetic flux tubes initially embedded in the vicinity of convecting plasma in the sub-surface layers. The results are directly compared with emerging flux observations.

# 2 Moving magnetic flux tubes: fragmentation, vortex streets and the limit of the approximation of thin flux tubes

## 2.1 Background

The objective of the present study is to carry out 2.5D numerical experiments of the rise of a buoyant horizontal magnetic flux tube in a stratified medium using a state-of-the-art AMR code (the FLASH code) and profiting from the unprecedented computational power allowed by today's massively parallel computers. The chapter is organized as follows. In Section 2.2, we present details of the simulation setup, including the system of equations solved, the numerical method used, initial conditions of the simulation. Additionally, in Section 2.2.4, we present the method used to track the flux tube. In Section 2.3, the results from the 2.5D simulations are presented. The following aspects of the simulations are discussed: dependence on Reynolds number (Section 2.3.1), the dependence of the flux retention on twist (Section 2.3.2) and the evolution of the twist in the tube (Section 2.3.3). In Section 2.4, we use a thin flux tube model to explain the evolution of the flux tube as it rises through the stratified layer. In Section 2.5, we explore the transition from the thin flux tube regime to the thick flux tube regime. Finally, in Section 2.6 we discuss possible implications for understanding real magnetic flux tubes in the solar interior.

## 2.2 Equations, numerical method and initial conditions

### 2.2.1 Equations

The medium is taken to be a compressible, electrically conducting ideal gas with the equation of state:

$$p = R\rho T, \tag{2.1}$$

where  $R = R^*/\bar{\mu}$  is the individual gas constant and  $\bar{\mu}$  the mean molar mass. The time evolution of the system is governed by the ideal magnetohydrodynamics equations:

$$\frac{\partial \rho}{\partial t} + \nabla \cdot (\rho \vec{v}) = 0, \quad (2.2)$$

$$\frac{\partial(\rho \vec{v})}{\partial t} + \nabla \cdot \left( \rho \vec{v} \otimes \vec{v} - \frac{1}{\mu_0} \vec{B} \otimes \vec{B} \right) + \nabla p_{\text{tot}} = \rho \vec{g}, \quad (2.3)$$

$$\frac{\partial(\rho e)}{\partial t} + \nabla \cdot \left( \vec{v}[\rho e + p_{\text{tot}}] - \frac{1}{\mu_0} \vec{B}[\vec{v} \cdot \vec{B}] \right) = \rho \vec{g} \cdot \vec{v}, \quad (2.4)$$

$$\frac{\partial \vec{B}}{\partial t} + \nabla \cdot (\vec{v} \otimes \vec{B} - \vec{B} \otimes \vec{v}) = 0, \quad (2.5)$$

$$(2.6)$$

where  $\vec{v} \otimes \vec{v}$ ,  $\vec{B} \otimes \vec{B}$  etc. denote dyadic products and

$$p_{\text{tot}} = p + \frac{B^2}{2\mu_0}, \quad (2.7)$$

$$e = \frac{1}{2}v^2 + \epsilon + \frac{1}{\rho} \frac{B^2}{2\mu_0} \quad (2.8)$$

are total pressure and total specific energy.  $\epsilon$  is the specific internal energy. The solenoidal condition  $\nabla \cdot \vec{B} = 0$  applies as an initial condition. These equations are valid in the absence of thermal, viscous and Ohmic diffusion.

## 2.2.2 Initial conditions

### 2.2.2.1 Background stratification

A hydrostatic, adiabatically stratified polytropic layer of ideal monatomic gas was chosen as the initial background stratification. This initial polytropic layer is described by the following temperature, density and pressure profiles:

$$T(y) = T_0 \left[ 1 + \frac{\nabla_{\text{ad}}}{H_{p0}}(d - y) \right], \quad (2.9)$$

$$\rho(y) = \rho_0 \left[ 1 + \frac{\nabla_{\text{ad}}}{H_{p0}}(d - y) \right]^{1/\nabla_{\text{ad}} - 1}, \quad (2.10)$$

$$p(y) = p_0 \left[ 1 + \frac{\nabla_{\text{ad}}}{H_{p0}}(d - y) \right]^{1/\nabla_{\text{ad}}}, \quad (2.11)$$

where  $y$  is the height coordinate,  $d$  the thickness of the layer, and  $T_0$ ,  $\rho_0$ ,  $p_0$  and  $H_{p0}$  are the temperature, density, gas pressure, and pressure scale height at the top boundary ( $y = d$ ), respectively. The logarithmic temperature gradient is  $\nabla = \nabla_{\text{ad}} = (d \ln T / d \ln p)_s = 1 - 1/\gamma_2$ .  $\gamma_2$  is Chandrasekhar's second adiabatic exponent (Chandrasekhar 1957). For the case of a completely ionized or completely neutral, monatomic gas,  $\gamma_2 = 5/3$ . An adiabatic stratification was chosen because it is neutral to motions induced by the rise of the flux tube. This is, of course, an idealization of what happens in the solar convective zone. However, here we are interested in studying the rise of the tube purely by its own

buoyancy. Furthermore, for  $B \gg B_{\text{eq}}$ , where  $B_{\text{eq}}$  is the equipartition field strength with respect to the convective flows, we can safely neglect the effects of the external convection on the rise of the tube.

We choose to use  $\rho_0$ ,  $p_0$  and  $H_{p0}$  as units for the density, pressure and length respectively.  $RT$  is used as the temperature variable. The units for the velocity and time  $c_0 = \sqrt{p_0/\rho_0}$  (the isothermal sound speed at the top of the layer) and  $t_0 = H_{p0}/c_0$  respectively. The unit for specific energies is  $e_0 = p_0/\rho_0$  and the unit for the magnetic field is  $B_0 = \sqrt{2\mu_0 p_0}$ . Expressed in these units, the initial polytropic profiles (2.9) to (2.11) become

$$\tilde{T}(\tilde{y}) = [1 + (\tilde{d} - \tilde{y})\nabla_{\text{ad}}], \quad (2.12)$$

$$\tilde{\rho}(\tilde{y}) = [1 + (\tilde{d} - \tilde{y})\nabla_{\text{ad}}]^{1/\nabla_{\text{ad}}-1}, \quad (2.13)$$

$$\tilde{p}(\tilde{y}) = [1 + (\tilde{d} - \tilde{y})\nabla_{\text{ad}}]^{1/\nabla_{\text{ad}}}, \quad (2.14)$$

where the tilde denotes a quantity expressed in these units. In what follows, all quantities are expressed in terms of these units and we drop the tilde from all the symbols. Quantities inside the flux tube are denoted with a subscript  $i$  and quantities outside the flux tube have no subscripts. For example,  $T$  and  $T_i$  refer to the temperature outside and inside the flux tube respectively. From here on, the symbol  $H_p$  always refers to the local pressure scale height.

In the simulations presented in Section 2.3, the polytropic layer is enclosed in the region  $x \in [-10, 10]$  and  $y \in [0, 35]$ . Therefore the density and pressure contrasts between the bottom and top of the polytropic layer are 58 and 871 respectively. The number of pressure scale heights spanned over the height of the layer is  $N_p = \int dy/H_p = 6.77$ . This is comparable to the number of pressure scale heights spanned between the bottom of the solar convection zone (at depth of 200 Mm) and a depth of about 20 Mm. Thin flux tube simulations of flux tubes carrying magnetic flux comparable to active regions ( $\Phi = 10^{20} - 10^{22}$  Mx) are considered to yield reliable results up to a depth of about 10 Mm. Above that depth, the radii of these flux tubes become comparable to the local  $H_p$ . The number of pressure scale heights between a depth of 200 Mm to 10 Mm is  $N_p \approx 16$ .

### 2.2.2.2 Initial magnetic profile of the flux tube

The initial flux tube is taken to be axisymmetric. In cylindrical coordinates, the longitudinal and azimuthal components of its magnetic field have the form:

$$B_l(r) = B_0 \exp(-r^2/R_0^2), \quad (2.15)$$

$$B_\theta(r) = \frac{\lambda r}{R_0} B_l, \quad (2.16)$$

where  $r \in [0, 2R_0]$  is the radial distance from the tube axis,  $R_0$  is the characteristic radius of the flux tube and  $\lambda$  is the dimensionless twist parameter. For  $r > 2R_0$ , the magnetic field is zero. As such, a twisted magnetic flux tube of this form carry no net current. We note that the parameter  $q$  used by Linton et al. (1996) and Fan et al. (1998b) is equivalent to  $\lambda/R_0$ . At  $r = R_0$ , the pitch angle is given by  $\tan \Psi = (B_\theta/B_l)|_{R_0}$ . The total initial longitudinal flux of the tube is  $\int B_l dA = 0.98\pi R_0^2 B_0$ .



For each simulation, a flux tube was inserted near the bottom of the stratified layer at time  $t = 0$ . We have carried out a number of simulations with different values of  $R_0$  and  $\lambda$ .

### 2.2.3 Numerical method

We have chosen to use the FLASH code for carrying out the simulations. This code implements a Riemann solver that is formally second-order accurate in time and space. The advective terms are discretized using a slope-limited Total Variation Diminishing (TVD) scheme and time-stepping is performed using an explicit, Hancock-type scheme (Toro 1997). The system of equations is solved on a 2D grid with cartesian geometry.

As mentioned in § 2.2.1, the MHD equations (3.2)-(3.1) do not take into account the effects of thermal, viscous and Ohmic diffusion. In practice, however, such non-ideal effects are always present in simulations as a result of numerical diffusion. Of course, if diffusive effects are actually important for the problem of interest, diffusive terms can be added to the MHD equations to capture the relevant physics. In astrophysical problems, one often encounters situations with very large dynamic and magnetic Reynolds numbers. This is also the case for the solar interior. As such, we have chosen not to impose explicit diffusive terms in the MHD equations. Diffusive effects in the following simulations are purely numerical. The amount of numerical diffusion present in the simulation is dependent on the numerical resolution used. The higher the numerical resolution, the smaller is the amount of numerical diffusion and the larger are the effective Reynolds numbers. Since the initial state of the background atmosphere in our problem is uniform (except for small pressure perturbations) in the horizontal direction and smoothly varying in the vertical direction, only relatively large grid spacing is required to resolve regions far away from the flux tube. On the other hand, high spatial resolution is needed to resolve the small-scale features at the interface between the tube and its surroundings (e.g., in regions where the flux tube fragmented).

The numerical resolution we can use is limited by the computational resources available. To get the highest numerical resolution where we need it, we made use of the Adaptive Mesh Refinement (AMR) feature in FLASH. The cartesian domain is comprised of adjacent square blocks, each consisting of  $8 \times 8$  grid cells. At each time-step, all the blocks are checked to determine if the block should be refined. If the normalized second-order spatial derivative of the absolute field strength,  $|B|$ , exceeds some fixed threshold in any grid cell, the resolution of the corresponding block is doubled by interpolation and the original block is split into four sub-blocks, increasing the ‘refinement level’ of the original block by one. The reverse process (coarsening) occurs when the normalized second-order spatial derivative of  $|B|$  is smaller than some threshold for all four sub-blocks. Then the resolution of each sub-block is halved and the sub-blocks are merged.

For further details on the FLASH code, the reader is referred to the FLASH user manual (ASCI Center for Thermonuclear Flashes, 2003).

### 2.2.4 Tracking the flux tube

In the simulations discussed here, the initial flux tube does not remain a single, monolithic structure as it rises to the top. From the results of the literature (Emonet and Moreno-



Insertis 1998, Fan et al. 1998a, Hughes and Falle 1998), we expect the tube to fragment and lose flux by means of vortex shedding. However, for a sufficiently high level of field line twist, a central portion of the tube retains its identity throughout the simulation. We refer to this central flux filament as the ‘main tube’. To track the main tube, we make use of the flux function:

$$\psi(x, y) = \int_0^x B_y(x', y) dx' - \int_0^y B_x(x, y') dy'. \quad (2.17)$$

Field lines traced out by the transverse field  $(B_x, B_y)$ , when projected onto the  $x - y$  plane, correspond to contours of  $\psi$ . For the initial axisymmetric flux tube, the contours are a family of concentric circles corresponding to the planar projection of the twisted field lines that wind around the tube axis. Let us call one of these circles  $C$ . The initial magnetic flux inside this structure is given by  $\Phi_0 = \int_C B_z dA$ . To identify this structure at a later time, we calculate  $\psi$  for that time and find the contour(s)  $\partial C'$  satisfying the flux conservation criterion  $\Phi_t = \int_{C'} B_z dA = \Phi_0$ . If the structure has broken up, then the contours will be a set of closed curves and the sum of the fluxes enclosed in these curves is  $\Phi_0$ .

If we arbitrarily chose a value of  $\Phi_0$  to define the main tube, we have no guarantee that at a later time, the structure we track remains coherent. In order to define a coherent main tube, we reverse the aforementioned procedure. At the end of a simulation (i.e. when the main flux structure has reached the top of the domain),  $t = t_1$ , we calculate  $\psi(x, y)|_{t_1}$ . We test different contour levels  $\psi_0 = \psi|_{t_1}$ . If the contours corresponding to a particular value of  $\psi_0$  consists of more than one closed loop, we dismiss them. For the remaining values of  $\psi_0$  (each of which has only one corresponding closed curve), we pick the one that encloses the maximum amount of flux ( $\Phi_{\text{MT}}$ ). This is defined as the main tube for this particular simulation. To back-track the main tube at earlier times, we simply calculate  $\psi$  for that time. Then the contour which encloses a flux equal to  $\Phi_{\text{MT}}$  represents the main tube at that time.

The centre of the main tube is located at the extremum of  $\psi$  (maximum or minimum depending on whether the tube has right or left-handed twist). Although the main tube is, in general, not circular, we can define an effective radius,

$$r_{\text{eff}} = \sqrt{\int_C dA/\pi}, \quad (2.18)$$

which gives a useful measure of its size.

## 2.3 Simulation results

We have carried out a number of simulations in order to study different aspects of the problem of the buoyant rise of magnetic flux tubes. Various aspects of the results are discussed in the following sections.

### 2.3.1 Dependence on Reynolds number

From the same initial setup, we have carried out simulations with different levels of grid refinement in order to study how the numerical resolution influences the outcome of the

Run	Effective resolution	$Re$
A1	$256 \times 448$	25
A2	$512 \times 896$	140
A3	$1024 \times 1792$	630
A4	$2048 \times 3584$	2600

Table 2.1: Simulations runs out carried to study the dependence of the simulation result on numerical resolution (and hence Reynolds number).

simulation. The initial condition is as follows: a flux tube was inserted near the bottom of the polytropic atmosphere at  $(x_0, y_0) = (0.0, 2.5)$  at  $t = 0$ . The flux tube has  $R_0 = 0.5$  (corresponding to 4% of the local pressure scale height),  $\beta_0 = 15$  and  $\lambda = 0.25$ . The material inside the tube has the same entropy as the external atmosphere, so that it is buoyant. We carried out four runs from this initial condition. Run A1 has the lowest effective resolution. If the simulation domain was fully refined, the domain would be spanned by  $256 \times 448$  grid cells in the  $x$  and  $y$  directions. Runs A2, A3 and A4 have 2, 4 and 8 times the effective resolution of A1 respectively. Table 2.1 gives the effective resolution and effective Reynolds numbers ( $Re$ ) for each of the runs. The latter is defined as

$$Re = \left( \frac{D}{L_{bl}} \right)^2, \quad (2.19)$$

where  $D$  is the flux tube diameter and  $L_{bl}$  is the width of the boundary layer between flux tube and its surroundings.

Figure 2.1 shows the distribution of the longitudinal field ( $B_z$ ) over the entire domain at  $t = 200$  for all four runs. Figure 2.2 shows the  $z$  component of the vorticity ( $\omega_z$ ) at the same time. To emphasize the difference in resolution between the runs, the axes are labelled in terms of grid-points. To calculate  $Re$ , we examined the profiles of  $B_z$  and  $\omega_z$  near the vertical  $x = 0$  for each of the runs at  $t = 200$ . From the  $B_z$  profile we can find the tube diameter  $D$ . From the corresponding  $\omega_z$  profile, we identify a thin boundary layer near the apex of the tube. The left and right halves (about  $x = 0$ ) of this boundary layer have opposite sign. The thickness of this boundary layer - which is the site of vorticity generation - corresponds to  $L_{bl}$ . Inspection of the vertical profile of the magnetic field along  $x = 0$  gives the distance over which the magnetic field goes to zero above the tube apex. This gives the thickness of the magnetic boundary layer. For the simulations in this study, we found that the magnetic and viscous boundary layers have similar thickness, about 6 grid cells, indicating that the magnetic Reynolds number  $Re_m \sim Re$ . This is not a coincidence, since the viscous and magnetic diffusion stem from diffusion inherent in the numerical scheme.

### 2.3.1.1 Structure of the wake

The structure of the wake depends on the Reynolds number. At  $Re = 25$  (top left panel of Figs. 2.1 and 2.2), we identify two coherent counter-rotating vortex rolls in the wake. These types of wake structures have been reported in past studies of rising magnetic flux tubes (Schüssler 1979, Longcope et al. 1996, Moreno-Insertis and Emonet 1996, Emonet and Moreno-Insertis 1998). A similar pair of vortex rolls is also found in the wake of

the flux tube for the run with  $Re = 140$ . In this case, however, the rolls have more internal structure. Fig. 9 of Emonet and Moreno-Insertis (1998) shows similar plots of vorticity for a rising twisted flux tube. We note that the vorticity distribution shown in the rightmost panel of their figure very much resembles our case for  $Re = 140$ . However, the vortex rolls in their figure also show signs of breakup into smaller vortex rolls. At higher  $Re$  ( $Re = 630$  and  $Re = 2600$  in runs A3 and A4 respectively), the breakup of the vortex rolls is even more obvious. In these two cases, each roll is replaced by a group of secondary rolls with the same sign in vorticity. This indicates that the shedding of material at high Reynolds number occurs in a much more intermittent fashion than in cases with low  $Re$ .

### 2.3.1.2 Flux retention and field diffusion

The fraction of magnetic flux retained by the head of the flux tube (i.e. the main tube) also depends on the Reynolds number. Fig. 2.3 shows the flux retained in the main tube at  $t = 280$  for the four different runs (diamonds). Clearly, with increasing  $Re$ , the percentage of flux retained by the main tube increases. At  $Re = 2600$ , the main tube retains 84% of the original flux of the initial tube. Although we cannot conclude from these simulations that the flux retained converges to some value in the limit  $Re \rightarrow \infty$ , Fig. 2.3 does seem to suggest that the curve levels off for increasing  $Re$ .

Emonet and Moreno-Insertis (1998) demonstrated that in a rising, twisted flux tube, vorticity is generated in the magnetic boundary layer between the tube and the surrounding flow. The material in this boundary is then advected towards the wake, leading to a loss of magnetic flux from the tube. We can estimate the flux loss per unit time as

$$-\frac{d\Phi}{dt} = v_{\text{tube}} L_{\text{bl}} B_{\text{bl}}, \quad (2.20)$$

where  $v_{\text{tube}}$  is the relative velocity between the tube and the surroundings and  $B_{\text{bl}}$  is the characteristic value of the longitudinal field in the boundary layer. Making use of Eq. (2.19), and using the approximation that  $Re \approx Re_m$ , we find that

$$-\frac{d\Phi}{dt} = v_{\text{tube}} B_{\text{bl}} \frac{D}{\sqrt{Re}}. \quad (2.21)$$

If one makes the additional assumptions that,  $v_{\text{tube}}$ ,  $D$  and  $B_{\text{bl}}$  do not change much with  $Re$ , then we find that the amount of flux lost from the tube scales as  $O(Re^{-1/2})$ . The amount of flux retained by the main tube, as predicted by this scaling relation, is plotted as a solid line in Fig. 2.3. The value at  $Re = 25$  was used as a reference point for the curve.

In ideal MHD, the ratio of mass and longitudinal magnetic flux enclosed in the main tube,  $M/\Phi$ , should remain constant. In numerical simulations, however, the ratio always increases with time because of some mass diffusion across field lines. The size of this change tells us how well the simulation approximates the ideal MHD case. Fig. 2.4 shows the percentage change of this quantity for the main tube between  $t = 0$  and  $t = 280$ , as a function of  $Re$ . At  $Re = 25$ , the ratio  $M/\Phi$  increased by 44%. This increase in the ratio diminishes for higher resolution. At  $Re = 2600$ , the change is only on the order of 1%. Consequently, in order to compare the results from numerical simulations with predictions

## 2 Moving magnetic flux tubes: fragmentation, vortex streets and the limit of the approximation of thin flux tubes

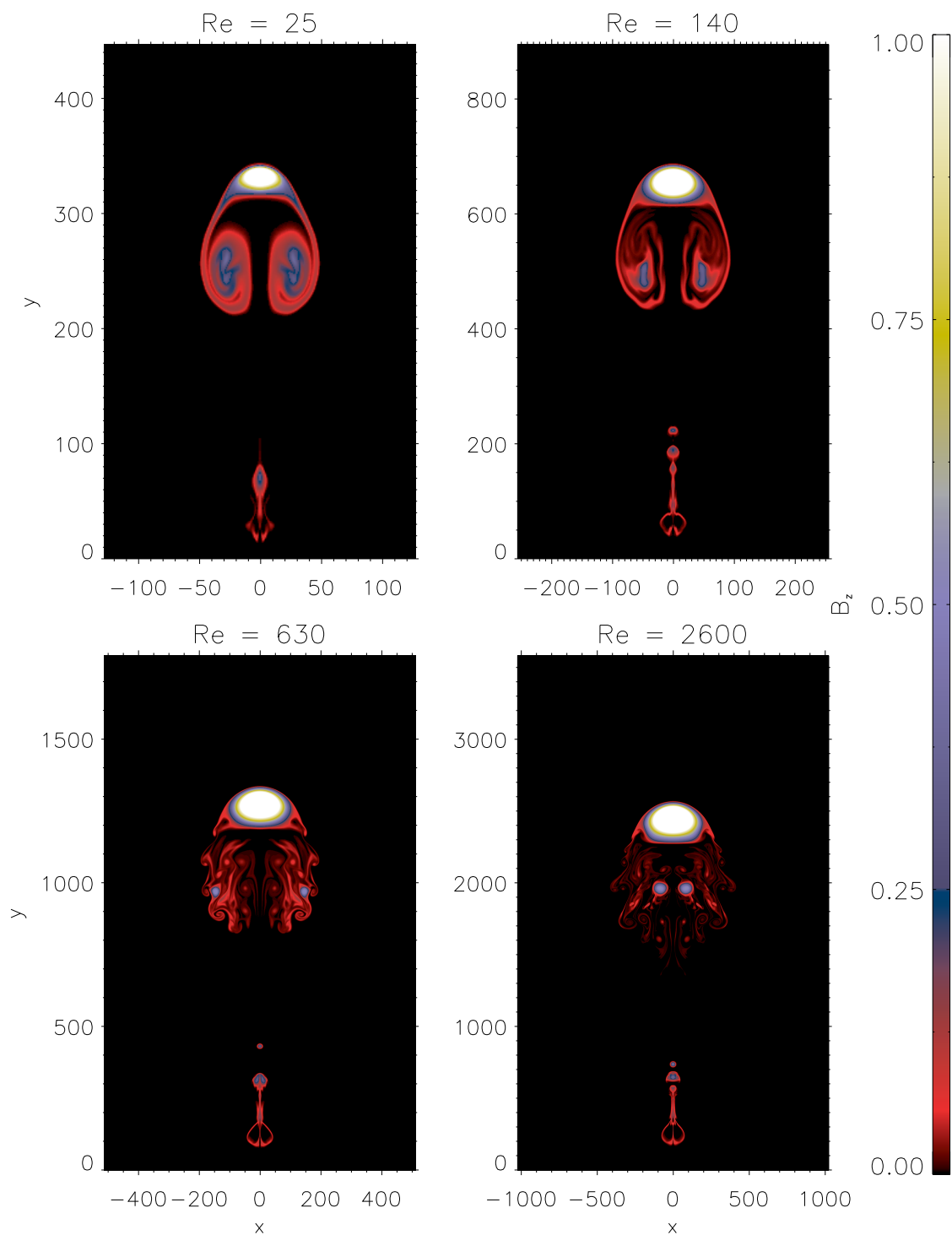


Figure 2.1: The structure of the wake below the rising flux tube depends on the Reynolds number of the flow. The four panels show the distribution of the longitudinal magnetic field at Reynolds numbers ranging from 25 to 2600.

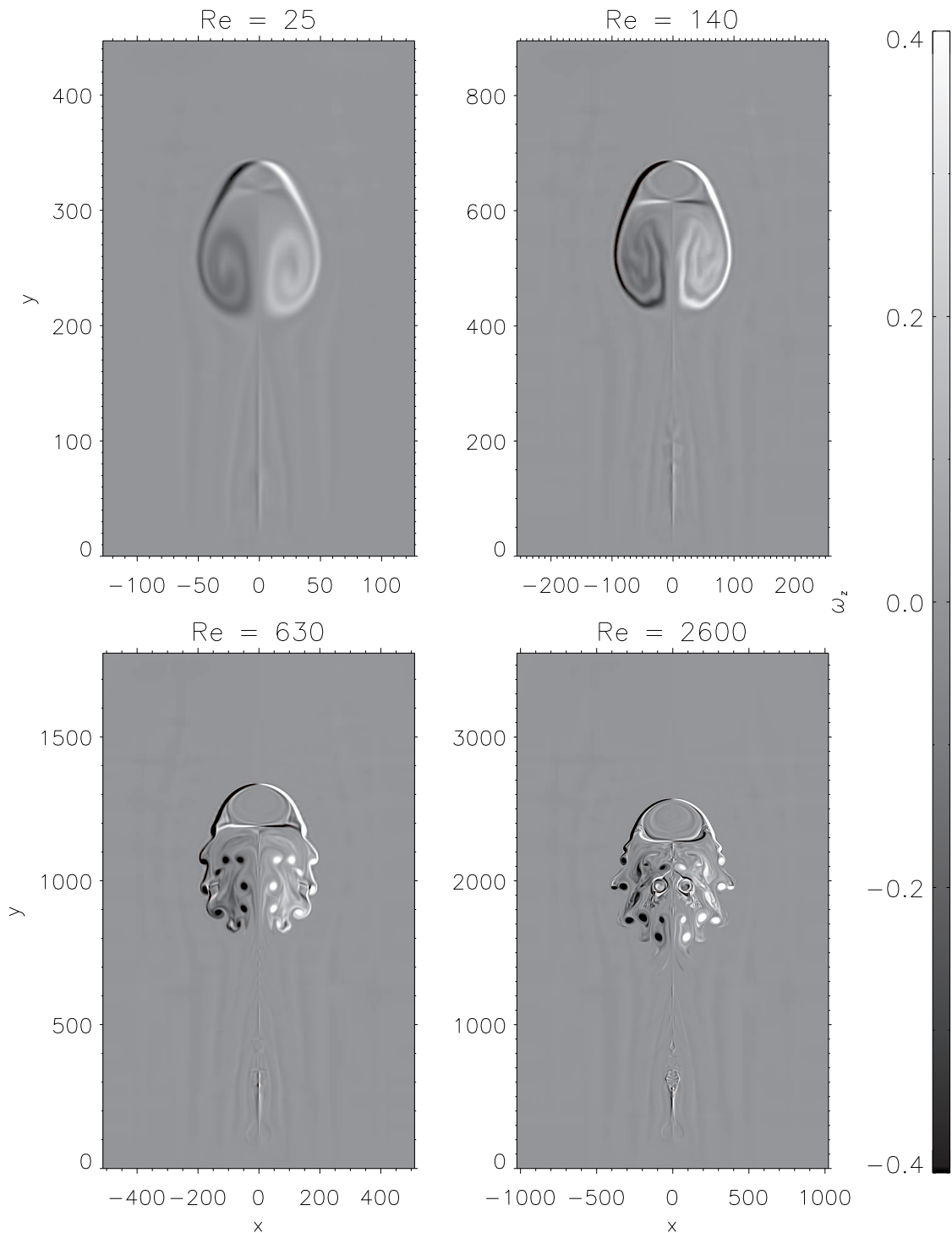


Figure 2.2: Same as Fig. 2.1 but for the  $z$  component of the vorticity. At low Reynolds numbers - see cases with  $Re = 25$  and  $Re = 140$  - the wake consists of two vortex rolls with vorticity of opposite sign. At sufficiently high Reynolds numbers - see cases with  $Re = 630$  and  $Re = 2600$  - the vortex rolls break up and the shedding of vorticity into the wake occurs in a more intermittent fashion.

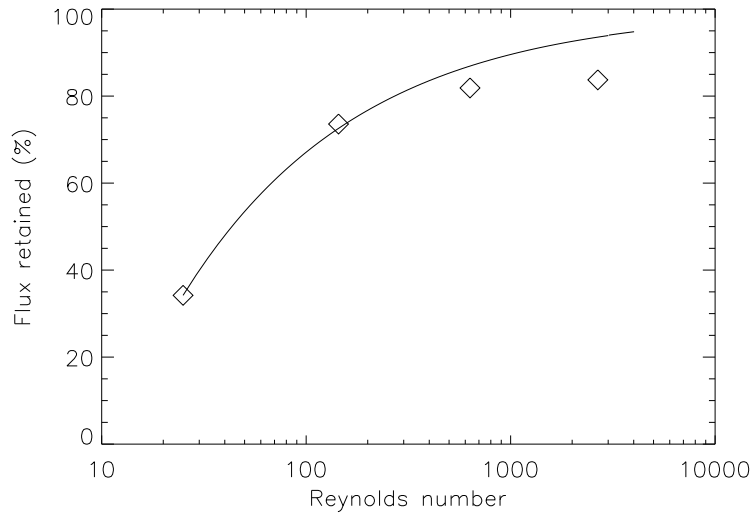


Figure 2.3: Magnetic flux retained in the main tube as a function of the Reynolds number. The diamonds plot the values from simulations A1 to A4. If the amount of flux lost scaled as  $O(Re^{-1/2})$ , it would follow the solid curve.

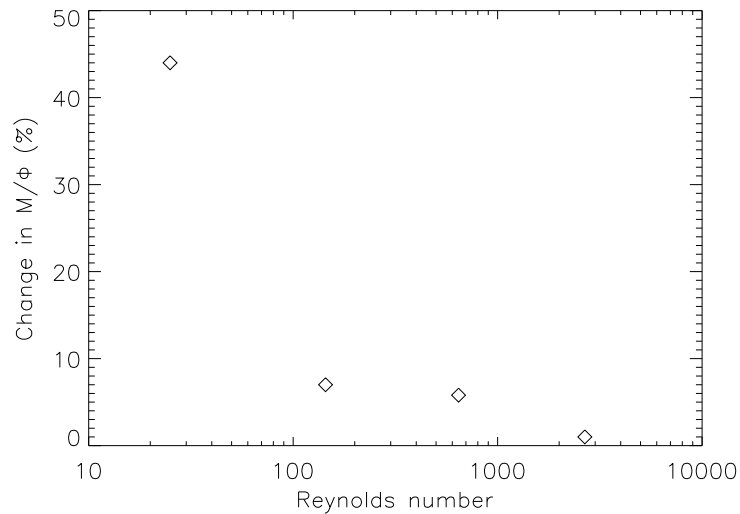


Figure 2.4: The change of  $M/\Phi$  (ratio of enclosed mass and enclosed magnetic flux in the main tube) as a function of the Reynolds number.

in the approximation of thin flux tubes (which assumes ideal MHD), we should take the results from runs with the highest values of  $Re$ .

### 2.3.2 Dependence of flux retention on twist

We carried out a number of simulations to study the dependence of the flux retained in the main tube as a function of the twist parameter  $\lambda$ . These runs have the same resolution as

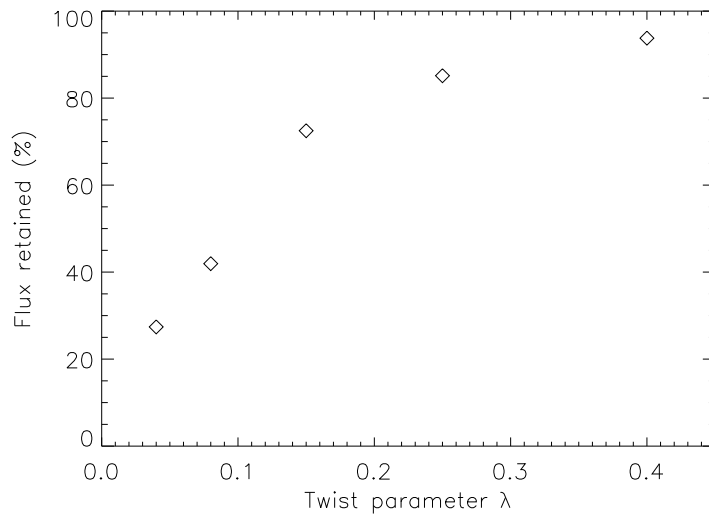


Figure 2.5: The dependence of the twist retained in the main tube as a function of the twist parameter  $\lambda$ .

run A4. We find that a flux tube with no initial twist ( $\lambda = 0$ ), after rising a distance a few times its radius, splits into two counter-rotating vortex rolls, which separate horizontally from each other. This behaviour has already been reported in an early paper by Schüssler (1979). Longcope et al. (1996) showed that this is a result of the combination of the buoyancy and lift forces acting on the flux tube. Our results show that even at the relatively high Reynolds number ( $Re \sim 10^3$ ), the same behaviour is observed.

For magnetic flux tubes with non-zero twist, we were able to track a main tube. Figure 2.5 shows that the amount of flux retained in the main tube at  $t = 280$ . It is a monotonically increasing function of  $\lambda$ , a result consistent with the previous work of Moreno-Insertis and Emonet (1996). Thus, given that a main tube can be tracked, the amount of flux it retains increases with  $Re$ .

### 2.3.3 Evolution of twist in the flux tube

As Parker (1974, 1979) pointed out, the radial expansion (compression) of a twisted flux tube leads to an increase (decrease) of the pitch angle of the field lines. This is a consequence of magnetic flux conservation (Fan et al. 1998b).

The radial profiles of the longitudinal and transverse field we have chosen for the initial flux tube yield a pitch angle of the field lines that depends on radial distance from the axis. A more appropriate measure for the amount of twist in the tube is  $\lambda$ , which is dimensionless and constant over the initial tube. If the flux tube undergoes a homologous expansion (or compression),  $\lambda$  evolves according to

$$\frac{\lambda}{\lambda_0} = \frac{R}{R_0}, \quad (2.22)$$

where the  $\lambda$  and  $R$  are the twist and characteristic radius of the tube, respectively. The subscript 0 denotes their initial values. Eq. (2.22) states that  $q = \lambda/R$  remains constant

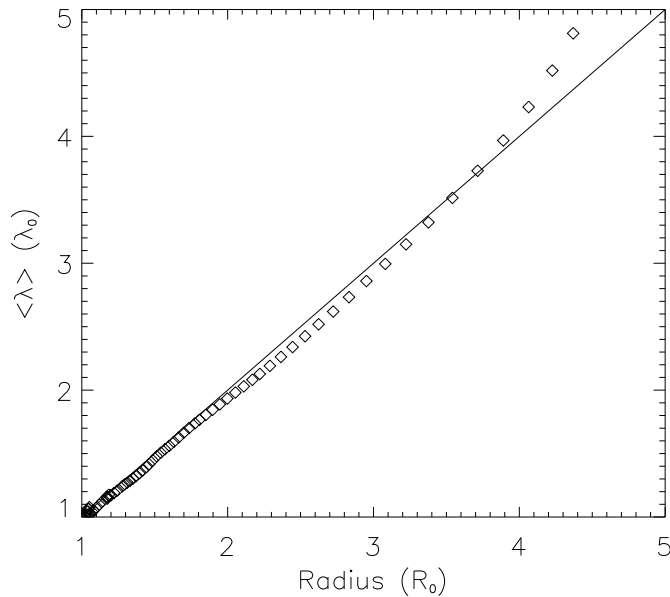


Figure 2.6: The relationship between the tube’s effective radius and its twist  $\lambda$ . The solid line shows the linear relation given by Eq. (2.22). Diamonds denote the evolution of the mean twist  $\langle \lambda \rangle$  of the main tube in run A4. This good match indicates that the main tube expands homologously over most of the tube rise.

as the tube rises (Linton et al. 1996). The second-order thin flux tube approximation also predicts the same result (Ferriz-Mas et al. 1989). In this approximation, an axisymmetric tube has a transverse field  $B_\theta(r) \propto r$ . By virtue of the conservation of the transverse magnetic flux, Eq. (2.22) can be obtained.

In Fig. 2.6, the relationship given by this equation is shown as a solid line. Overplotted (as diamonds) are values of the mean twist  $\langle \lambda \rangle$  of the main tube in run A4 against its effective radius  $r_{\text{eff}}$ . Following (2.16), we define the mean twist as

$$\langle \lambda \rangle = r_{\text{eff}} \left\langle \frac{B_\theta}{r' B_z} \right\rangle, \quad (2.23)$$

where  $r'$  is the distance of a point in the main tube from the tube centre. The match between the simulation results and the linear law is very good up to  $R \simeq 3.6R_0$ , indicating good compatibility with the assumption of homologous expansion. Beyond this size, the flux tube radius is larger than the local pressure scale height and there is a clear deviation between the linear law and the simulation results.

## 2.4 Comparison with a thin flux tube model

One of the main aims of this paper is to evaluate the relevance of the thin flux tube approximation with regards to describing the behavior of flux tubes in 2.5D simulations. In the following, we consider how a rising magnetic flux tube behaves in the context of this approximation (Roberts and Webb 1978, Spruit 1981).



### 2.4.1 Thin flux tube model

The basic assumption of the thin flux tube approximation is that the radius of the flux tube is much smaller than any other characteristic length scale in the system (e.g., local pressure scale height and the radius of curvature of the tube axis). We assume that the quantities are uniform over the tube cross-section, so that their values at the tube axis are representative of their off-axis values. This assumption corresponds to retaining only the zeroth-order term in the axis-centered Taylor-expansion of the quantities in the tube. Higher-order treatments can also be derived (Roberts and Webb 1978, Ferriz-Mas et al. 1989). In the following, we develop a model based on the zeroth-order approximation, which is already sufficient for modelling how the physical properties near the tube centre evolve. To model the evolution of the twist in the main tube, it is necessary to extend to a second-order approach.

Instantaneous pressure balance ( $p_{\text{ex}} = p_{\text{in}} + B^2/2\mu_0$ ) between the tube and its surroundings is assumed. For this assumption to hold, we require that the sound-crossing time over the tube diameter be much smaller than the time required for the tube to transverse a distance comparable to its diameter. This means the adiabatic sound speed  $c_s$  is much larger than the speed of the tube. Taking the terminal velocity (Parker 1975, Moreno-Insertis and Emonet 1996):

$$v_{\text{term}} = \sqrt{\frac{\pi}{C_D} \frac{\Delta\rho}{\rho} gR} \quad (2.24)$$

as the characteristic speed of the tube, and taking  $|\Delta\rho/\rho| \approx 1/\beta$ , we arrive at the criterion:

$$\left(\frac{R_{\text{tube}}}{H_p}\right)^{1/2} \left(\frac{1}{\beta}\right)^{1/2} \ll O(1). \quad (2.25)$$

We make the additional assumption that the horizontal thin flux tube evolves adiabatically, subject to instantaneous pressure balance with its surrounding. This means that the state of the tube at any time is only a function of its initial state and the height it has risen. A convenient measure for the height of the flux tube is the *external pressure contrast*,

$$\chi_p \equiv p_1/p_0, \quad (2.26)$$

where  $p_0$  is the ambient pressure at the initial height of the tube and  $p_1$  is the ambient pressure at a different height. Thus, the physical quantities within the flux tube (e.g.  $\beta$ ,  $\rho_i$  etc.) at any time are functions of their initial values and  $\chi_p$ .

For a uniform horizontal flux tube, conservation of longitudinal magnetic flux leads to

$$\frac{\rho_{i1}}{\rho_{i0}} = \frac{B_1}{B_0}, \quad (2.27)$$

where  $B$  here is the longitudinal field strength of the thin flux tube. Combining this with the condition of instantaneous pressure balance, we have

$$\frac{\rho_{i1}}{\rho_{i0}} = \chi_p^{1/2} \left(\frac{\beta_0 + 1}{\beta_1 + 1}\right)^{1/2}. \quad (2.28)$$

From the adiabatic evolution of the flux tube,

$$\frac{\rho_{i1}}{\rho_{i0}} = \left( \frac{p_{1i}}{p_{0i}} \right)^{1/\gamma}, \quad (2.29)$$

and Eq. (2.28), we obtain

$$\frac{\beta_1 + 1}{\beta_0 + 1} = \left( \frac{\beta_1}{\beta_0} \right)^{2/(2-\gamma)} \chi_p. \quad (2.30)$$

Given an initial value  $\beta_0$ , we can solve for  $\beta_1$ , after the tube has risen through a pressure contrast of  $\chi_p$ . For  $\beta \gg 1$ , we have  $\beta_1/\beta_0 = \chi_p^{(\gamma-2)/\gamma}$ . The physical properties of the flux tube can be expressed as functions of  $\beta_1$  in the following way

$$B(\chi_p) = B_0 \left( \frac{\beta_1}{\beta_0} \right)^{1/(\gamma-2)}, \quad (2.31)$$

$$\rho_i(\chi_p) = \rho_{i0} \left( \frac{\beta_1}{\beta_0} \right)^{1/(\gamma-2)}, \quad (2.32)$$

$$T_i(\chi_p) = T_{i0} \left( \frac{\beta_1}{\beta_0} \right)^{(\gamma-1)/(\gamma-2)}, \quad (2.33)$$

$$R(\chi_p) = R_0 \left( \frac{\beta_1}{\beta_0} \right)^{1/(4-2\gamma)}, \quad (2.34)$$

where  $R$  is the radius of the flux tube and the expressions on the r.h.s. can be expressed in terms of  $\chi_p$  by virtue of Eq. (2.30).

Of the four simulation runs A1 to A4, we chose to compare the thin flux tube model with results from Run A4 because the effect of magnetic diffusion is smallest for this case. Fig. 2.7 shows the dependence of  $|B|$ ,  $T$ ,  $\beta$  and the tube radius as functions of  $\chi_p$ . The values of  $|B|$ ,  $T$  and  $\beta$  in the simulation were taken at the *centre* of the main tube, and are plotted as diamonds. The effective radius  $r_{\text{eff}}$  of the main tube is defined by Eq. (2.18). The solid lines show these quantities as calculated with Eqs. (2.30) to (2.34). Since  $\chi_p$  is the pressure contrast,  $\chi_p < 1$  corresponds to heights above the original position of the tube. For this simulation, we have tracked the main tube until  $\chi_p = 5.4 \times 10^{-3}$ , corresponding to over 5 pressure scale heights. The thin tube predictions agree well with the simulation results over this wide range of heights, even at the lowest values of  $\chi_p$  where the radius becomes comparable to or larger than the local pressure scale height. The thin flux tube predictions of temperature, density and  $|B|$  deviate from their actual values in the main tube centre by less than 2%. The values of  $\beta$  calculated with the thin tube model deviate from the actual values by 3% at most and the effective radius of the main tube differs from the theoretical value by less than 4%.

The comparison we have made here shows that Eqs. (2.30) to (2.34) accurately describes the height dependence of the physical properties *in the tube centre*. In order for our thin tube model to be a dynamical model, we must also solve the equation of motion for a thin flux tube. This will then allow us to model the motion of the main tube as well as the time-dependence of its physical properties in the thin flux tube framework. This comparison is carried out in the following section.

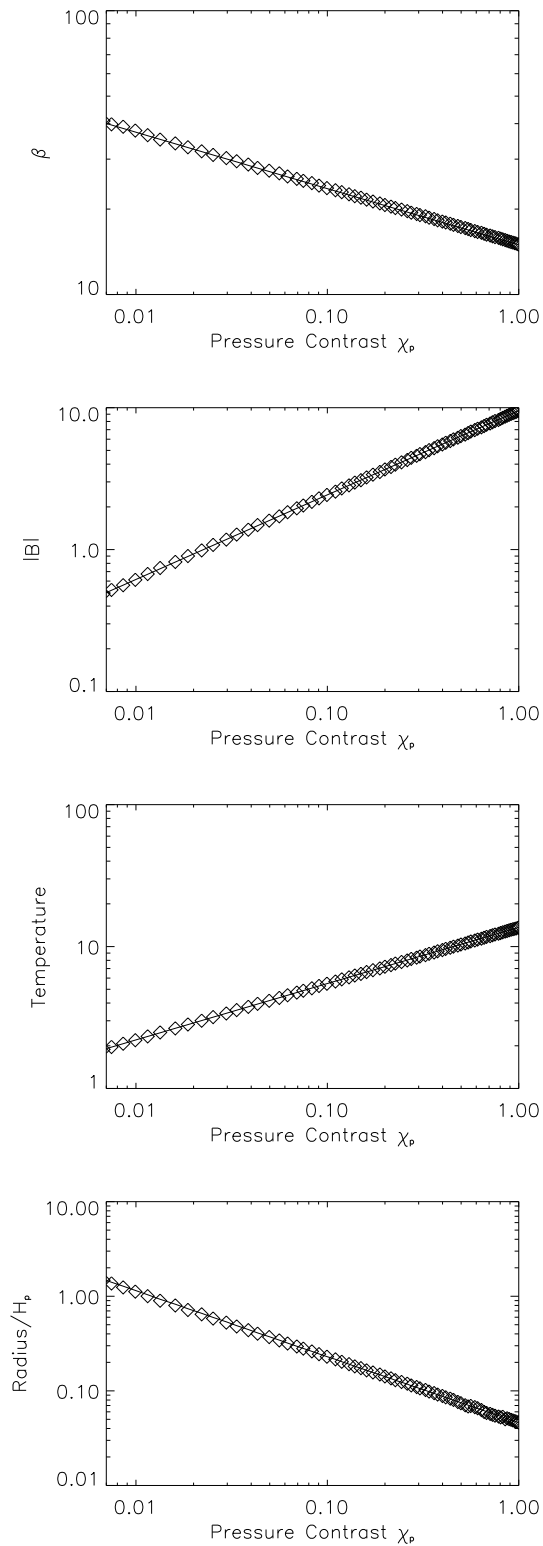


Figure 2.7: Comparison between the simulation (run A4) and the thin flux tube model. Diamonds indicate values of the physical quantities at the tube centre in the simulation and the solid lines show the predictions from the thin tube model (Eqs. (2.30)-(2.34)).

### 2.4.2 Modelling the motion of the main tube

As explained in the introduction, the motion of a twisted magnetic flux tube in an unmagnetized environment shares a number of features with the motion of a rigid cylinder in a flow (Emonet and Moreno-Insertis 1998, Emonet et al. 2001). Under a number of simplifying assumptions, the equation of motion of the magnetic tube can be written in a simple way; among them we count: (1) zero circulation and small Mach number of the surrounding flow; (2) not too low Reynolds numbers ( $Re \gtrsim 50$ ); (3) small length-scales and long timescales of change for the flux tube compared to the intrinsic length and time scales, respectively, of the flow. Under those assumptions, the integrated effect of the fluid stresses on the periphery of the tube can be simply described by a drag force given by the classical aerodynamic formula and an enhancement of the inertia of the tube because of the co-acceleration of the external medium in the vicinity of the tube (Batchelor 1967). For a cylinder or flux tube driven by its own buoyancy in rectilinear motion this would yield:

$$I\dot{v}_y = g\frac{\Delta\rho}{\rho} - \frac{C_D}{\pi} \frac{|v_y|v_y}{R}, \quad (2.35)$$

where  $v_y$  is the vertical velocity of the tube,  $\Delta\rho/\rho$  the relative density difference between the tube and its environment and  $g$  the gravitational acceleration. The second term on the right is the drag acceleration, with  $C_D$  being the aerodynamic drag coefficient (of order unity for  $Re \gg 1$ ) and  $I$  the enhanced inertia factor (which is  $\approx 2$  for  $\beta \gg 1$ ).

Figure 2.8 shows the rise velocity of the main tube (upper panel) and its height (lower panel), both as functions of time. Values from the simulation are indicated as diamonds. The solid lines indicates the theoretical profiles found by integrating Eq. (2.35). The mean density deficit of the main tube,  $\langle\Delta\rho/\rho\rangle = 0.013$ , and its initial radius,  $R = 0.64$ , were used as initial conditions for the path integration. The values of the drag coefficient and enhanced inertia factor used are  $C_D = 2.0$  and  $I = 2.0$  respectively. To take into account the effect of tube expansion on the buoyancy and drag forces, Eqs. (2.32) and (2.34) were used to update the tube radius and density at each time step of the path integration.

The velocity and height profiles from the thin tube approximation are in general agreement with the motion of the main tube between  $t = 0$  and  $t = 200$ . Between  $t = 0$  and  $t = 20$ , the main tube approximately undergoes a freefall acceleration in accordance with its own buoyancy. The motion of the main tube during this time interval is well-matched by the solid lines. The time taken for the main tube to rise a height difference of  $\Delta y = 30$  (corresponding to 4.1 pressure scale heights) is  $\Delta t = 273$ . The corresponding rise time predicted by the thin flux tube mode is  $\Delta t = 256$ , which is within 10% of the actual value.

One feature of the motion of the main tube which is not predicted by the thin tube calculations is the temporary deceleration of the tube between  $t = 20$  and  $t = 30$ . As reported by Moreno-Insertis and Emonet (1996), this is a result of the differential acceleration experienced by the different parts of the flux tube. Since, initially, the core of the tube has the largest density deficit, it undergoes a stronger acceleration than the parts of the tube above it. This differential acceleration leads to a compression at the apex of the tube, which enhances the transverse magnetic field there. The enhanced magnetic tension near the apex of the tube eventually decelerates the core of the flux tube (our main tube) and induces an internal oscillation.

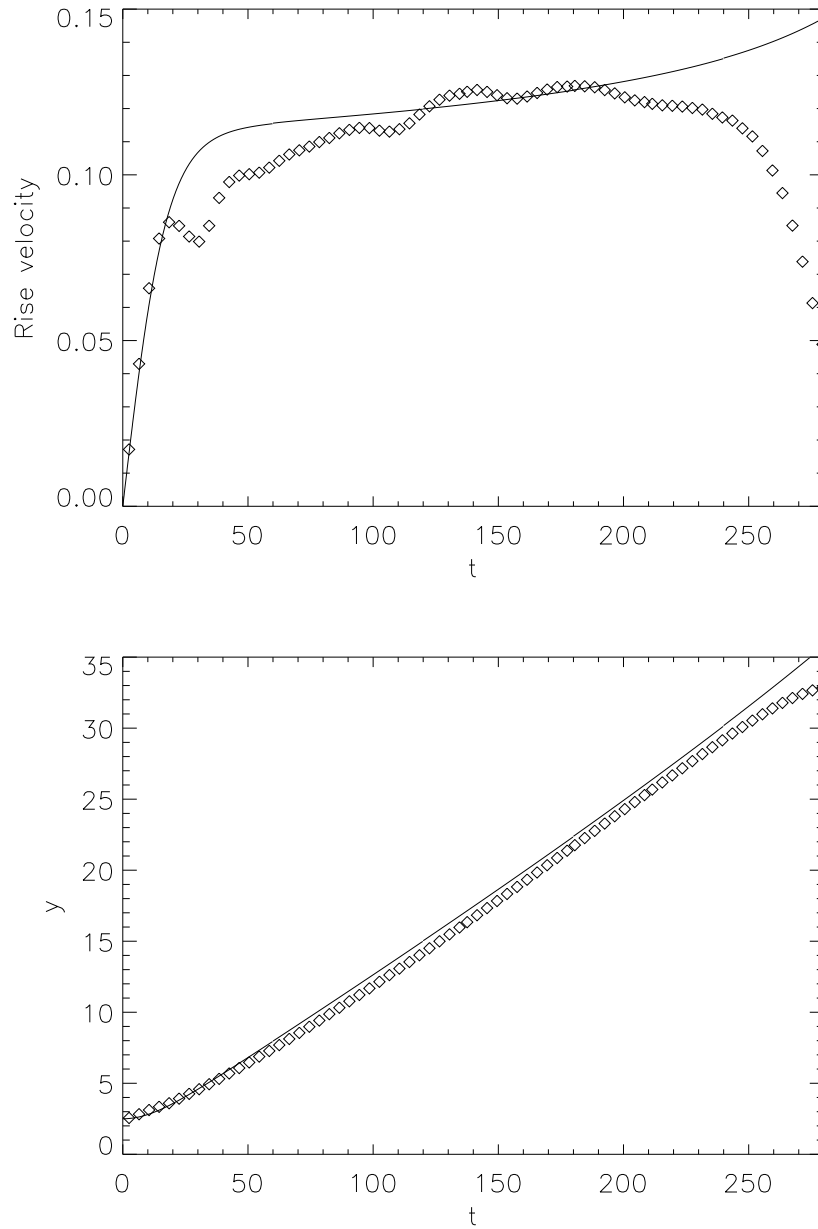


Figure 2.8: Rise velocity (upper panel) of the main tube and its height (lower panel), both as functions of time. Diamonds indicate values from the MHD simulation (run A4). The solid line shows the velocity profile calculated with the thin flux tube model, with  $C_D = 2.0$  and  $I = 2.0$ .

This effect, which is not described by Eq. (2.35) for the motion of a thin flux tube, is a source of discrepancy between the simulation results and the thin flux tube calculations. Another discrepancy is the deceleration of the main tube after  $t = 200$ , which is not predicted by the thin flux tube result. This deceleration is due to the closed top boundary condition used. Eq. (2.35) does not take this into account.

Near the top of the simulation domain, the main tube is so large that it can no longer be considered a thin flux tube. At  $t = 253$ , the main tube has an effective radius equal to  $H_p$ . In Section 2.5, we examine in more detail how the limit of the thin flux tube model is reached as the flux tube increases in size.

### 2.4.3 The asymmetric rise of magnetic flux tubes and their trailing vortex streets

In the simulations discussed thus far, the background atmosphere was initially plane-parallel and the flux tube initially axisymmetric and stationary. This confines the flux tube to a purely vertical trajectory. To study the asymmetric rise of flux tubes, we carried an additional simulation run. Run B has essentially the same initial condition as Run A4 ( $\beta_0 = 15$ ,  $\lambda = 0.25$ ,  $R_0 = 0.5$ ), with the exception that the flux tube is initially rotating solidly about its axis with angular velocity  $\omega = 0.03$ . The vorticity integrated over the initial flux tube ( $r \in [0, 2R_0]$ ) is  $\Omega_0 = \int_0^{2R_0} \nabla \times \vec{v}_t dS = \oint \vec{v} \cdot d\vec{l} = 0.2$ .

As already mentioned in the introduction, a flux tube with a net vorticity  $\vec{\Omega}$  travelling with forward velocity  $\vec{V}$  with respect to the external medium experiences a lift force equal to  $-\rho\vec{\Omega} \times \vec{V}$ . The lift force causes a sideways acceleration of the flux tube so that its motion deviates from the vertical. In simulations runs A1 to A4, we have seen that a flux tube rising purely vertically sheds equal but opposite amounts of vorticity to the left and right halves of its wake. When the tube motion is no longer purely vertical, the two sides of the tube shed unequal amounts of vorticity. Each time a vortex roll is emitted from the flux tube, the remaining tube and wake structure is left with a net vorticity.

Emonet et al. (2001) found that the quasi-periodic shedding of vorticity of alternating sign by a rising flux tube leaves this tube and wake structure with a net circulation that reverses its sign periodically in time. Thus the horizontal component of the lift acceleration also alternates periodically. This results in an oscillatory, horizontal motion of the flux tube super-imposed on the general vertical rise of the tube, so that it traces out a zigzag path. By adding the lift acceleration  $-\vec{\Omega} \times \vec{v}$  to the equation of motion of the thin flux tube and assuming a sinusoidal time-varying vorticity for the tube and wake, they could model the zigzag motion of the tube. We found that  $\Omega_z(t) = 0.04 \sin(2\pi t/80 + 5.2)$  gives a good agreement between the integrated path from the thin flux tube model (plotted as a dashed line in Fig. 2.9) and the actual path of the main tube. The sequence of circles indicate the positions and effective radii of the main tube as it rises and expands.

Figure 2.10 shows the vorticity distribution at  $t = 280$ . The three vortex rolls of alternating sign constitute a pattern reminiscent of a von Kármán vortex street. The first vortex roll shed by the flux tube is centered at  $(x, y) = (-3, 12)$  and has negative sign. This means that, as this roll was being shed, the remaining tube and wake system was gaining a net positive vorticity. The lift force then acts to steer the tube and wake system towards the right. During this time, vortex rolls with positive vorticity are preferentially

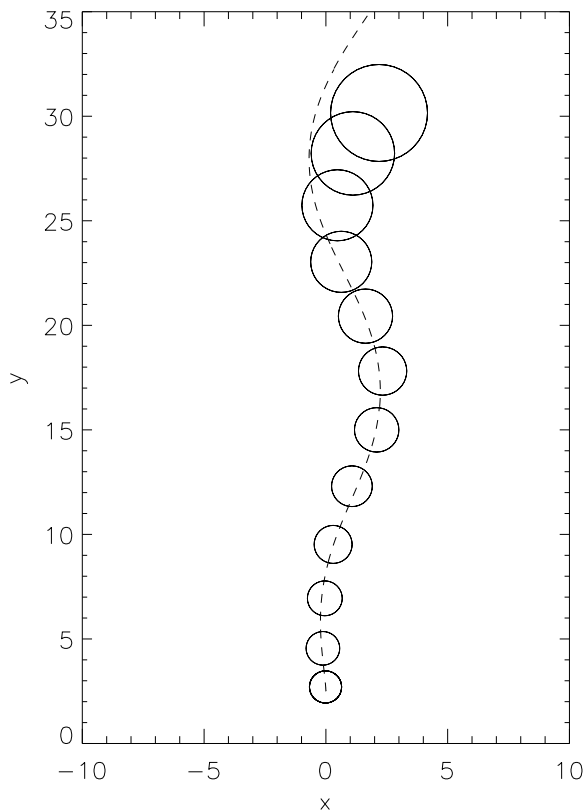


Figure 2.9: The trajectory of the main tube in run B. The circles indicate the position of the main tube at different times during the simulation. The effective radius of the main tube at different instances is given by the size of the circles in the plot. The dashed line shows the trajectory from a thin flux calculation, taking into account the aerodynamic lift force.

shed off the tube. This continues until the tube and wake system has a net negative vorticity. At this point, the lift force pushes the tube back towards the left.

## 2.5 Exploring the limits of the thin flux tube approximation

In this section, we address the question: How relevant are the predictions of the thin flux tube model in describing the quasi-static structure of a rising flux tube as its radius approaches and exceeds the local pressure scale height? To explore the transition from the thin flux tube regime to the ‘thick’ flux tube regime, we performed a simulation (Run C) of a rising tube, starting with a flux tube with an initial flux 100 times larger than in the previous cases. Here, the domain spans  $x \in [-40, 40]$  and  $y \in [0, 70]$ . The flux tube is initially centered at  $(x_0, y_0) = (0, 20)$  with  $B_0 = 12.3$ ,  $R_0 = 5$  (corresponding to  $1/4$  of the local pressure scale height) and  $\lambda = 0.1$ .

Figure 2.11 shows the flux tube at  $t = 0$  and  $t = 220$ . The five concentric green

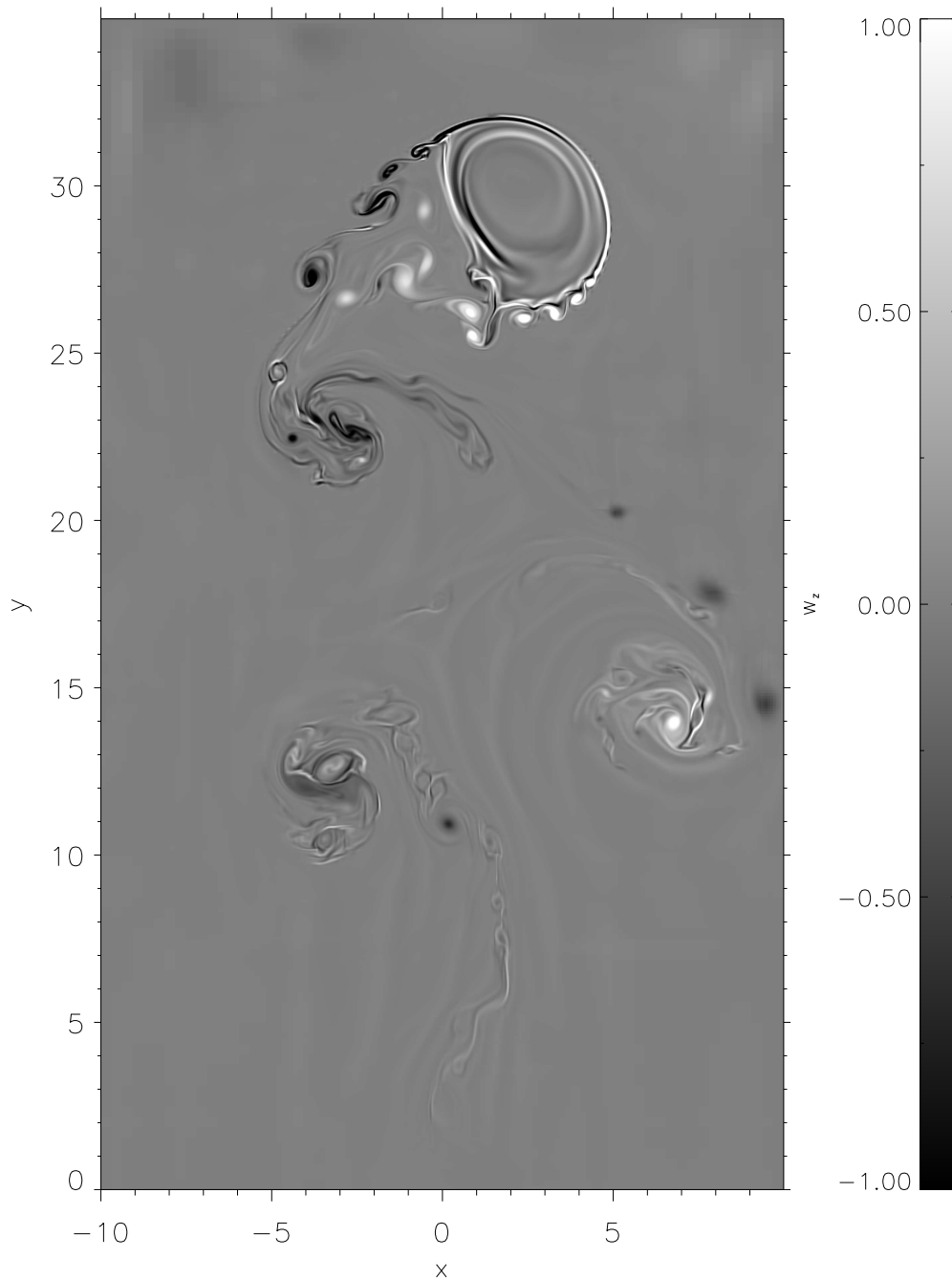


Figure 2.10: The distribution of the vorticity at  $t = 280$  for run B. In this simulation, the flux tube had an initial net vorticity. Aerodynamic lift causes the flux tube to rise in a zigzag fashion, leaving behind a vortex street in its wake.



Flux roll	$R (H_p)$	$\Phi (\Phi_0)$	Symbol in Fig. 2.12
1	0.02	0.01	+
2	0.08	0.1	◇
3	0.1	0.2	△
4	0.2	0.5	□
5	0.3	0.8	×

Table 2.2: The flux and initial radius of the flux rolls as shown in Fig. 2.11(a).

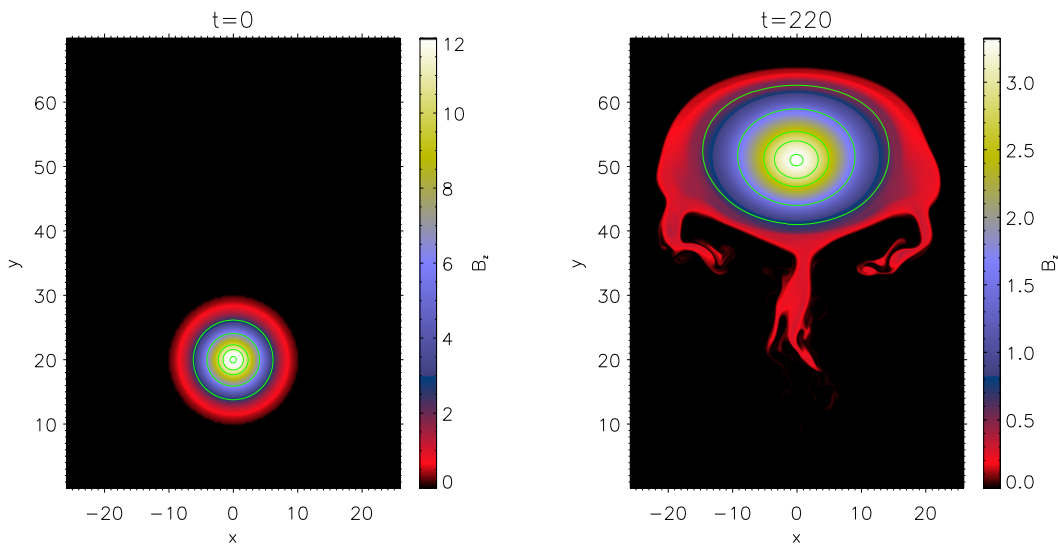


Figure 2.11: Evolution of a large flux tube (Run C). Shown in color is the longitudinal field. Each of the five circular green contours represent a magnetic field line projected onto the plane. Every contour encloses a certain amount of flux, which defines a *flux roll*. Table 2.2 gives the flux and initial radius of each flux roll.

contours in the left panel are the planar projection of different field lines. Each of these contours defines a *flux roll*. By tracking these contours, we follow the evolution of these flux rolls. The longitudinal flux and initial radius of each of these rolls is given in Table 2.2.

In order to evaluate the validity of the thin flux tube approximation, we compare its predictions with the simulation results for all five flux rolls. For the thin flux tube predictions, Eqs. (2.31)-(2.34) are used to calculate how the physical quantities evolve. The initial values ( $B_0$ ,  $\rho_0$ , etc.) are taken as averages inside the rolls. The values from the thin flux tube calculations are then compared with the average values measured in the flux rolls at later times in the simulation.

Figure 2.12 shows the relative discrepancies between the model predictions and the average values from the simulation as a function of effective radius of largest flux roll (flux roll 5). The size of this flux roll is representative of the ‘true’ size of the rising flux tube. As expected, the discrepancy grows as the effective radius of the flux tube becomes comparable to the local pressure scale height. In this regime, the flux tube interior is sufficiently stratified that average values of its physical properties do not match with the corresponding thin flux tube values, so the thin flux tube approximation is no longer

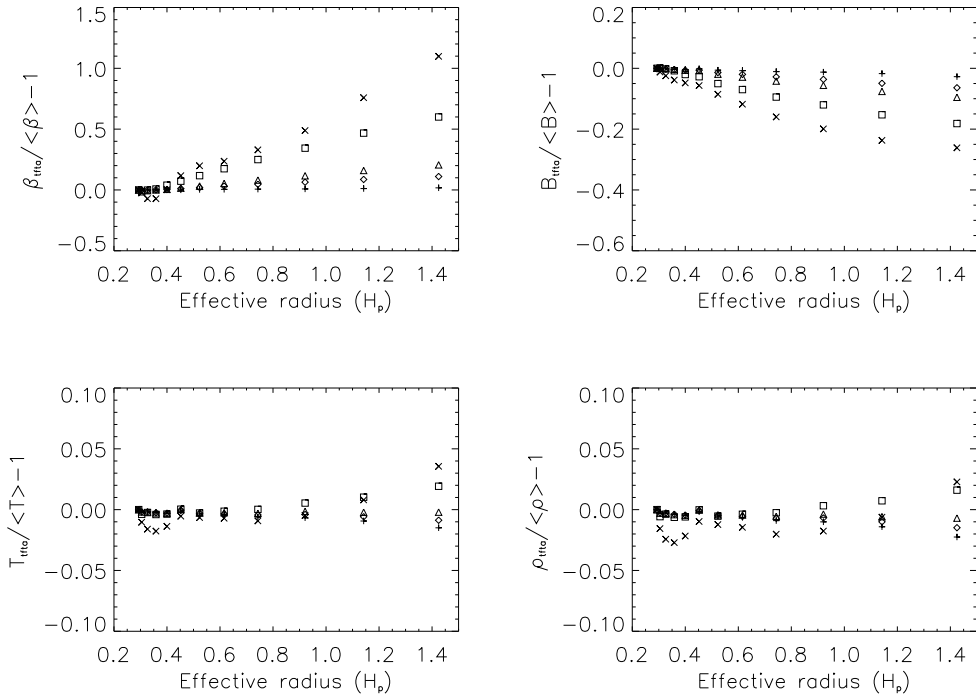


Figure 2.12: Comparison between thin flux tube calculations with average quantities inside the flux rolls (Run C). The different symbols correspond to quantities in the different flux rolls (see Table 2.2). As the effective radius of the flux tube approaches the local pressure scale height  $H_p$ , the discrepancy between the simulation results and the thin flux tube predictions grows.

appropriate for describing the state of the flux tube. The discrepancies in temperature and density do not grow as much as the discrepancies in field strength and  $\beta$  for the following reason: for an ideal thin flux tube in pressure balance with its surroundings, the relative difference of  $T$  and  $\rho$  between the tube and its surroundings is always of order  $O(\beta^{-1})$ . Thus relative differences in  $T$  and  $\rho$  decrease with increasing  $\beta$  (the case of an expanding tube). Consequently, discrepancies in  $T$  and  $\rho$  between the thin tube predictions and the simulation results do not tell whether the thin flux tube approximation is good at describing the average properties of the flux tube. In contrast, discrepancies in  $\beta$  and  $|B|$  show clearly the transition between the thin flux tube regime to the ‘fat’ flux tube regime, when the radius of the tube is comparable to the pressure scale height.

We have also examined how the average twist,  $\langle \lambda \rangle$ , of each flux roll evolves as they expand. Fig. 2.13 shows  $\langle \lambda \rangle$  as a function of the effective radii of the flux rolls. Again, there is good agreement between the data points and the solid curve, which plots the relation given by Eq. (2.22).

## 2.6 Conclusions

We have carried out idealized 2.5D MHD simulations of buoyant magnetic flux tubes rising in a stratified layer over a range of Reynolds numbers ( $25 \gtrsim Re \gtrsim 2600$ ). Our

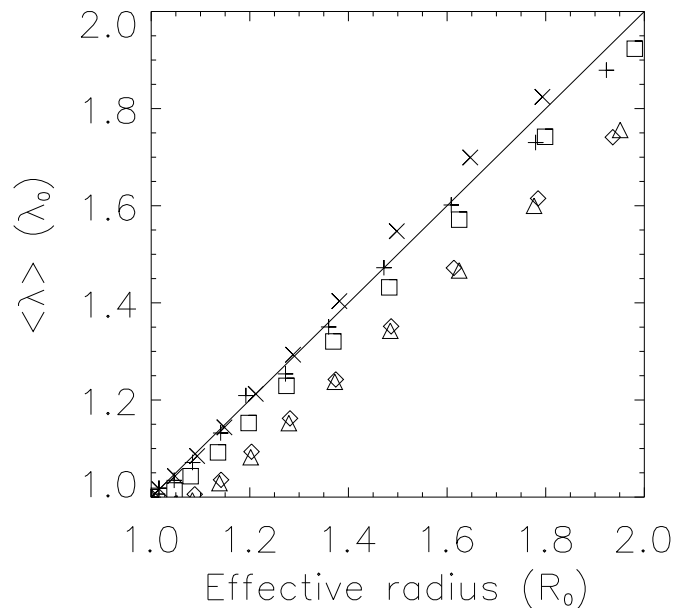


Figure 2.13: Variation of the average twist of the flux rolls as a function of their effective radii. The different symbols show the average twist of the five flux rolls (Run C). The solid line shows the relation given by Eq. (2.22). The good match between the simulation results and relation (2.22) indicates that the flux rolls expand homologously.

simulations confirm previous results in the literature. Additionally, we have analyzed the dependence of the results on the Reynolds number. We found that the detailed structure of the wake, as well as the amount of flux retained in the main tube, varies with the Reynolds number. At sufficiently high Reynolds number ( $Re \gtrsim 600$ ), the vortex pair in the wake break into secondary rolls. The amount of flux retained in the tube also increases with  $Re$ .

We have studied how the twist in a flux tube varies as it expands. In particular, the dimensionless twist  $\langle \lambda \rangle$ , averaged over the main tube, scales approximately linearly with the tube radius. If flux tubes originating from the bottom of the solar convection zone have any amount of initial twist, this twist will be amplified upon the rise of the tube. The twist will be maximum at the apex of the rising loop, where the cross-sectional radius is largest.

We derived thin flux tube equations (Eqs. (2.31)-(2.34)) to model the evolution of the properties a horizontal flux tube rising adiabatically through the atmosphere. Using these equations to model the expansion of the tube, and using Eq. (2.35), the motion of the main tube can be reproduced. For a tube that undergoes asymmetric vortex shedding, the lift force can be included into the equation of motion to explain the zigzag motion of the tube. The vortex shedding associated with this zigzag motion leaves behind a vorticity distribution resembling a von Kármán vortex street.

Furthermore, we studied the transition from the regime of thin flux tubes to the regime of fat flux tubes (Run C). We found that the discrepancy between the thin tube calculations

and the average quantities of flux rolls increases as the flux tube expands. When its radius is comparable to one pressure scale height, the discrepancy between the thin tube calculations and the simulation results can be at least of order  $O(1)$ , meaning the thin flux tube approximation is no longer valid. This result is in accordance with previous expectations. In the solar convection zone, rising toroidal flux tubes approach this limit at a depth of about 10 Mm, so it is no longer appropriate to continue thin flux tube simulations above those depths. On the other hand, our results point in the direction that below such depths, the thin flux tube approximation is useful for studying the evolution of flux tubes.

### 3 Simulation of near-surface convection and the photosphere

In order to simulate photospheric flux emergence, the first requirement is to have an accurate 3-dimensional model of the upper convection zone and the photosphere. In the quiet Sun, the most prominent photospheric feature is the surface granulation. The granulation pattern consists of granules with a typical size of 1 Mm. The boundary of the granules is the intergranular network. In white light, the granules appear brighter than the intergranular network. The granulation pattern is dynamic. Time-sequences of the granulation in the quiet Sun reveal that the typical lifetime of surface features is about 5 minutes (Leighton et al. 1962, Title et al. 1989).

Numerical simulations have firmly established the solar granulation as a radiative-convective phenomenon (Stein and Nordlund 1989, 1998). The individual granules are plumes of hot, upflowing material originating from the convection zone and overshooting into the stably stratified photosphere. The superadiabatic temperature gradient required to drive the motion in the convection zone is maintained by radiative cooling at the thermal boundary layer between the convection zone and the photosphere. Radiative losses make the overshooting material relatively cold and dense. Their overturning motion feeds the intergranular network of downflows.

On the one hand, the near-surface flow responsible for the granulation pattern can influence the evolution of emerging magnetic fields. On the other hand, the Lorentz force of magnetic fields embedded in the fluid may also influence the motion of the fluid. The interplay between magnetic fields and convective plasma, *magneto-convection*, is a key aspect of solar surface magnetism. The ability to model magneto-convection in the near-surface layers and photosphere is therefore important for flux emergence simulations. A proper treatment of this problem requires the inclusion of several physical effects:

**3D compressible MHD** - The convection zone and solar atmosphere are both stratified. Upflowing plasma expands whereas downflowing plasma compresses. The expansion/compression of fluid elements lead to the weakening/intensification of the embedded magnetic field. Additionally, the flows in these layers have Mach numbers up to  $M \sim O(0.1 - 1)$ . As such, the Boussinesq and anelastic approximations are insufficient and the fully-compressible MHD equations must be solved.

**Energy exchange via optically thin radiative transfer** - The energy produced in the core of the Sun must be carried outwards. In the radiative core, the radial energy flux  $F_\nu$  is carried by photons. Owing to the high densities and opacities in this region, the mean free path of a photon is much smaller than the local pressure scale height (i.e. the medium is optically thick over the typical scale of temperature and pressure variations). Thus,

the radiative transport of energy in the radiative core can be treated with the diffusion approximation, with  $\mathbf{F}_{\text{rad}} = -k_{\text{rad}}\nabla T$ , where  $k_{\text{rad}}$  is the coefficient of conduction for radiative transport (Kippenhahn and Weigert 1994). In the convection zone, convection takes over as the dominant mechanism for the transport of energy. Finally, in the transition layer between the convection zone and the photosphere, radiative transfer once again takes over as the dominant mechanism of energy transport.

The plasma at and above this transition layer, however, is tenuous and the photon mean free path is comparable, or larger, than the local pressure scale height ( $H_p \sim 150$  km). This means the medium is optically thin over such a length scale. In this region, the radiative heating rate  $Q_{\text{rad}}$  is an important source term in the energy equation and errors in  $Q_{\text{rad}}$  arising from the unjustified use of the diffusion approximation cannot be ignored. An improved approach is to use the Eddington approximation. Robinson et al. (2003), for example, carried out 3D solar surface convection simulations using the diffusion approximation for optically thick layers and the Eddington approximation for optically thin layers. A shortcoming of the Eddington approximation is that it assumes a nearly isotropic radiation field, which is not the case in the photosphere. In the presence of strong magnetic fields the horizontal gradients exasperates the problem of anisotropy. To determine  $Q_{\text{rad}}$  accurately, it is necessary to calculate the radiation field by solving the Radiative Transfer Equation (thereafter RTE).

**Partial ionization effects** - In the upper convection zone and the photosphere, the plasma is partially ionized, which means its thermodynamic properties are different from a completely neutral or completely ionized ideal gas. The specific internal energy of such a partially ionized gas has two components. The first component is attributed to the thermal energy of the particles. There is also a *latent heat* component, which is associated with the ionization and excitation energies of the species in the gas. Changes in the ionization state of the gas affect the gas pressure for a given mass density, the specific heats  $c_v$  and  $c_p$  as well as the opacity of the gas (Rast and Toomre 1993a,b, Rast et al. 1993). As shown by Rast and co-workers, all these effects are important for the local dynamics in the convective zone as well as the global transport properties of energy and enthalpy. In the upper few Mm of the convection zone, about 2/3 of the vertical enthalpy flux is carried in the form of latent heat. This is indicative of how important partial ionization effects are for solar convection.

All these effects are treated by the MURaM code (Vögler et al. 2005) under the assumption of local thermodynamic equilibrium (LTE). In the following paragraphs, we review why each the aforementioned effect is important. In § 3.1, we present the full set of radiative MHD equations solved by MURaM and discuss the numerical schemes used. In § 3.2, we give details of the setup we used to obtain a numerical model of the upper convection zone and photosphere. Furthermore, we discuss the properties of the convection. In § 3.4, we present an explanation for the reversed granulation, which is a reversal of the temperature fluctuation pattern at about 100 km above the visible surface. The understanding gained from this exercise will eventually help us to better interpret the results from the flux emergence simulations, which will be presented in the next two chapters.

## 3.1 The radiative MHD equations

The MURaM code was developed for simulation of photospheric radiative-MHD phenomena. The MHD equations solved by MURaM consist of the induction equation, the equation of continuity, the equation of motion and the energy equation. These equations are supplemented by the equation of state (EOS) and the radiative transfer equation (RTE).

### 3.1.1 The equations of magnetohydrodynamics

#### Induction equation

$$\frac{\partial \mathbf{B}}{\partial t} = \nabla \times (\mathbf{v} \times \mathbf{B}) - \nabla \times (\eta \nabla \times \mathbf{B}). \quad (3.1)$$

This equation describes the evolution of a magnetic field embedded in an electrically conducting fluid. Here,  $\eta = c^2/4\pi\sigma$  is the magnetic diffusivity,  $c$  the speed of light and  $\sigma$  the electrical conductivity.

#### Continuity equation

$$\frac{\partial \rho}{\partial t} + \nabla \cdot (\rho \mathbf{v}) = 0. \quad (3.2)$$

This equation expresses the principle of mass conservation.

#### Equation of motion

$$\frac{\partial \rho \mathbf{v}}{\partial t} + \nabla \cdot \left[ \rho \mathbf{v} \otimes \mathbf{v} + \left( p + \frac{B^2}{8\pi} \right) \underline{\underline{1}} - \frac{\mathbf{B} \otimes \mathbf{B}}{4\pi} \right] = \rho \mathbf{g} + \nabla \cdot \underline{\underline{\tau}}. \quad (3.3)$$

This equation is a statement of the principle of momentum conservation. Here,  $p$  is the gas pressure and  $\mathbf{g}$  is the gravitational acceleration. In a thin layer near the solar surface, we can take this to be constant, with  $\mathbf{g} = (0, 0, -2.74 \times 10^4) \text{ cm s}^{-2}$ . The terms  $\mathbf{v} \otimes \mathbf{v}$  and  $\mathbf{B} \otimes \mathbf{B}$  represent dyadic products and  $\underline{\underline{1}}$  represents the  $3 \times 3$  identity matrix. The Lorentz force  $\mathbf{j} \times \mathbf{B}/c$  has been split into two terms. The first term is a gradient of the magnetic pressure, which is defined as:

$$p_{\text{mag}} = \frac{B^2}{8\pi}.$$

The second term in the Lorentz force is the term  $\nabla(\mathbf{B} \otimes \mathbf{B}/4\pi)$ , which describes the magnetic tension of field lines. The last term on the r.h.s. of Eq. (3.3) is the viscous force. The components of the viscous stress tensor  $\underline{\underline{\tau}}$  for a compressible fluid are given by:

$$\tau_{ij} = \mu \left( \frac{\partial v_i}{\partial x_j} + \frac{\partial v_j}{\partial x_i} - \frac{2}{3} \delta_{ij} (\nabla \cdot \mathbf{v}) \right), \quad (3.4)$$

where  $\mu$  is the dynamic viscosity and  $\delta_{ij}$  the Kronecker-Delta symbol. The dynamic viscosity is related to the kinematic viscosity  $\nu$  by the relation  $\mu = \rho\nu$ .

### Energy equation

The sum of the internal, kinetic and magnetic energy densities per unit volume is  $e = \rho\epsilon + \frac{1}{2}\rho v^2 + B^2/8\pi$ . Its evolution is described by the energy equation

$$\begin{aligned} \frac{\partial e}{\partial t} + \nabla \cdot \left[ \mathbf{v} \left( e + p + \frac{B^2}{8\pi} \right) - \frac{1}{4\pi} \mathbf{B} (\mathbf{v} \cdot \mathbf{B}) \right] \\ = \frac{1}{4\pi} \nabla \cdot (\mathbf{B} \times \eta \nabla \times \mathbf{B}) + \nabla \cdot (\mathbf{v} \cdot \underline{\underline{\tau}}) + \nabla \cdot (K \nabla T) \\ + \rho (\mathbf{g} \cdot \mathbf{v}) + Q_{\text{rad}}. \end{aligned} \quad (3.5)$$

Here  $T$  is the temperature and  $K$  the thermal conductivity. The first and second terms on the r.h.s. of Eq. (3.5) are the Ohmic and viscous dissipation terms respectively.  $Q_{\text{rad}} = -\nabla \cdot \mathbf{F}_{\text{rad}}$  is the radiative heating rate. As mentioned earlier, the radiative transfer equation (RTE) must be solved in order to evaluate this term.

### 3.1.2 Equation of state

The equation of state (EOS) used in the MURaM code is implemented in the form of look-up tables  $T = T(\epsilon, \rho)$  and  $p = p(\epsilon, \rho)$ . The look-up tables were evaluated by solving the Saha-Boltzmann equations. The first ionization of the 11 most abundant elements were considered. For a detailed account of how the tables were evaluated, we refer the reader to Appendix A of Vögler et al. (2005).

### 3.1.3 Numerical treatment of the MHD equations

MURaM consists of two modules, one for solving the MHD equations and one for solving the radiative transfer. The two modules are coupled in the following way: At each time step, the MHD module provides the spatial distribution of temperature, density and pressure. This is used by the radiative transfer module to solve the RTE. The radiative transfer module provides  $Q_{\text{rad}}$  to the MHD module, which allows the latter to update the solution. In this section, we describe how the MHD module solves the MHD equations numerically. In Section 3.1.5, we describe how the radiative transfer module is implemented. For more details about both modules, see Vögler (2003) and Vögler et al. (2005).

MURaM uses the following numerical scheme to solve the MHD equations (3.1)-(3.5). The equations are solved on a 3-dimensional cartesian grid, with regular grid-spacing in each cartesian direction. The spatial discretization of the equations is based on a fourth-order centered-difference scheme on a five-point stencil. The code is parallelized by means of domain decomposition. The Message Passing Interface (MPI) is used for communication between the sub-domains.

It has been estimated that in the surface layers of the Sun, the hydrodynamics Reynolds number of the flow lies in the range  $10^8 - 10^9$  (Komm et al. 1991). These values for the Reynolds numbers correspond to viscous length scales on the order of centimeters, which means that, at the length and velocity scales of the granulation, viscous effects are negligible. At present, it is computationally infeasible to carry out simulations of surface granulation with sufficiently small grid-spacing to resolve such tiny length scales. As



such, all attempts at simulating the surface granulation are effectively *large-eddy* simulations. These simulations resolve flow structures with length scales larger than grid-spacing available. Owing to non-linearities in the MHD equations, energy may cascade down to sub-grid scales, which could lead to numerical instabilities in the calculations. Some numerical schemes have inherent numerical diffusivities that prevent this from happening. For higher-order finite difference schemes, the inherent numerical diffusivities are small. In order to keep the simulations stable, explicit diffusive terms are required. For this purpose, MURaM makes use of artificial diffusivities. A combination of *hyper*- and *shock-resolving* diffusivities are used. Hyperdiffusivities are implemented in such a way, that the diffusion terms associated with them are comparable in magnitude to the inertial terms only at length scales close to the grid-spacing. For the thermal and viscous coefficients  $K$  and  $\nu$ , the hyperdiffusivities are defined throughout the entire domain using the scheme described in Vögler et al. (2005). For the magnetic diffusion term in the Induction Equation, we impose a constant magnetic diffusivity  $\eta_0$  throughout the domain. Near the top and bottom boundary boundaries and in regions of strong expansion of the magnetic fields, we found it necessary to use an additional artificial magnetic diffusivity to stabilize the simulation. Shock diffusivities are implemented in the same way as Vögler et al. (2005). In regions of converging flow (i.e.  $\nabla \cdot \mathbf{v} < 0$ ), the values of the shock diffusivities are proportional to  $|\nabla \cdot \mathbf{v}|$ . In other regions of the domain, the values of the shock diffusivities are set to zero.

MURaM uses an explicit fourth-order Runge-Kutta scheme for the temporal discretization. The maximum size of the time step,  $\Delta t_{\max}$ , is determined by a modified CFL-criterion (Hirsch 1990a,b):

$$\Delta t_{\max} = \min(\Delta t_{\text{ad}}, \Delta t_{\text{diff}}), \quad (3.6)$$

where  $\Delta t_{\text{ad}}$  is the advective time step given by

$$\Delta t_{\text{ad}} = \frac{8 \min(\nu, \eta, \kappa)}{3 c_{\text{tot}}^2}, \quad (3.7)$$

and  $\Delta t_{\text{diff}}$  is the diffusive time step given by

$$\Delta t_{\text{diff}} = \frac{2}{3} \left[ \max(\nu, \eta, \kappa) \left( \frac{1}{\Delta x^2} + \frac{1}{\Delta y^2} + \frac{1}{\Delta z^2} \right) \right]^{-1}. \quad (3.8)$$

The total wave speed  $c_{\text{tot}}$  is defined as

$$c_{\text{tot}} = v + c_{\text{sound}} + c_{\text{Alfvén}}, \quad (3.9)$$

where  $v$  is the fluid speed,  $c_{\text{sound}} = \sqrt{p/\rho}$  the isothermal sound speed and  $c_{\text{Alfvén}} = B/\sqrt{4\pi\rho}$  the Alfvén speed.

### 3.1.4 Radiative Transfer Equation

Let  $d\varepsilon_{\text{rad}}$  be the quantity of energy carried by radiation in the frequency interval  $(\nu, \nu + d\nu)$  along the direction  $\boldsymbol{\mu}$  within a solid angle  $d\Omega$  passing through an area element  $dS$  with unit normal  $\hat{\mathbf{n}}$  in a time interval  $dt$ . The monochromatic specific intensity  $I_\nu$  is then defined as

$$d\varepsilon_{\text{rad}} = I_\nu(\mathbf{x}, \boldsymbol{\mu}, t) \boldsymbol{\mu} \cdot \hat{\mathbf{n}} dS d\Omega d\nu dt. \quad (3.10)$$

The Radiative Transfer Equation (RTE) governs the change in  $I_\nu$ :

$$\left(\frac{1}{c} \frac{\partial}{\partial t} + \boldsymbol{\mu} \cdot \nabla\right) I_\nu = \kappa_\nu \rho (S_\nu - I_\nu), \quad (3.11)$$

where  $\kappa_\nu$  is the monochromatic opacity and  $S_\nu$  the source function. Since the speed of the fluid motion is much less than the speed of light  $c$ , the explicit time dependence can be dropped and we have the time-independent RTE:

$$\boldsymbol{\mu} \cdot \nabla I_\nu = \kappa_\nu \rho (S_\nu - I_\nu). \quad (3.12)$$

A natural measure for the distance transversed by photons in absorbing media is the optical depth

$$d\tau_\nu := \kappa_\nu \rho ds. \quad (3.13)$$

where  $ds$  is the path element along a given direction  $\boldsymbol{\mu}$ . This allows one to write the transfer equation as

$$\frac{dI_\nu}{d\tau_\nu} = S_\nu - I_\nu. \quad (3.14)$$

This equation has the formal solution

$$I_\nu(\tau_\nu) = I_\nu(0)e^{-\tau_\nu} + \int_0^{\tau_\nu} S_\nu(t_\nu) e^{-(\tau_\nu - t_\nu)} dt_\nu. \quad (3.15)$$

The radiative energy flux  $\mathbf{F}_\nu$  is the first moment of the specific intensity:

$$\mathbf{F}_\nu = \oint_{4\pi} I_\nu(\boldsymbol{\mu}) \boldsymbol{\mu} d\Omega. \quad (3.16)$$

The mean intensity is

$$J_\nu = \frac{1}{4\pi} \oint_{4\pi} I_\nu(\boldsymbol{\mu}) d\Omega. \quad (3.17)$$

The radiative heating/cooling term in Eq. (3.5) is defined as

$$Q_{\text{rad}} = - \int (\nabla \cdot \mathbf{F}_\nu) d\nu. \quad (3.18)$$

It is this term in the energy equation that couples the magnetohydrodynamics to the radiative transfer. Making use of Eq. (3.12), an equivalent expression for  $Q_{\text{rad}}$  is

$$Q_{\text{rad}} = \int 4\pi \kappa_\nu \rho (J_\nu - \bar{S}_\nu) d\nu \quad (3.19)$$

where  $\bar{S}_\nu = (4\pi)^{-1} \oint_{4\pi} S_\nu d\Omega$  is the angular mean of the source function. As yet, we have not made any assumptions about the form of  $S_\nu$ . Under photospheric conditions, we can assume that the gas is approximately in local thermodynamic equilibrium (LTE). Under this assumption, each fluid element has a well-defined local temperature and the ionic, atomic and molecular population levels satisfy Saha-Boltzmann statistics. This assumption greatly simplifies the computational effort to solve the RTE, for the source function can be approximated by the Planck function, i.e.

$$S_\nu = B_\nu(T) = \frac{2h\nu^3}{c^2} \frac{1}{e^{h\nu/kT} - 1}. \quad (3.20)$$

Since the Planck function is isotropic,  $\bar{S}_\nu = B_\nu$ .

### 3.1.5 Numerical treatment of the RTE

In the following, we describe how the radiative transfer module of MURaM solves the RTE numerically (for details, see Vögler et al. 2005). The RTE is solved over a 3D cartesian grid, with the grid centers of this radiative grid defined by the cell corners of the grid used by the MHD module of the code. For each point on this radiative grid, the RTE is solved over 24 ray directions (3 per octant). The method of short characteristics is used to solve the RTE. For each ray direction on a given grid-point, the transfer equation is solved along the ray segment (short characteristic) between the grid-point and the nearest upwind intersection of the ray with a cell boundary. The values of  $T$ ,  $p$  and  $\rho$  at the ends of the ray segment are interpolated from the values in the adjacent grid-points on the MHD grid. Once the transfer equation has been solved for all 24 directions, the quadrature sum of  $I_\nu$  over these rays provides the radiative flux density  $F_\nu$  and the mean intensity  $J_\nu$ .

MURaM can treat the radiative transfer in the grey or non-grey approximation. In the grey approximation, the frequency dependent opacity  $\kappa_\nu$  is replaced by a suitably defined mean opacity  $\bar{\kappa}$ , which is just a function of  $T$  and  $p$ . This function is stored as a look-up table, which the code uses at runtime to determine the opacities in the domain. In the optically thick and thin regimes,  $\bar{\kappa}$  corresponds to the Rosseland and Planck mean opacities, respectively. In the non-grey approximation, opacities at different frequencies are sorted into a number of bins in the following way. Given a 1D reference atmosphere, the depth at which  $\tau_\nu$  becomes unity is determined for each frequency. Depending on the depth at which this occurs, the opacities were sorted into the respective bins. For each bin, a mean opacity look-up table was computed using the same scheme as for the grey case. The use of 4 bins is a good compromise between accuracy and performance. When MURaM is configured to run a non-grey simulation, the radiative transfer module solves the transfer equation 4 times (once for each bin) for each ray segment of a given grid-point. The radiative heating is then the sum of  $Q_{\text{rad}}$  over all 4 bins.

The treatment of frequency dependence by the opacity binning method greatly reduces the computational effort required to solve the radiative transfer. Vögler (2004) has carried out MURaM simulations of photospheric magneto-convection with grey and non-grey radiative transfer and found that the properties and dynamics at  $\tau_{\text{Ross}} = 1$  for both runs are very similar. In the upper photosphere, the non-grey run yields smaller temperature fluctuations than in the grey run. This effect is more pronounced in magnetic concentrations. The r.m.s. contrast of surface brightness maps is slightly lower in the non-grey runs than in the grey runs. This actually leads to an enhancement of the contrast between bright magnetic features and their surroundings.

Since the grey runs require less computational resources, and we are interested primarily in the dynamics near the surface, we have used grey radiative transfer for most of our simulations of flux emergence. We have also repeated one simulation run using non-grey radiative transfer to check that this does not change the results and conclusions we make, which is indeed the case. Synthesis of spectro-polarimetric diagnostics from the simulations, however, requires non-grey radiative transfer because the formation of many spectral lines is very dependent on temperature.

## 3.2 Simulation setup

Here we give details of the simulation setup used to obtain a thermally relaxed 3D model of the upper convection zone and the photosphere. In this simulation there are no magnetic fields present in the domain. The horizontal size of the simulation domain is  $24 \text{ Mm} \times 12 \text{ Mm}$ , with each direction spanned by 480 and 240 grid cells respectively. The height of the domain is  $2.304 \text{ Mm}$ , and is spanned by 144 grid cells. The grid-spacing in the horizontal and vertical directions is 50 and 16 km respectively. Periodic boundary conditions are implemented for the vertical side boundaries. The bottom boundary is open and allows mass to flow in and out of the domain smoothly. The specific entropy  $s$  of both in- and out-flows are constant over the bottom boundary, i.e.

$$\left(\frac{\partial s}{\partial z}\right)_{\text{bottom}} = 0. \quad (3.21)$$

The velocities of the downflows ( $v_z < 0$ ) and upflows ( $v_z > 0$ ) at the bottom boundary are treated differently. The following stress-free boundary conditions are satisfied for downflows at the bottom boundary:

$$\left(\frac{\partial v_x}{\partial z}\right)_{\text{bottom}} = \left(\frac{\partial v_y}{\partial z}\right)_{\text{bottom}} = \left(\frac{\partial v_z}{\partial z}\right)_{\text{bottom}} = 0. \quad (3.22)$$

Upflows at the bottom boundary are vertical:

$$(v_x)_{\text{bottom}} = (v_y)_{\text{bottom}} = \left(\frac{\partial v_z}{\partial z}\right)_{\text{bottom}} = 0. \quad (3.23)$$

For this purely hydrodynamic run, we imposed a closed top boundary, with the velocities satisfying

$$\left(\frac{\partial v_x}{\partial z}\right)_{\text{top}} = \left(\frac{\partial v_y}{\partial z}\right)_{\text{top}} = (v_z)_{\text{top}} = 0. \quad (3.24)$$

We found that, for simulations of magnetic flux emergence, a closed top boundary is inappropriate because it artificially traps the emerged magnetic field inside the domain. For the flux emergence simulations, we have modified the top boundary so that it allows for a smooth outflow or inflow of material. The details of the implementation of this open top boundary condition is given in the next chapter. Details of the boundary condition for the magnetic field at both the top and bottom boundaries will also be discussed in that chapter.

For the initial condition, we took the 1D height profiles of  $\rho$  and  $\epsilon$  from the mixing length model of Spruit (1974) and imposed a plane-parallel atmosphere into the simulation domain. To break the symmetry, we imposed pressure perturbations on the order of a few percent. We then ran the simulation until we obtained a statistically stationary state for the convection. The properties of this 3D model are discussed in the next section.

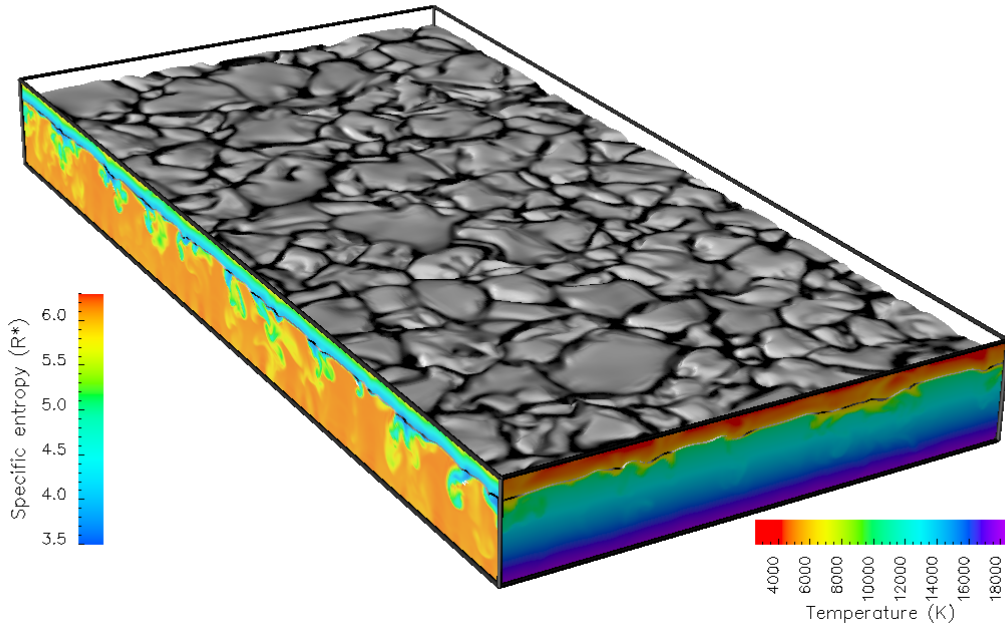


Figure 3.1: A snapshot of the 3D model of the upper convection zone and the photosphere. The gray surface shows the  $\tau_{\text{Ross}} = 1$  level. The grey scale on this surface shows the vertical velocity of the material at that level (dark is downflowing and light is upflowing). The vertical slice on the right side of the domain shows the temperature stratification. The vertical slice on the left side shows the specific entropy distribution.

### 3.3 Properties of near-surface convection and the photosphere

Figure 3.1 shows a snapshot of our numerical model of the upper convection zone and the photosphere. The grey surface shows the Rosseland  $\tau_{\text{Ross}} = 1$  level, calculated along rays directed vertically downwards. From hereon, when we speak of the *visible surface*, we are referring to this level. The pattern of the surface granulation can be clearly discerned from the grey-shading on this surface, which shows the vertical velocity of the material at that level. The grey-shading ranges between  $-3$  (black, downwards) to  $+3$  (white, upwards)  $\text{km s}^{-1}$ . The  $\tau_{\text{Ross}} = 1$  surface is corrugated. The surface is depressed in the intergranular network and elevated in the interior of granules. The r.m.s. of the height of this surface is 30 km, consistent with the value reported by Stein and Nordlund (1998), who also used numerical simulations to study solar granulation. We take the  $x$ - $y$  plane at which  $\langle \tau_{\text{Ross}} \rangle = 1$  (horizontal average of  $\tau_{\text{Ross}}$ ) to be  $z = 0$ , with  $z$  increasing upwards. This plane is 450 km below the top boundary. Defining the pressure scale-height as  $H_p = (d \ln p / dz)^{-1}$ , the number of pressure scale heights between the bottom boundary and the visible surface is  $N(H_p) = \int dz / H_p = 5$ .

The colour-coding on the vertical plane on the right side of Fig. 3.1 shows the temperature distribution in that plane. Similarly, the colour-coding on the vertical plane on

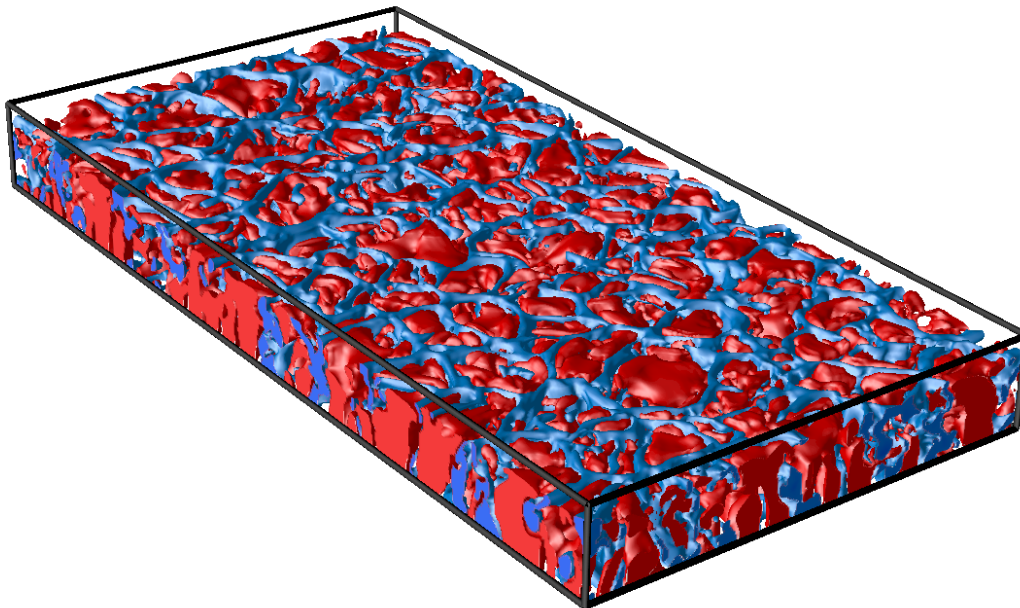


Figure 3.2: Topology of near-surface convection. The red isosurfaces indicate upflow regions and the blue isosurface indicates the downflow regions. The strong downflows form a connected network, which separates the upflowing material into disjoint upwellings.

the left side of this figure shows the specific entropy distribution in that plane. We discuss this in more detail in Section 3.3.3.

### 3.3.1 Topology of near-surface convection

Figure 3.2 shows isosurfaces of the kinetic energy density of the vertical component of velocity  $\frac{1}{2}\rho v_z^2 = 8125 \text{ erg cm}^{-3}$ . For the mean surface density of  $\langle \rho \rangle = 2.6 \times 10^{-7} \text{ g cm}^{-3}$ , this kinetic energy density corresponds to a vertical speed of  $2.5 \text{ km s}^{-1}$ . The isosurfaces coloured red indicate upflow regions and the isosurface coloured blue indicate downflow regions. This figure shows that the upflows are broader and the downflows are narrower. The downflow network consists of lanes, which outline the granules, and vertices, which connect the lanes. The asymmetry between the upflows and the downflows is a robust feature of compressible convection in a stratified medium: ascending material expands and descending material is compressed. For a convecting flow in statistical equilibrium, the net mass flux crossing a horizontal plane is close to zero. This requires the narrow downflows to have larger speeds than the broad upflows. Between  $z = 0$  and  $z = -300 \text{ km}$ , downflows have typical speeds of  $4 - 8 \text{ km s}^{-1}$  whereas upflows have typical speeds of only  $2 - 4 \text{ km s}^{-1}$ . Since the downflows are more compact and faster, they are able to penetrate through upflowing regions and separate them into disjoint upwellings.

Figure 3.2 shows that the intergranular downflows reach down to the bottom boundary of the simulation domain. The simulation domain of Stein and Nordlund (1998) reaches down to  $2.5 \text{ Mm}$  below the visible surface. In their simulations, the downflows also reach the bottom boundary. At the moment, it is unclear just how far the surface-driven



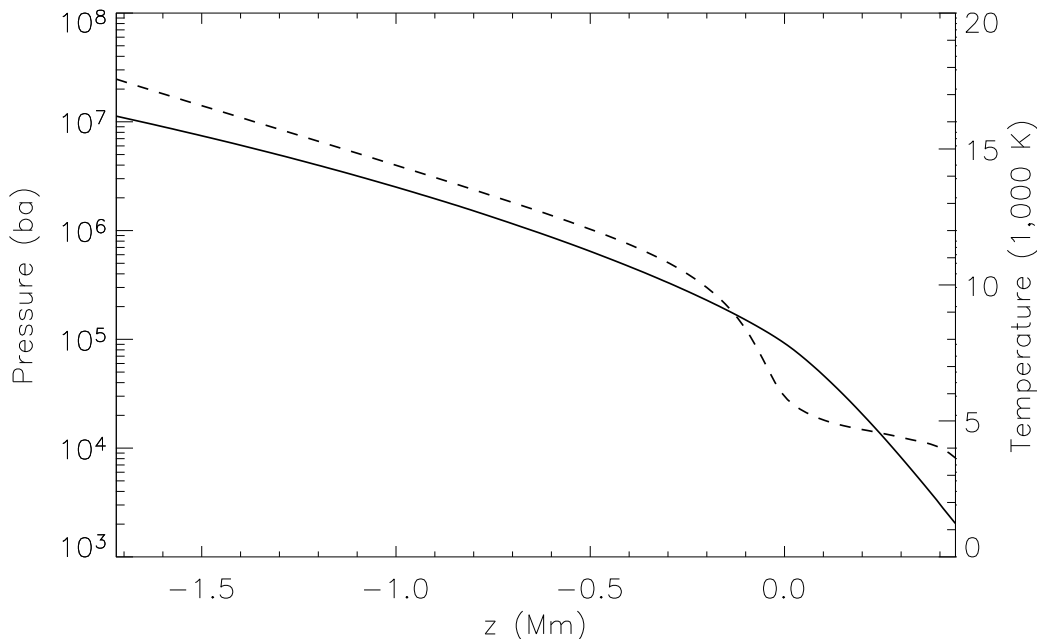


Figure 3.3: Horizontally averaged pressure (solid) and temperature (dashed) as functions of  $z$ .

downdrafts can penetrate into the convection zone. Although there are theoretical reasons suggesting that at even greater depths, coherent downdrafts will self-organize and merge into stronger downdrafts (Spruit et al. 1990), it is a hypothesis that remains to be confirmed or refuted by future simulations and helioseismic observations.

### 3.3.2 Logarithmic temperature and density gradients

In the original version of the MURaM code (Vögler et al. 2005), the EOS was described by the two look-up tables  $T(\epsilon, \rho)$  and  $p(\epsilon, \rho)$ . This is sufficient for the code to run. In this study, we are interested in using additional thermodynamic quantities as aids for analyzing the simulations. As is shown in Appendix A, a number of important thermodynamic quantities can be readily calculated from the look-up tables for temperature and pressure. The specific entropy  $s$  and the adiabatic temperature gradient  $\nabla_{\text{ad}}$ , for example, are particularly useful because they are related to adiabatic processes.

The horizontally averaged temperature and pressure as a function of  $z$  are shown in Fig 3.3 as dashed and solid curves respectively. Figure 3.4 shows the corresponding logarithmic temperature gradients:

$$\nabla := \frac{d \ln T}{d \ln p}, \text{ and} \quad (3.25)$$

$$\nabla_{\text{ad}} := \left( \frac{\partial \ln T}{\partial \ln p} \right)_s. \quad (3.26)$$

$\nabla$  (solid black curve) is the actual average temperature gradient in the simulation and  $\nabla_{\text{ad}}$

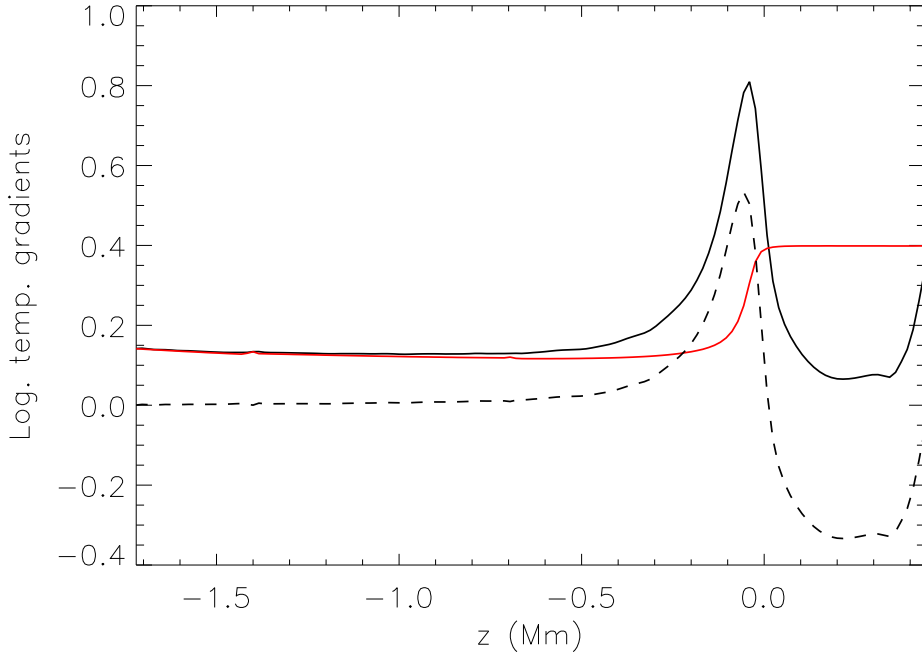


Figure 3.4: Logarithmic temperature gradients  $\nabla$  (solid black curve),  $\nabla_{\text{ad}}$  (solid red curve) and the super/sub-adiabaticity  $\delta_T = \nabla - \nabla_{\text{ad}}$  (dashed curve).

(solid red curve) is the adiabatic temperature gradient.  $\nabla_{\text{ad}}$  describes the variation of temperature of a fluid element undergoing adiabatic expansion or compression. It is related to Chandrasekhar's second adiabatic exponent by  $\gamma_2 = (1 - \nabla_{\text{ad}})^{-1}$  (see Appendix A.5).

The super/sub-adiabaticity is defined as  $\delta_T := \nabla - \nabla_{\text{ad}}$ . This quantity is plotted as a dashed curve in Fig. 3.4. In the special case that the gas is completely neutral or completely ionized, all three of Chandrasekhar's adiabatic exponents converge to the same quantity  $\gamma$ , which is equal to the ratio of specific heats  $c_p/c_v$ . In the photosphere, the chemical species are almost completely neutral. Since molecules have not been taken into account in our EOS, the gaseous mixture in our model is monatomic. For a monatomic gas,  $\gamma = 5/3$  and so in our model photosphere,  $\nabla_{\text{ad}} = 1 - 1/\gamma = 0.4$ . As we go deeper into the convection zone, the ionization fraction of hydrogen (and traces of other species) increases. This has the effect of decreasing the adiabatic temperature gradient, so that  $\nabla_{\text{ad}} < 0.4$ .

The (in-)stability of the stratification to convective motion is influenced by changes in the ionization state. Consider the classical picture of a parcel of gas in an average background stratification. Initially, it has the same density and pressure as its surroundings. Let it be displaced vertically and let it do so adiabatically. If, upon ascent (descent), the parcel gains a density deficit (excess) relative to the surroundings, the buoyancy force accelerates the parcel in the same direction as its motion. In this case, the stratification is said to be unstable the convective instability. Formulated mathematically, the criterion for instability is

$$\nabla_{\rho, \text{ad}} > \nabla_{\rho} \quad (3.27)$$



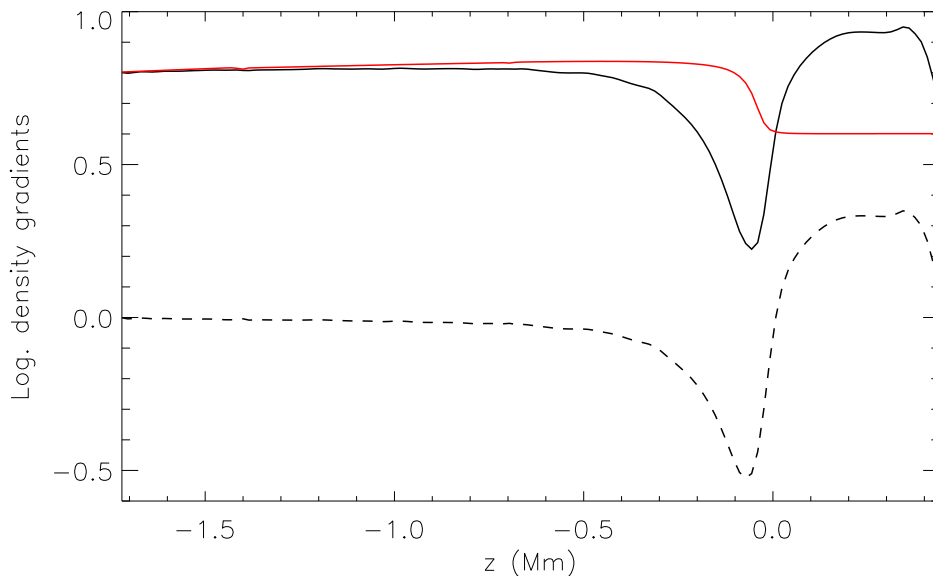


Figure 3.5: Logarithmic density gradients  $\nabla_\rho$  (solid black curve),  $\nabla_{\rho,\text{ad}}$  (solid red curve) and their difference  $\delta_\rho = \nabla_\rho - \nabla_{\rho,\text{ad}}$  (dashed curve).

where  $\nabla_{\rho,\text{ad}} := \left( \frac{\partial \ln \rho}{\partial \ln p} \right)_s = 1/\gamma_1$  is the density response of the parcel and  $\nabla_\rho := \frac{d \ln \rho}{d \ln p}$  is the actual density gradient in the background atmosphere. In analogy with the super/sub-adiabaticity  $\delta$ , we call the difference between these two terms  $\delta_\rho := \nabla_\rho - \nabla_{\rho,\text{ad}}$ . Fig. 3.5 shows these three quantities as functions of  $z$  in our 3D model. The region  $z < 0$  (i.e. the convection zone) has  $\delta_\rho < 0$  and is convectively unstable. The photosphere ( $z > 0$ ), in contrast, is stable to the convective instability since  $\delta_\rho > 0$ . The quantity  $\delta_\rho$  is indicative of the amount of buoyancy driving in the unstably stratified layers. After a parcel of gas has been displaced from its equilibrium position  $z_0$  by a vertical distance  $\Delta z$ , the ratio of the internal density of the parcel  $\rho_i$  with respect to the external density  $\rho_e$  is given by

$$\ln \left[ \frac{\rho_i}{\rho_e} \right]_{z_0+\Delta z} = - \int_{z_0}^{z_0+\Delta z} \frac{\delta_\rho dz}{H_p}, \quad (3.28)$$

where  $H_p = (d \ln p / dz)^{-1}$  is the local pressure scale height.

Criterion (3.27) can be expressed in terms of the super/sub-adiabaticity  $\delta_T$  in the following way

$$\delta_T > 0. \quad (3.29)$$

This is the *Schwarzschild criterion* for convective instability. Inspection of the height dependence of  $\delta_T$  in Fig. 3.4 indeed shows that  $\delta_T$  is positive in the convection zone and negative in the photosphere.

### 3.3.3 Specific entropy distribution

In the convection zone (in the simulation domain), the upflows have a typical specific entropy  $s_{\text{up}} \approx 6.0R^*$  (recall  $R^*$  is the universal gas constant). Downflows, which are

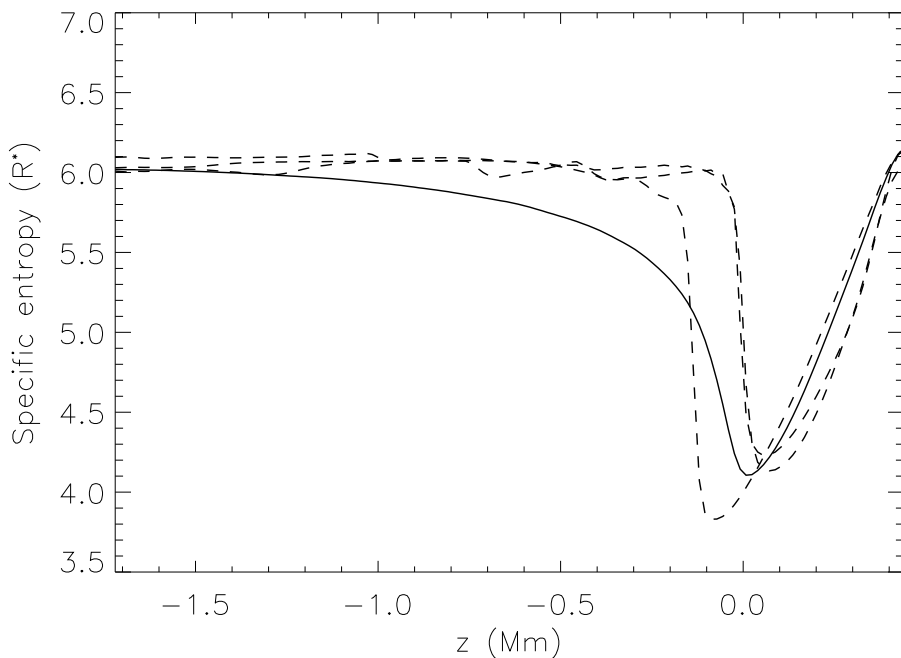


Figure 3.6: Vertical profiles of the specific entropy. The solid curve shows the horizontally averaged profile as a function of height  $z$ . The dashed curves show examples of vertical entropy profiles along upwellings. These profiles show that below the visible surface, the upflows rise almost adiabatically.

cooler and denser, have lower entropy. Fig. 3.6 shows vertical profiles of  $s$  in the simulation domain. The solid curve shows the horizontally averaged profile as a function of  $z$ . The average profile of entropy is almost identical with that found by Stein and Nordlund (1998). This curve has a minimum very near to  $z = 0$  (where  $\tau_{\text{Ross}} = 1$ ). In the convection zone ( $z < 0$ ),  $ds/dz < 0$ . Above  $z = 0$ ,  $ds/dz > 0$ . Schwarzschild's criterion can be restated in terms of vertical gradients in specific entropy. When  $ds/dz < 0$ , the layer is convectively unstable to adiabatic perturbations and when  $ds/dz > 0$ , the layer is stable.

The dashed curves in Fig. 3.6 show some examples of vertical profiles of  $s$  inside upflowing regions. These curves show that, along upwelling regions (granules), the material ascends to the visible surface almost adiabatically. At optical depths  $100 \gtrsim \tau_{\text{Ross}} \gtrsim 1$ , the material loses entropy by radiative cooling. The corresponding thickness of this thermal boundary layer is about 150 km, comparable to the local pressure scale height. In the near surface layers, the dominant contributor to the opacity is negatively ionized hydrogen ( $\text{H}^-$ ). The opacity related to this species is highly temperature sensitive and decreases rapidly with temperature ( $\sim T^{10}$ ), so that when a fluid element of plasma cools, its opacity drops rapidly and the cooling is enhanced (Stein and Nordlund 1998). This is the reason why the thermal boundary layer between the convection zone and the photosphere is so thin. We have not shown vertical profiles along downflow regions because the downflows tend to be displaced horizontally as they descend and interact with the surrounding upflows.

### 3.4 The structure of the reversed granulation in the photosphere

Intensity maps in the visible continuum show bright granules and dark intergranular boundaries at the base of the photosphere ( $\tau_{\text{Ross}} = 1$ ). Intensity maps taken in the wings of the Ca II H & K lines reveal a similar pattern. In these intensity maps, the cells are in general co-incident with the surface granules, as are the boundaries. The intensity contrast, however, is reversed. (Evans and Catalano 1972, Suemoto et al. 1987, 1990). This effect, known as the *reversed granulation*, has also been observed in intensity maps of other photospheric spectral lines (Espagnet et al. 1995, Balthasar et al. 1990, Kucera et al. 1995). These observations indicate that the reversed granulation occurs already at a height of  $z \approx 150$  km. Recently, Rutten et al. (2004) carried out cross-correlations between time sequences of intensity maps from the G-band and the Ca II H line. They found that the anticorrelation between the two patterns is highest if the Ca II H intensity maps are time-delayed by 2 – 3 minutes with respect to the G-band intensity maps. Leenaarts and Wedemeyer-Böhm (2005) extended this analysis by synthesizing intensity maps for the blue continuum and Ca II H wing (in the LTE approximation) from numerical simulations of the photosphere and chromosphere. From the unsmoothed synthetic intensity maps, they found that the anticorrelation between the two does not vary significantly between a time delay of 0 and 2 minutes. The anticorrelation decreased for longer time delays. When the images were smoothed to 1.5 arcsec resolution, a time-delay of 2 – 3 minutes yielded a significantly higher value of the anticorrelation compared to no time delay. The result from both of these papers indicate that magnetic fields play no major role in the formation of the reversed granulation.

In this section, we study the reversed granulation in our 3D model. For lines (or regions thereof) that form in approximate LTE conditions, such as some Fe I lines and the wings of the Ca II H & K lines, fluctuations in line intensity are a proxy for diagnosing temperature fluctuations. An intensity excess in the intensity map corresponds to a temperature excess in the layer of the atmosphere in which the line forms. An inspection of the temperature fluctuations at different heights of the atmosphere allows one to ascertain the height at which the reversed granulation begins (Steffen et al. 1989).

The top row of Fig. 3.7 shows the relative temperature fluctuations at the surfaces  $\tau_{\text{Ross}} = 1$  (left column) and  $\tau_{\text{Ross}} = 0.1$  (right column). The bottom row of this figure shows the vertical velocity at the same surfaces. On average, the  $\tau_{\text{Ross}} = 0.1$  surface is 140 km higher than the  $\tau_{\text{Ross}} = 1$  surface. At  $\tau_{\text{Ross}} = 1$ , one finds the normal granulation pattern: the granules are hotter than their boundaries. At  $\tau_{\text{Ross}} = 0.1$ , the reversed granulation is already clearly visible: the cell boundaries are regions of temperature excess. When we inspect the velocity structure, we find that the cells at  $\tau_{\text{Ross}} = 0.1$  are upflowing regions. The cellular boundaries at this optical depth are downflows. This layer of the atmosphere is stably stratified (see section 3.3.2), which means vertical motion is suppressed by the stratification. The material in the cells in the higher layer originates from the granules at the base of the convection zone, and are overshooting into the stably stratified photosphere. This is the reason that the vertical flow speeds at  $\tau_{\text{Ross}} = 0.1$  are smaller than the vertical speeds at  $\tau_{\text{Ross}} = 1$ . Although the amplitude of the speeds are different, the granular pattern in terms of velocity is the same at both optical depths. So, we em-

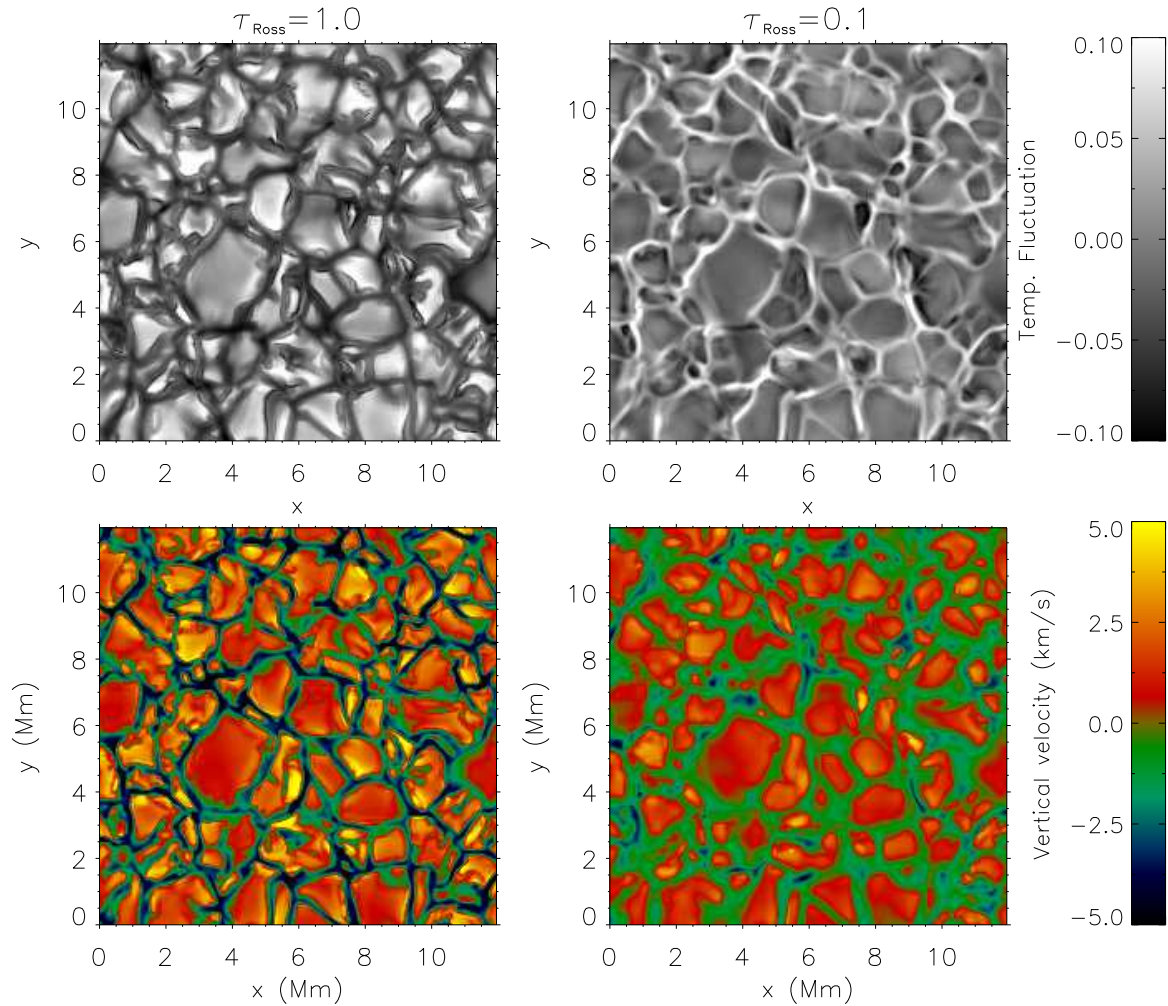


Figure 3.7: Patterns of temperature fluctuations ( $\Delta T/\bar{T}$ ) and vertical velocity at two different optical depths. The left column shows the patterns at  $\tau_{\text{Ross}} = 1$ , the right  $\tau_{\text{Ross}} = 0.1$ . The upper and lower rows show the temperature fluctuation and vertical velocity patterns respectively. The reversed granulation shows up as a reversal of the temperature fluctuations, but not in the velocity pattern.

phasize the point, that a reversal of the pattern of temperature (and intensity) fluctuations is *not* accompanied by a reversal of the velocity pattern.

We would like to determine the optical depth at which the reversed granulation begins. For each vertical line-of-sight (l.o.s.), we inspected the vertical velocity and temperature as functions of optical depth. To separate cell and boundary regions, we use the following classification: For a given l.o.s., if the plasma is upflowing at  $\tau_{\text{Ross}} = 1$ , the l.o.s. is labelled as one that penetrates a cell. This l.o.s. is then an element of the set  $L_{\text{cell}}$ . Similarly, if the vertical velocity along the l.o.s. is zero or negative at  $\tau_{\text{Ross}} = 1$ , the l.o.s. is binned into the set  $L_{\text{boundary}}$ . For each  $l$ , we have a profile of temperature as a function of optical depth. An average of the profiles at each optical depth over all l.o.s. (in both  $L_{\text{cell}}$  and  $L_{\text{boundary}}$ ) gives the mean temperature as a function of  $\tau_{\text{Ross}}$ , i.e.  $\bar{T}(\tau_{\text{Ross}})$ . Given this mean temperature profile, we can calculate the relative temperature fluctuation

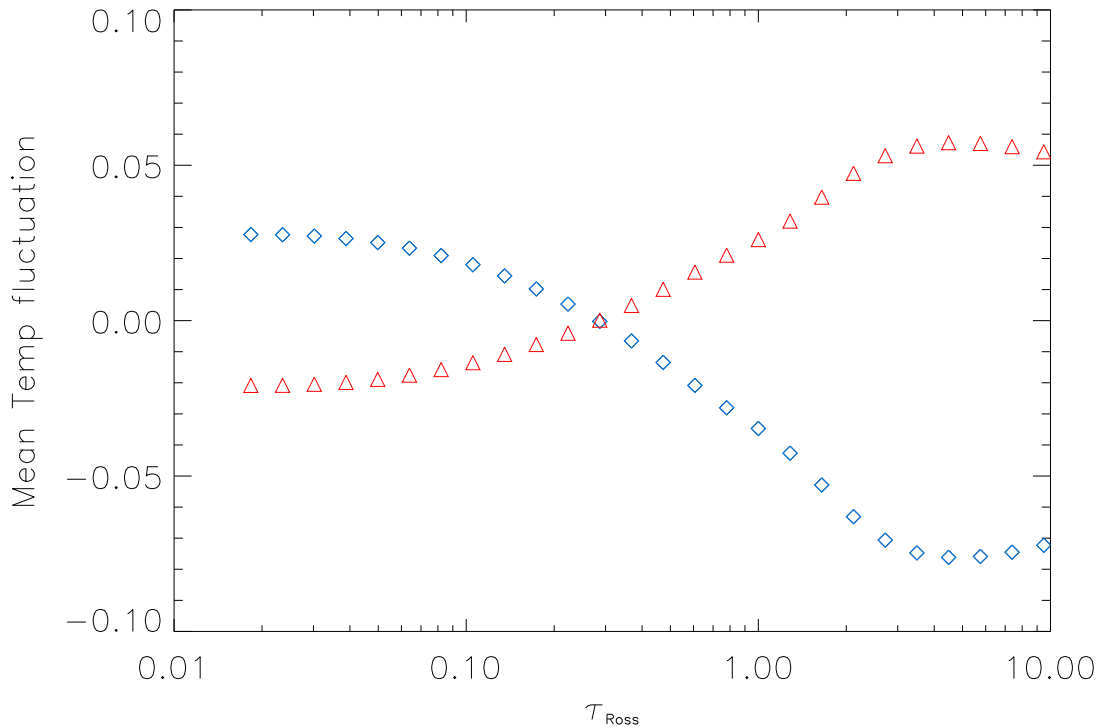


Figure 3.8: Mean temperature fluctuation of cells (blue diamonds) and of boundaries (red triangles) as a functions of optical depth. The reversed granulation begins at an optical depth of about  $\tau_{\text{Ross}} = 0.3$ .

$(\Delta T/\bar{T})$  at each optical depth for each l.o.s. We refer to the mean of the relative temperature fluctuations over the set  $L_{\text{cell}}$  ( $L_{\text{boundary}}$ ) as the mean temperature fluctuation in the cells (boundaries). These two quantities are plotted as functions of  $\tau_{\text{Ross}}$  in Fig. 3.8. The blue diamonds indicate the mean temperature fluctuation in the cells whereas the red triangles indicate the mean temperature fluctuation in the boundaries. These two are not simply the negative of each other because the cells and boundaries have different filling factors. Starting from  $\tau_{\text{Ross}} = 1$ , the temperature excess (deficit) of the cells (boundaries) diminishes with decreasing optical depth. At  $\tau_{\text{Ross}} \approx 0.3$ , the mean temperature fluctuations of both regions cross zero. At even shallower optical depths, the temperature fluctuation is reversed. This leads us to conclude that reversed granulation begins already at  $\tau_{\text{Ross}} \approx 0.3$ . On average, this level is 80 km above the base of the photosphere. This finding is in agreement with that of Suemoto et al. (1987), who concluded from observations in the inner wing of Ca II K that “the granular hotter layers do not extend higher than  $\tau \sim 0.3$  and that an intergranular hotter layer is located considerably higher than  $\tau \sim 0.3$ ”.

What is the cause of the reversed granulation? First, consider the following scenario. Suppose we have an atmosphere with a subadiabatically stratified layer sitting on top of a superadiabatically stratified layer. This is analogous to the photosphere/convection zone region. For the moment, we consider only adiabatic motion. When a parcel of fluid in the convection zone ascends, it gains a temperature excess relative to its surroundings.

When this parcel has crossed the interface and has moved into the stable layer, its temperature excess begins to diminish, until at a certain height in the stable layer, it has the same temperature as the surroundings. Since the parcel has finite vertical momentum, it will continue to move upwards. During this *overshoot* phase, the parcel becomes colder (and denser) than its surroundings and experiences a downwards acceleration. At a certain penetration height into the stable layer, the parcel will have zero vertical velocity but continues to be accelerated downwards. At this instant the parcel overturns and begins its return journey. Applying this model to the near-surface convection zone and the photosphere, we can explain the overturning of the granules in the photosphere. However, one is then led to believe that at any given height in the photosphere, the upflows and downflows have the same temperature. This scenario does not explain the reversal of the temperature fluctuations between the upflows and downflows.

In order to explain the reversed granulation, we must consider non-adiabatic effects associated with radiation in the photosphere. Fig. 3.9 shows a subvolume in the simulation domain in the neighbourhood of a granule (the one centred at  $[x, y] = [4, 5]$  Mm in Fig. 3.7). In both panels, the grey scale shows the vertical velocity at  $z = 0$  at the same instant. Overplotted are a set of streamlines emanating from this granule. The pattern of streamlines resemble a fountain: they begin near the centre of the granule, travel up to the photosphere and eventually overturn to the intergranular lanes. In the upper panel of this figure, the colour-coding of the streamlines corresponds to the value of  $s$  at each point on the curve (purple is low entropy, orange high entropy). In the lower panel, the colour-coding corresponds to the sign of  $Q_{\text{rad}}$  (dark blue means  $Q_{\text{rad}} < 0$ , yellow means  $Q_{\text{rad}} > 0$ ).

We have examined how different physical quantities vary along these streamlines. Fig. 3.10 shows profiles of  $s$  and  $T$  along a representative streamline. The left column shows the profiles as functions of  $z$  and the right column shows the profiles as functions of the optical depth  $\tau_{\text{Ross}}$ . The colour-coding of the curves gives the sign of  $Q_{\text{rad}}$  (c.f. Fig. 3.9).

Imagine a fluid element travelling on any one of these streamlines<sup>1</sup>. Its trajectory in the photosphere has the shape of a loop. In the convection zone ( $z < 0$ ), it has  $s = 6.0R^*$ . As it approaches the surface, between  $100 \gtrsim \tau_{\text{Ross}} \gtrsim 1$ , the fluid element loses entropy and buoyancy by radiative cooling. Nevertheless, it has vertical momentum and enters the photosphere ( $z > 0$ ). As it rises, the fluid element expands but its temperature decreases at a subadiabatic rate because the fluid element is continually being heated by the radiation field below ( $Q_{\text{rad}} > 0$ ). This leads to an increase of  $s$  of the fluid element. At the apex of its trajectory, the fluid element overturns. The exact height at which the fluid element overturns is determined by the dynamics in the neighbourhood of the granule. In general, however, fluid elements that originate from near the centre of the granule are able to penetrate higher into the photosphere than those that originate near the edge of the granule.

The radiative heating of the fluid element does not stop at the apex of its trajectory. As Fig. 3.10 shows,  $Q_{\text{rad}}$  remains positive for a short distance at the beginning of its descent. The radiative heating, together with the compression of the fluid element as it reaches

<sup>1</sup>Since the flow is time-dependent, streamlines and trajectories do not coincide. We have repeated the following analysis on trajectories of tracer fluid elements in the simulation and confirmed that indeed the radiative heating is the main source of entropy change.



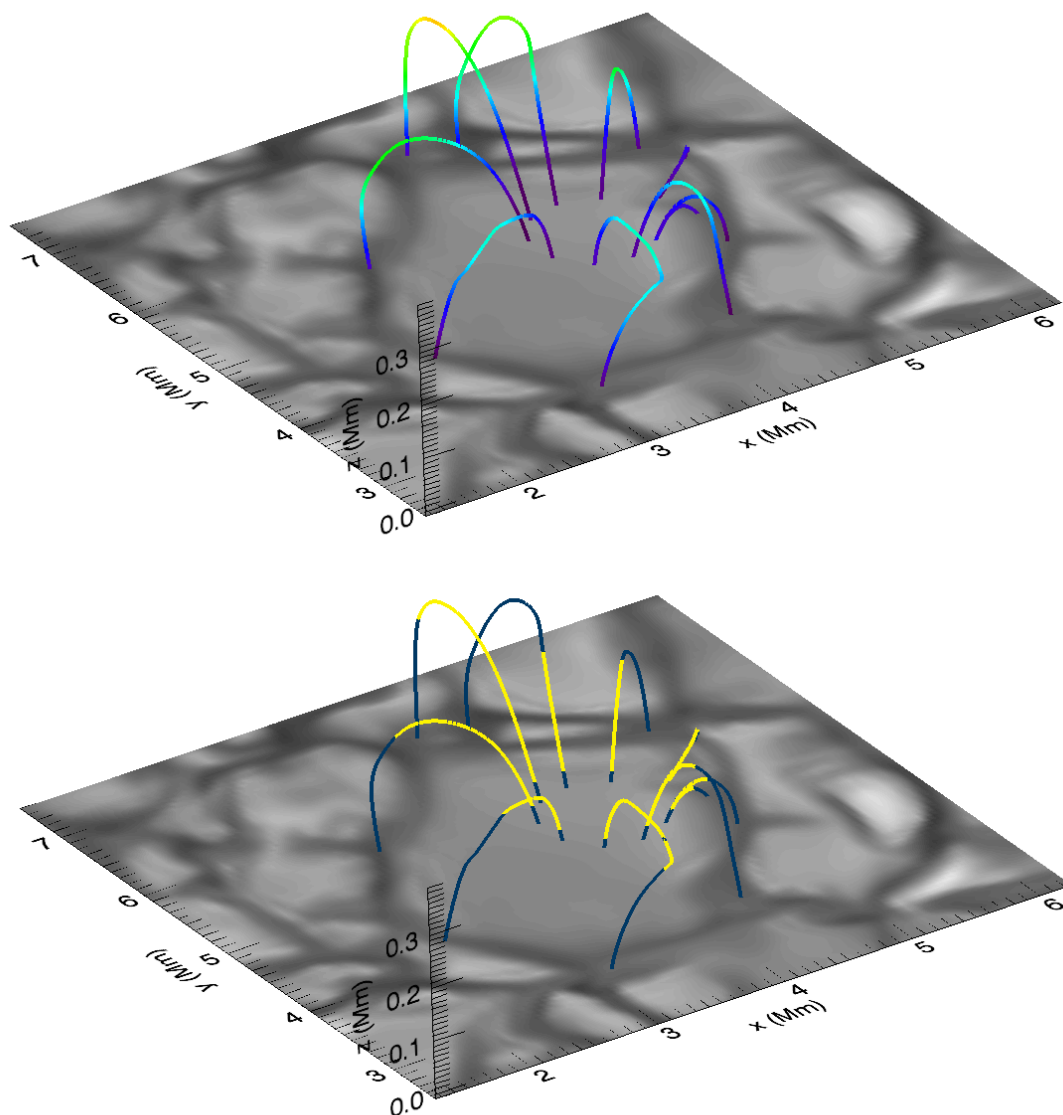


Figure 3.9: The upper and lower panels show the neighbourhood of a granule in the photosphere. In both panels, the grey scale shows the vertical velocity at  $z = 0$ . Streamlines beginning from the granule are colour-coded according to the local value of the specific entropy  $s$  (upper panel; purple is low entropy, orange high entropy) and the sign of  $Q_{\text{rad}}$  (lower panel; dark blue means  $Q_{\text{rad}} < 0$ , yellow means  $Q_{\text{rad}} > 0$ ).

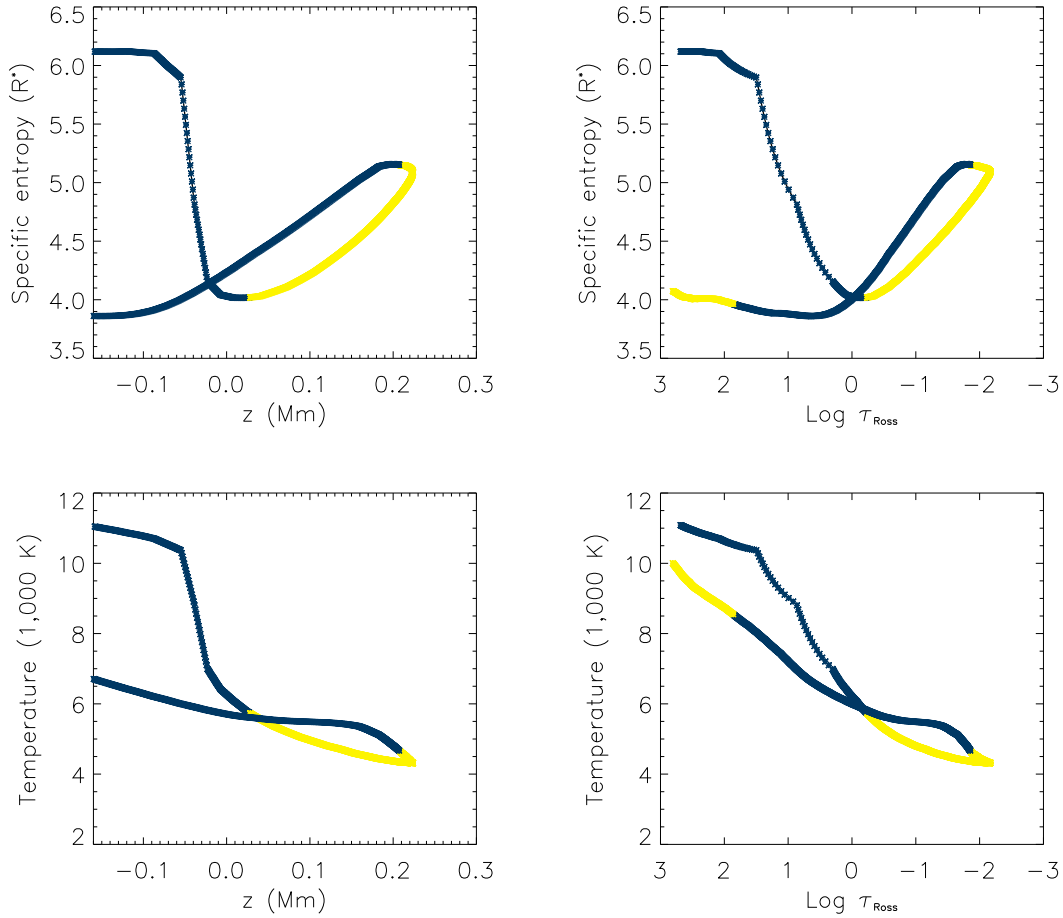


Figure 3.10: The profiles of specific entropy and temperature along a representative streamline shown in Fig. 3.9. The colour-coding of the curves correspond to the sign of  $Q_{\text{rad}}$  (dark blue means  $Q_{\text{rad}} < 0$ , yellow means  $Q_{\text{rad}} > 0$ ).

denser layers, leads to an increase of its temperature. At some point, the fluid element is sufficiently hot, so that it emits and absorbs radiation in equal rates (i.e.  $Q_{\text{rad}} = 0$ ). The fluid element is then in *radiative equilibrium*. The temperature at which this occurs is denoted by  $T_{\text{RE}}$ . When the fluid element has a higher temperature than  $T_{\text{RE}}$ ,  $Q_{\text{rad}}$  is negative. This is why the fluid element loses specific entropy as it returns to the base of the photosphere. The important point here is that the cumulative total of the heating (upon ascent and for a short while after overturn) and cooling (during descent) of the fluid element occur in unequal amounts. A fluid element that travels from  $z = 0$  to the photosphere and back gains more entropy than it loses. This asymmetry is the cause for the reversed granulation: at the same geometrical height and optical depth in the photosphere, the downflows (cell boundaries) are hotter than the upflows (cells).

An estimate for the lower bound of  $T_{\text{RE}}$  is possible when we assume the fluid element to be located at  $\tau_{\text{Ross}} = 0$ . Recall that  $Q_{\text{rad}} = \int_0^\infty 4\pi\kappa_\nu\rho(J_\nu - B_\nu)d\nu$ . In the approximation of grey radiative transfer,  $\kappa_\nu$  is replaced by the mean opacity  $\bar{\kappa}$ , so that

$$Q_{\text{rad}} = 4\pi\bar{\kappa}\rho[J - B(T)], \quad (3.30)$$



where  $B(T) = \int_0^\infty B_\nu(T) d\nu = (\sigma/\pi)T^4$  is the frequency-integrated Planck function and  $J = (4\pi)^{-1} \int_{4\pi} \int_0^\infty I_\nu d\nu d\Omega$  is the angular-averaged, frequency-integrated intensity. Assume that the solar atmosphere has plane-parallel symmetry. In this case,  $I_\nu$  is symmetric about the  $z$ -axis. Making use of the Eddington-Barbier approximation, we obtain

$$J = \frac{1}{4\pi} \int_0^\infty \oint_{4\pi} I_\nu d\Omega d\nu, \quad (3.31)$$

$$= \int_0^\infty \left[ \frac{1}{2} \int_{-1}^1 B_\nu(T|_{\tau=\mu}) d\mu \right] d\nu, \quad (3.32)$$

$$= \frac{\sigma}{2\pi} \int_{-1}^1 (T|_{\tau=\mu})^4 d\mu, \quad (3.33)$$

where  $\mu = \boldsymbol{\mu} \cdot \hat{\boldsymbol{z}} = \cos \theta$ .  $T_{\text{RE}}$  is defined so that  $Q_{\text{rad}} = 0$ . That is,  $B(T_{\text{RE}}) = (\sigma/\pi)T_{\text{RE}}^4 = J$ . To evaluate  $J$ , we use our model and calculate the average temperature  $\langle T \rangle$  at different values of  $\tau_{\text{Ross}}$ . This yields  $T_{\text{RE}} = 4600$  K. Inspection of  $T$  and  $Q_{\text{rad}}$  along the streamlines shows that typical values of  $T_{\text{RE}}$  lie between 4600 and 5000 K. The higher values of  $T_{\text{RE}}$  in the simulation just reflects the fact that the fluid elements are located in the photosphere at finite optical depths. This analysis tells us that, even when a fluid element is descending in the photosphere, it will be heated by the radiation field as long as its temperature is below  $T_{\text{RE}} \approx 4600 - 5000$  K. Thus fluid elements that overturn at larger  $z$  will be heated more than those which overturn at lower  $z$ .

To summarize, the reversed granulation is a reversal of the pattern of intensity contrast between intensity maps in the continuum and intensity maps in spectral lines forming in the middle to upper photosphere. This is linked to a reversal of the temperature fluctuations with respect to height (see Fig. 3.8). The downflows in the cellular boundaries are relatively cooler than the upflowing granules for  $\tau_{\text{Ross}} > 0.3$ . For  $\tau_{\text{Ross}} < 0.3$ , the boundaries are relatively hotter. This reversal in the temperature contrast is explained by the radiative heating and cooling of convective plasma overturning in the photosphere. This study confirms the conclusion by Rutten et al. (2004) and Leenaarts and Wedemeyer-Böhm (2005) that surface magnetism plays an insignificant role in the formation of the reversed granulation.



## 4 Photospheric flux emergence: 2-dimensional simulations

In Chapter 2, we presented a study of the rise of horizontal magnetic flux tubes in a stratified layer. The simulations in that study are idealized: the convection zone is modelled by a polytrope; the medium has the properties of an ideal gas; and radiative energy exchange is not included. To realistically model photospheric flux emergence, these idealizations must be abandoned. In this chapter, we present results from 2D simulations that include these two effects. The simulations model the rise and emergence of a magnetic flux tube initially embedded in the sub-photospheric layers. The convective motion of the background material in the convection zone is not included. The effect of magneto-convection is discussed in subsequent chapters, where we presents results from 3D simulations.

### 4.1 Simulation setup

The simulations here were carried out in a 2D cartesian geometry. The components of the velocity and magnetic field in the  $y$ -direction (parallel to tube axis) may be non-vanishing, but  $\partial/\partial y$  of all quantities are identically zero. Often, such a setup is referred to as 2.5D. For these simulations, the MHD equations (3.1)-(3.5) and the RTE are solved. We consider a simulation domain with a horizontal size of 24 Mm and a height of 2.304 Mm. The grid-spacing in the horizontal and vertical directions is 50 and 16 km, respectively.

#### 4.1.1 Boundary conditions

Periodic boundary conditions are imposed at the vertical boundaries. The boundary condition at the lower boundary is identical to the one used for the 3D convection model of Chapter 3. The magnetic field at the lower boundary is kept vertical.

For the following simulations, we have modified the top boundary condition to allow for the bodily transport of magnetic field through the top boundary. This is important because we do not want the emerged magnetic field to be artificially trapped in the photosphere. In principle, stress-free conditions on all three components of the velocity at the upper boundary, i.e.

$$\frac{\partial v_x}{\partial z} = \frac{\partial v_y}{\partial z} = \frac{\partial v_z}{\partial z} = 0, \quad (4.1)$$

suffice for a smooth outflow. This condition, however, is independent of whether the mass flux through the upper boundary is appropriate or unrealistically high. In order that the mass flux be kept at appropriate levels, additional constraints must be applied. To this

end, we follow Stein and Nordlund (1998) and implement a *fiducial layer* above the top boundary of our simulation domain.

The bottom surface of our fiducial layer is co-incident with the horizontal plane containing the cell centres of the first ghost layer above the top domain boundary. To simplify the following discussion, let us use the position of this plane as the reference height, i.e.  $z = 0$  at the bottom of the fiducial layer. Using this reference, the height of the cell centres in the uppermost domain layer is  $z = -h$ , where  $h$  is the vertical grid-spacing. We impose that each vertical column of the fiducial layer be isothermal and be in hydrostatic equilibrium. This means that each column of mass in the fiducial layer follow an exponential decay with height,

$$\rho(x, y, z) = \rho(x, y, 0)e^{-z/\hat{H}_p}, \quad z \in [0, 3\hat{H}_p] \quad (4.2)$$

where  $\hat{H}_p$  is the pressure scale height evaluated at the uppermost domain layer. The fiducial layer has a thickness of  $3\hat{H}_p$ . Our aim is to specify an appropriate density distribution  $\rho(x, y, 0)$  at the bottom of the layer in order to fill the values of density in the ghost cells. To do this, we keep track of the total mass enclosed in the fiducial layer. By imposing the stress-free condition (4.1) on the velocity everywhere within the fiducial layer, we can determine the mass fluxes through the bottom and top surfaces of the layer. The total mass in the layer is given by

$$M_{\text{fid}} = \int_0^{3\hat{H}_p} \int \int \rho(x, y, z) dx dy dz, \quad (4.3)$$

$$= \bar{\rho}_0 \hat{H}_p A [1 - e^{-3}], \quad (4.4)$$

where  $A$  is the area of a horizontal plane in the domain and  $\bar{\rho}_0 = A^{-1} \int \int \rho(x, y, 0) dx dy$  is the mean density at the bottom of the fiducial layer. Expression (4.4) relates the mass of the fiducial layer with the mean density  $\bar{\rho}_0$  at the bottom of the layer. We require that density perturbations in the fiducial layer follow the same horizontal distribution as the corresponding perturbations in the uppermost domain layer. Let us denote the mean density in the uppermost domain layer as  $\bar{\rho}_D$ . Our requirement means that

$$\rho(x, y, 0) = \left[ \frac{\bar{\rho}_0}{\bar{\rho}_D} \right] \rho(x, y, -h). \quad (4.5)$$

At each time step, the r.h.s. of the above expression is calculated and Eqs. (4.2) and (4.5) are used to specify the density in the ghost cells. By keeping track of  $M_{\text{fid}}$ , we give memory to the fiducial layer. When too much mass has crossed from the domain into the fiducial layer,  $\bar{\rho}_0$  becomes larger than  $\bar{\rho}_D$  and so the stratification near the top boundary becomes top-heavy. Any further mass outflow through the top boundary is then suppressed by gravity. Conversely, in case too much mass has drained from the fiducial layer into the domain,  $\bar{\rho}_0$  becomes much smaller than  $\bar{\rho}_D$ , inducing a upwards directed pressure gradient that overcomes gravity to drive an outflow from the domain into the fiducial layer.

Besides the density, we also need to specify the values of the specific internal energy  $\epsilon$  in the ghost layers. This quantity is taken to be uniform over the fiducial layer. At a particular time step  $n$ , we specify this quantity in the ghost cells using

$$\epsilon^n = [1 - \delta] \epsilon^{n-1} + \delta \bar{\epsilon}_D^n, \quad (4.6)$$

where  $\epsilon^{n-1}$  is the value from the previous time step and  $\bar{\epsilon}_D^n$  is the horizontally-averaged value evaluated in the uppermost domain layer at time step  $n$ . The small quantity  $\delta$  can be varied to control how quickly we allow  $\epsilon$  in the ghost layers to adjust to the values in the domain. In all the simulation runs described in the following, we used  $\delta = 10^{-3}$  so that the adjustment is slow. This is desirable because we do not wish our fiducial layer to excite waves with periods comparable to the magnetohydrodynamic time scales of interest in the simulations.

The magnetic field above the upper boundary of the domain is matched to a potential field. This requires an extrapolation of the magnetic field in the uppermost domain layer into the ghost cells at each time step. The method we used for the field extrapolation is appropriate for both potential fields and more generally, linear force-free fields. For further details, we refer the reader to Appendix C.

### 4.1.2 Initial conditions

The background stratification in the domain is initially plane-parallel and static. The horizontally-averaged profiles of  $\epsilon$  and  $\rho$  as functions of height were taken from the 3D model of Chapter 3. In the presence of convection, as is the case with the 3D model, the energy flux carried by radiation at the surface is maintained by a continuous replenishment of upwelling, high-entropy material. This process keeps the average height of the visible surface approximately constant. Since there is no convection in the initial configuration here, the cooling of the visible surface causes the visible surface to sink in the course of the simulation. In the following simulations, the visible surface sinks by between 100 and 300 km over a duration of 25 minutes (the typical time scale of an emergence event). This side effect has relatively unimportant consequences compared with the alternative option, which would be a removal of the radiative heating term from the energy equation. Such a modification would eliminate what is arguably the most interesting result of this set of simulations, namely, the effect of radiative transfer on an emerging flux tube.

At  $t = 0$ , an axisymmetric magnetic flux tube was introduced into the sub-photospheric layers. The longitudinal and transverse components of the magnetic field have the form:

$$B_l(r) = B_0 \exp(-r^2/R_0^2), \quad (4.7)$$

$$B_\theta(r) = \frac{\lambda r}{R_0} B_l, \quad (4.8)$$

where  $r \in [0, 2R_0]$  is the radial distance from the tube axis and  $R_0$  the radius of the tube. Its longitudinal flux is given by  $\Phi_0 = \int B_l dS = 0.98\pi R_0^2 B_0$ .  $\lambda$  is the twist parameter. In the absence of the magnetic field, the divergence of the total stress tensor (viscous + Maxwell + pressure) is zero. Since we are primarily interested in studying the buoyant rise of the flux tube, we require that this condition holds when the flux tube is introduced. In such a case, the flux tube experiences only the gravitational force at time  $t = 0$ . Since the magnetic field contributes to the total pressure locally, the gas pressure in the flux tube must be decreased accordingly. Additionally, the magnetic tension of the transverse field (if present) exerts a force directed radially inwards, which must be balanced by an appropriately chosen pressure distribution. Having specified the internal gas pressure distribution, one is still free to choose the distribution of *one and only one* of the following

thermodynamic properties:  $\rho$ ,  $s$  or  $T$ . Choosing a distribution for any one of these quantities constrains the distributions of the remaining two.

## 4.2 Simulation results

In this section, we describe in detail results from two simulation runs. In both of these runs, the flux tube has  $B_0 = 8500$  G,  $R_0 = 200$  km and  $\Phi_0 = 10^{19}$  Mx. The flux tubes have the same internal specific entropy as the average value for the upflows in the 3D model of Chapter 3 ( $s = 6.0R^*$ ). Both are placed 1.35 Mm below the visible surface at  $t = 0$ . In the first run, the flux tube is untwisted ( $\lambda = 0$ ). In the second run, the flux tube has twist ( $\lambda = 0.5$ ). The relative density deficit is largest at the axes of the tubes, about 40%. In both cases, the density deficit averaged over the whole tube is much smaller, about 5%.

### 4.2.1 Dependence of emergence morphology on twist

Figures 4.1 and 4.2, respectively, show time sequences of the emergence of the untwisted ( $\lambda = 0$ ) and the twisted ( $\lambda = 0.5$ ) flux tube. In both figures, the temperature distribution of the background stratification is shown in greyscale. The absolute field strength  $|B|$  is indicated by the colour-coding. In each panel, the  $\tau_{\text{Ross}} = 1$  level is indicated by a purple line running across the horizontal extent of the domain.

We first describe features that are common to both simulations. In both cases, the buoyancy force accelerates the flux tube upwards. The buoyant acceleration of each flux tube is accompanied by a co-acceleration of non-magnetic material above it. The upwards displacement of non-magnetic material above the tube is indicated by the local elevation of the  $\tau_{\text{Ross}} = 1$  level (see the snapshots at  $t = 4$  min and  $t = 8$  min in Figs. 4.1 and 4.2) with respect to the average geometrical height of the same optical depth. Radiative cooling of material near the surface causes it to become denser than material in the underlying layer. This top heavy configuration is unstable to perturbations displacing material in the vertical direction. With the flux tube rising towards the surface, the overly dense material is able to descend by sliding around the rising tube. The sinking of the dense material into the superadiabatically stratified convection zone instigates the development of two downflows, one on either side of the emerging tube. In Figs 4.1 and 4.2, the two downflows show up as two ‘fingers’ of cool (dark in the greyscale) material reaching into the optically thick layers (i.e. the convection zone). The pressure deficit in the wake of the rising tube with respect to the surroundings gives a pressure gradient that deflects the developing downflows towards the wake.

The tube expands as it rises into layers of lower external pressure. In the convection zone, expansion in the vertical and horizontal directions occur at comparable rates. Once the magnetic structure has reached the surface, the expansion becomes markedly asymmetric with respect to the vertical and horizontal directions. The reason for this is simple: expansion in the vertical direction requires lifting of material into the stably stratified layer, which requires work to be done against gravity. This explanation follows that of Archontis et al. (2004), who carried out idealized simulations of flux emergence into the corona. To make the computation feasible, their simulations ignore radiative transfer

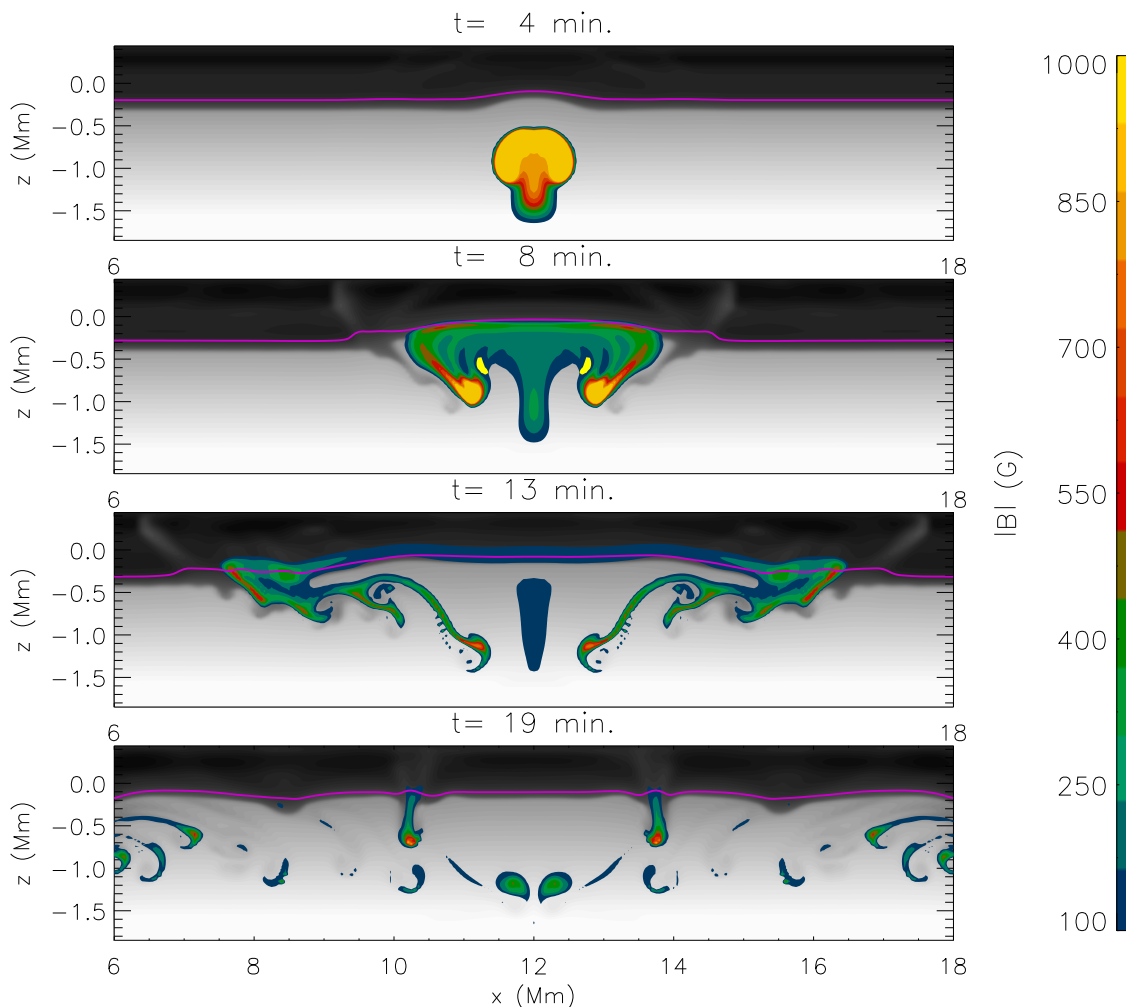


Figure 4.1: Time sequence of the emergence of an untwisted magnetic flux tube ( $\lambda = 0$ ). The background greyscale indicates the temperature stratification. The absolute field strength  $|B|$  is indicated by the colour-coding. In each of the panels, the purple line running across the horizontal extent of the domain indicates the  $\tau_{\text{Ross}} = 1$  level.

and convection in the layers underlying the corona. However, their background atmosphere does contain a stably stratified layer mimicking the photosphere. Although our simulation setups are different, both yield the result that a flux tube emerging into the photosphere expands preferentially in the horizontal direction.

The upper panel of Fig. 4.3 shows profiles of the longitudinal magnetic field  $B_l$  (upper panel) at  $t = 10$  min. The profiles were evaluated at the level of constant geometrical height ( $z = 0$  km). The solid and dashed lines show the profiles for the untwisted and twisted cases respectively. The profiles of  $B_l$  in the upper panel show that the twisted tube has a core with field strengths of up to 900 G. In comparison, the untwisted tube has a relatively weak field of 200 G.

The lower panel of Fig. 4.3 shows the corresponding profiles of the  $x$ -component of the velocity at  $t = 10$  min. The strong horizontal expansion of the emerging magnetic structure leads to the creation of two shock fronts propagating in opposite horizontal directions. This is illustrated by the profiles of the horizontal velocity in Fig. 4.3. The

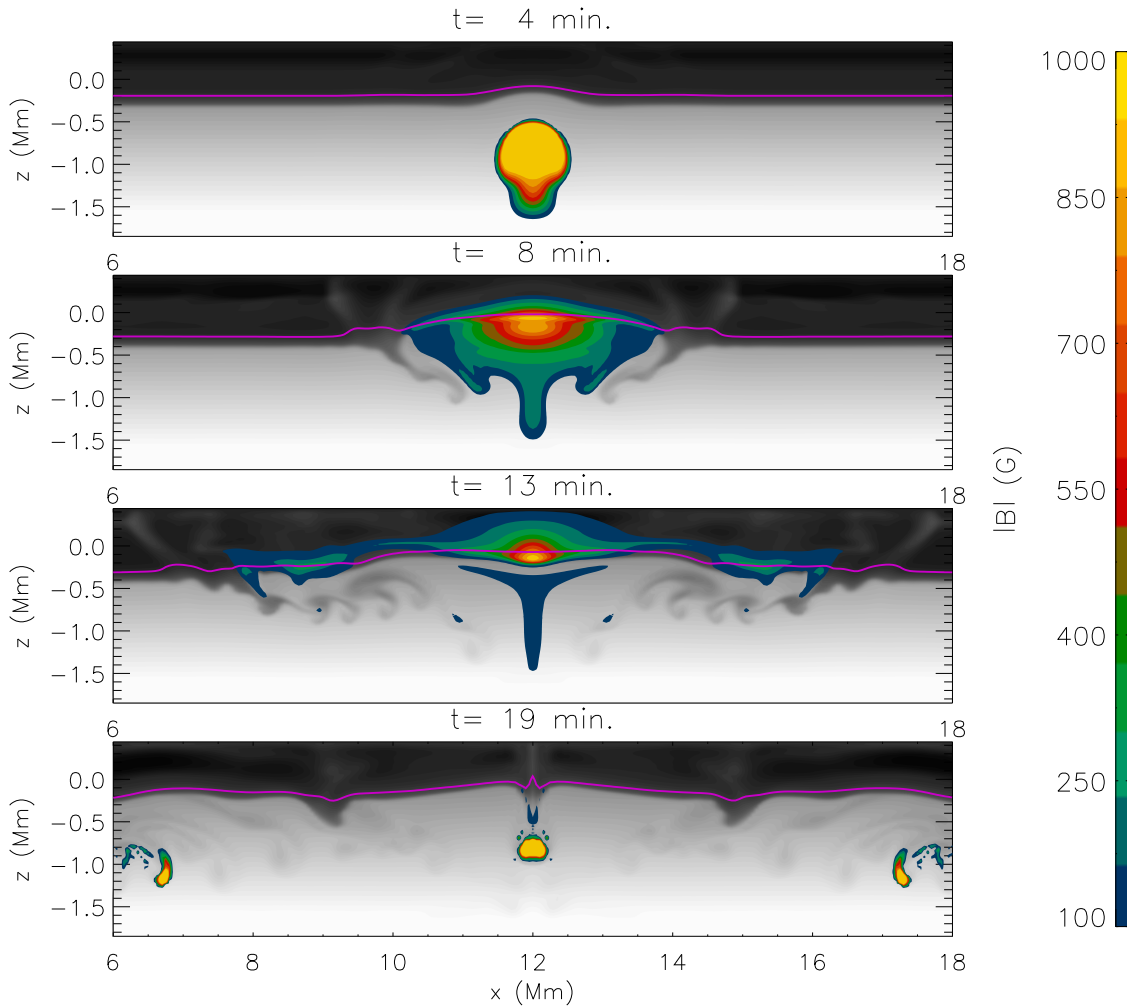


Figure 4.2: Same as Fig. 4.1, but for a twisted flux tube ( $\lambda = 0.5$ ).

horizontal velocity profile has maximum amplitude just *outside* the magnetic structure (compare with the upper panel of the same figure). The non-magnetic material residing immediately outside the tube can have speeds reaching  $10 - 15 \text{ km s}^{-1}$ , corresponding to Mach numbers of  $M \approx 1 - 2$ . The expanding flux tube acts like a piston, which does work on the surrounding non-magnetic material. The acceleration of the material in the neighbourhood of the tube is so strong that they reach supersonic speeds and shocks form. In Fig. 4.3, the pair of shock fronts propagating in opposite directions are centered at  $x = 9 \text{ Mm}$  and at  $x = 15 \text{ Mm}$  respectively. Viscous dissipation in the shock fronts lead to localized specific entropy production, enhanced temperature and radiative cooling.

The kinetic energy density in the supersonic outflows driven is several times larger than the kinetic energy density of the granular flow at the surface, which has typical horizontal speeds of  $2 - 4 \text{ km s}^{-1}$ . Suppose such a flux tube were to emerge at the solar surface. Its expansion would be so strong, that we expect the resulting outflows to modify the granulation pattern. Our 3D simulations of flux emergence, which will be presented in Chapter 5, indeed confirm this expectation.

From previous work in the literature (Schüssler 1979, Longcope et al. 1996) and from our study presented in Section 2.3.2, we know that an initially untwisted flux tube



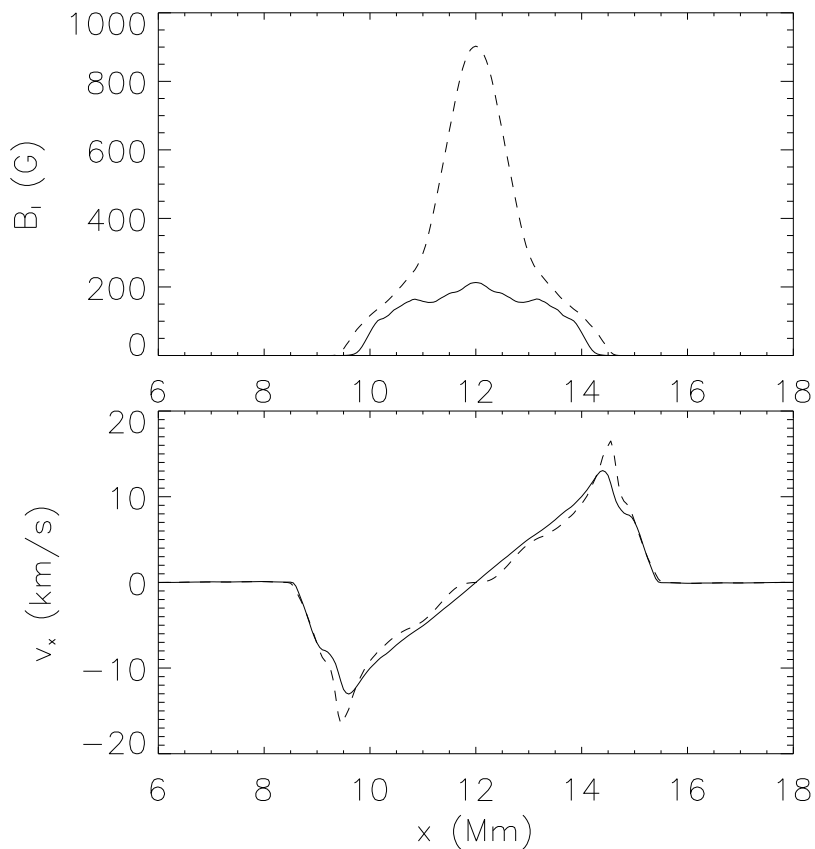


Figure 4.3: Profiles of the longitudinal magnetic field  $B_l$  (upper panel) and of the horizontal velocity  $v_x$  (lower panel), both taken at time  $t = 10$  min at the level  $z = 0$ . The solid lines and dashed lines indicate the profiles for the untwisted and twisted cases respectively.

rising under its own buoyancy separates into a pair of counter-rotating vortex rolls after transversing a distance a few times its diameter. A similar behaviour is found in the simulation presented in this chapter. By  $t = 8$  min, the initially untwisted tube (see Fig. 4.1) is separating into two vortex rolls. This is the reason that in Fig. 4.3, we find that in the twisted tube, the maximum of the longitudinal field is strongest in the core, whereas the longitudinal field in the untwisted tube is relatively weak.

#### 4.2.2 Intensification of emerging magnetic fields by radiative cooling

The inclusion of radiative transfer has interesting consequences for the evolution of the flux tube during emergence. Here, we focus our attention on describing the behaviour of the twisted flux tube with  $\lambda = 0.5$  (see Fig. 4.2) as it emerges at the visible surface. Since the flux tube in this case is twisted, we can apply the method as discussed in Section 2.2.4 to track the time evolution of physical quantities at the axis of the tube. Fig. 4.4 shows the field strength ( $|B|$ , upper panels) and the radiative heating rate per unit mass ( $Q_{\text{rad}}/\rho$ , lower panels) as functions of height (along the vertical  $x = 12$  Mm) at times  $t = 7.7$ ,

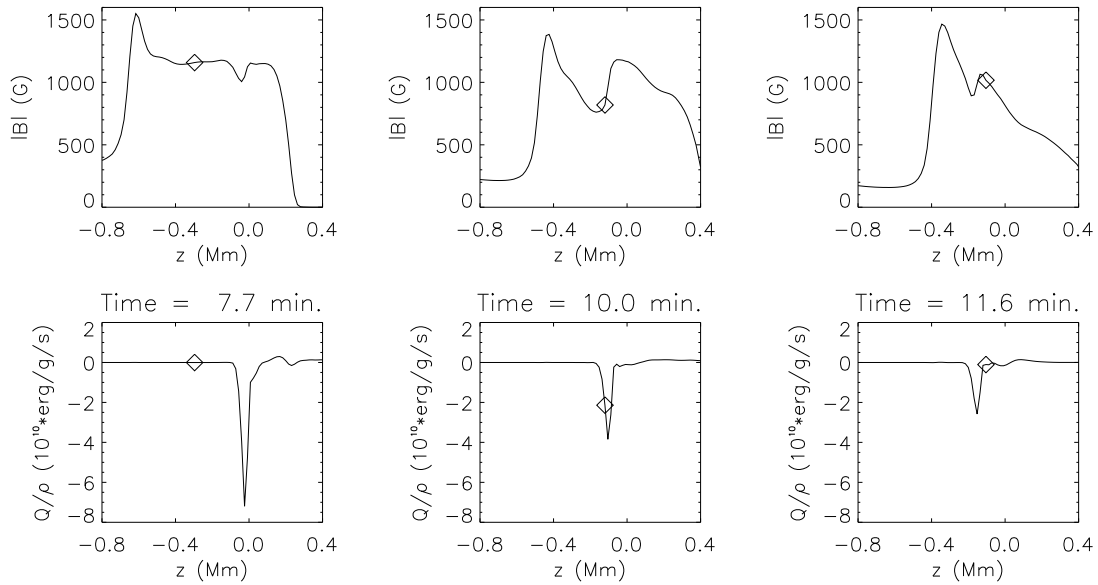


Figure 4.4: The propagation of the cooling front through the emerging tube leads to an intensification of the magnetic field strength. The three panels in the top row show  $|B|$  as functions of height (along the vertical  $x = 12$  Mm). The lower panels show the corresponding vertical profiles of the radiative heating rate per unit mass ( $Q_{\text{rad}}/\rho$ ). In each panel, the diamond indicates the position of the tube axis. The left, middle and right columns respectively correspond to the state of the flux tube before, during and after the cooling front has passed through the tube centre.

$t = 10.0$  and  $t = 11.6$  min. The diamond in each panel indicates the position of the tube axis. At each time, we find a narrow dip with a width of about 50 km in the profile of  $Q_{\text{rad}}/\rho$ . This corresponds to the thin cooling layer at optical depths  $1 \lesssim \tau_{\text{Ross}} \lesssim 100$  where the radiative cooling is most intense. In the following discussion, we refer to this feature as the *cooling front*. Located above the cooling front are the optically thin layers of the photosphere.

The sequence of profiles in Fig. 4.4 shows the propagation of the cooling front through the tube as it emerges into the photosphere. At  $t = 7.7$  min, the flux tube is beginning to emerge. By this time, the uppermost portion of the flux tube (parts of it above the cooling front) has already entered the photosphere but the axis of the tube is still in the convection zone. The field strength at the axis of the tube is  $|B| = 1,200$  G. As the centre of the tube continues to rise, its expansion weakens the local field strength. At  $t = 10.0$  min, the axis of the tube has  $|B| = 800$  G. The cooling front has already reached the tube axis. Equivalently, one can say that the axis of the tube is emerging at the surface. Thereafter, the cooling front continues to propagate through the lower portion of the tube. At  $t = 11.6$  min, we find that the tube axis has a field strength of  $|B| = 1,000$  G, higher than the value before the tube axis has emerged. This is despite the fact that the tube axis has reached layers of the atmosphere with lower external gas pressure. Thus, the radiative cooling has intensified the emerged magnetic field.

To emphasize the point made in the previous paragraph, we inspected the time evolu-

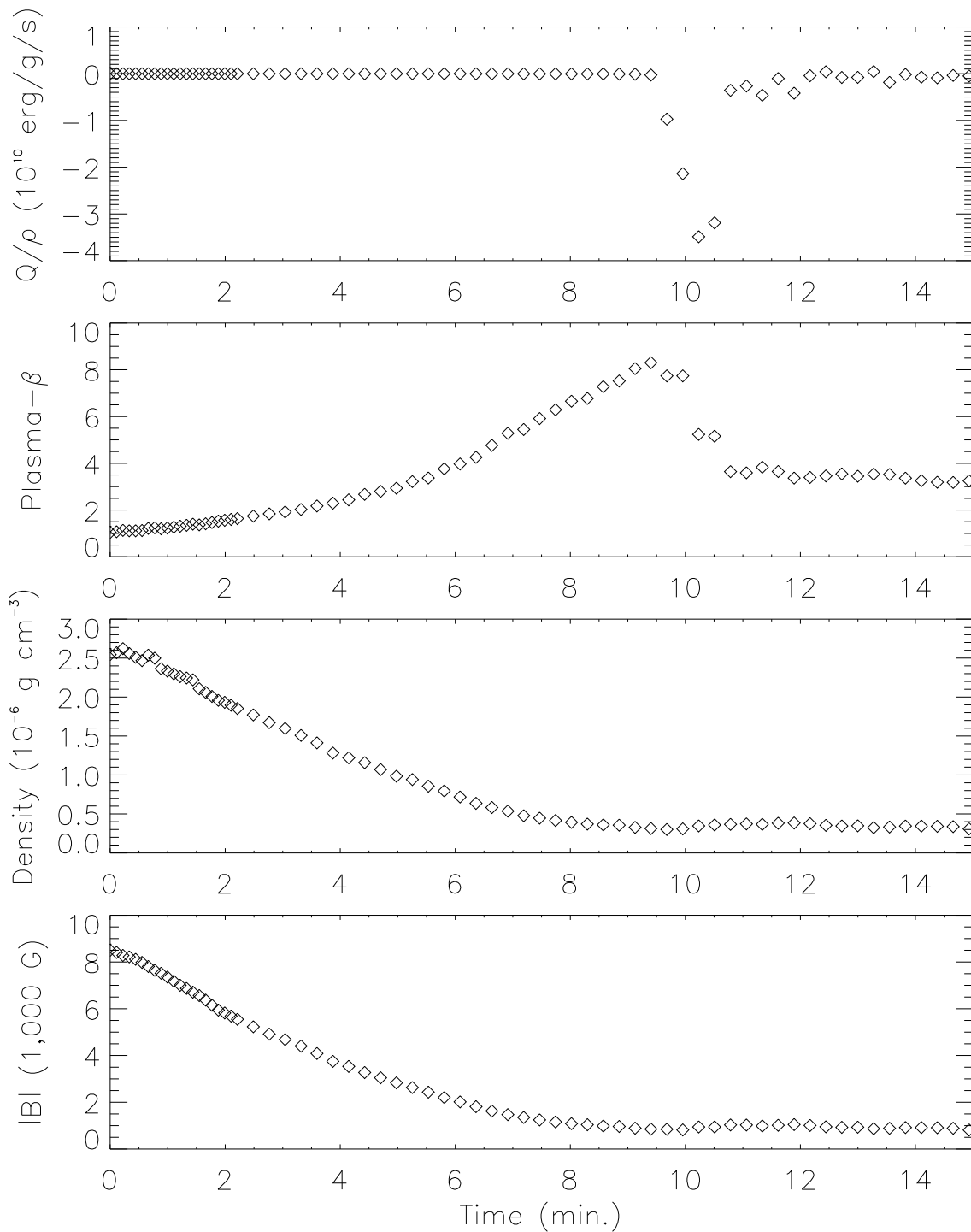


Figure 4.5: The radiative heating per unit mass ( $Q_{\text{rad}}/\rho$ ), the plasma- $\beta$ , the field strength  $|B|$  and the density  $\rho$  at the axis of the tube as functions of time. Between  $t = 9.5$  min and  $t = 11.0$  min, the tube axis undergoes substantial radiative cooling, leading to a compression. The result of the compression is an intensification of the magnetic field, in terms of both  $|B|$  and  $\beta$ .

tion of values of  $Q_{\text{rad}}/\rho$ ,  $\beta$ ,  $\rho$  and  $|B|$  taken at the tube axis. Fig. 4.5 shows these quantities as functions of time. The rise of the flux tube in the convection zone between  $t = 0$  and  $t = 9.5$  min is accompanied by a decrease in the density at the tube axis. The evolution of the magnetic field strength at the tube axis is approximately described by  $|B|/|B|_0 = \rho/\rho_0$  (see Section 2.3.1.2). In the limit of ideal MHD, we expect this relation to hold exactly. In numerical simulations, however, the effect of magnetic diffusion causes the field strength to fall slightly more rapidly than the density. In Appendix B, we calculated that the characteristic diffusion time scale for a flux tube of radius  $R_0$  is  $\tau = R_0^2/4\eta_0$ . For the value of the magnetic diffusivity used in these simulations ( $\eta_0 = 2.8 \times 10^{10} \text{ cm}^2\text{s}^{-1}$ ), this corresponds to  $\tau = 60$  min. The typical timescale for a flux tube to rise to the surface is about 10 min. Comparison of these timescale indicates that magnetic diffusion does not dramatically weaken the flux tube before it emerges.

The mechanism by which radiative cooling intensifies the field at the surface is as follows: A negative  $Q_{\text{rad}}$  in the energy equation decreases the internal energy of the fluid element. This in turn leads to a decrease in the local gas pressure. The resulting pressure gradient, which is directed towards the tube centre, drives a compression of the tube, increasing the internal density. Since the magnetic field strength is directly related to the density, the field is intensified. The second panel in Fig. 4.5 shows that the intensification of the field causes the plasma- $\beta$  to decrease from a value of 8 just below the surface to a value of 3 – 4 after emergence. Of course, the effect of this mechanism is not confined to the field at the tube axis, nor is it confined to intensifying just the longitudinal component of the field. When variations parallel to the field are allowed, as is in the 3D case, the intensification or weakening of the magnetic field need not be due to compression or expansion of the fluid element. A stretching of the fluid element in the direction parallel to magnetic field lines without changing the volume of the fluid element can also intensify the magnetic field.

### 4.2.3 Dependence of emerged flux on twist

The fraction of the initial longitudinal magnetic flux (crossing the plane) that successfully emerges into the photosphere depends on the initial twist of the tube. Let us define  $\Phi_{\text{photo}}(t)$  as the total longitudinal flux in the region  $\tau_{\text{Ross}} \leq 1$  in the simulation domain. Similarly, we define  $\Phi_{\text{conv}}(t)$  as the total longitudinal flux in the region  $\tau_{\text{Ross}} > 1$  in the domain. Since the top and bottom boundaries allow the bodily transport of longitudinal magnetic flux *out* of the simulation domain,  $\Phi_{\text{photo}}(t) + \Phi_{\text{conv}}(t) \leq \Phi_0$ , where  $\Phi_0$  is the initial longitudinal flux of the tube. The escaped flux is defined as  $\Phi_{\text{esc}}(t) := \Phi_0 - \Phi_{\text{photo}}(t) - \Phi_{\text{conv}}(t)$ , and is the amount of flux that has exited the domain. For all the cases discussed below and within the time interval considered ( $0 \leq t \leq 24$  min.), no magnetic flux ever reaches the bottom boundary. Thus,  $\Phi_{\text{esc}}$  effectively represents the amount of flux that emerges and passes above the photosphere to exit the domain.

Figure 4.6 shows  $\Phi_{\text{conv}}$ ,  $\Phi_{\text{photo}}$  and  $\Phi_{\text{esc}}$  as functions of time. The left panel shows the quantities for the emergence of the untwisted tube, the right panel for the emergence of the twisted tube ( $\lambda = 0.5$ ). The untwisted tube begins to enter the photosphere at  $t = 7$  min. In this case, the further rise of the magnetic structure into the photosphere continues only until  $t = 12$  min. After this time, the amount of flux above  $\tau_{\text{Ross}} = 1$  steadily decreases. This decrease indicates a submergence of flux that had previously

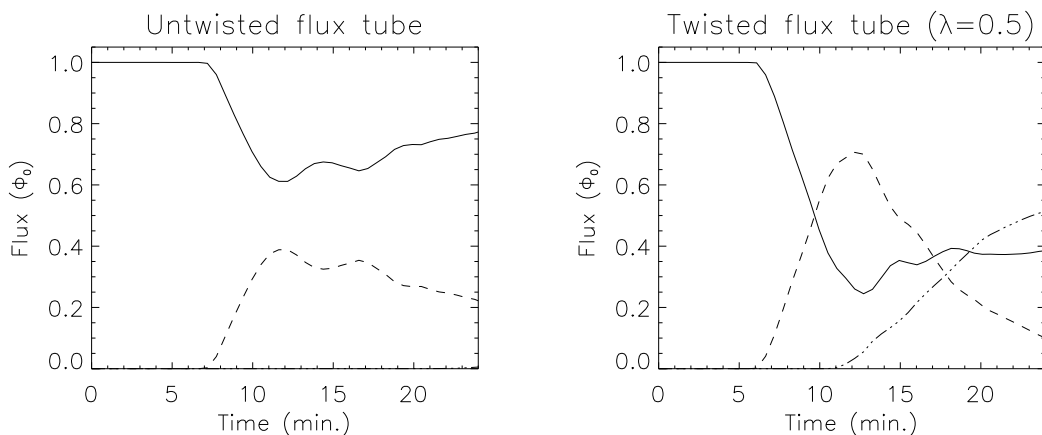


Figure 4.6: The two panels show  $\Phi_{\text{conv}}$  (the longitudinal flux below  $\tau_{\text{Ross}} = 1$  in the simulation domain; solid line),  $\Phi_{\text{photo}}$  (the longitudinal flux above  $\tau_{\text{Ross}} = 1$ ; dashed line) and  $\Phi_{\text{esc}}$  (the longitudinal flux that has left the simulation domain; dash-dotted line). All three quantities are shown in units of  $\Phi_0$ , the initial flux of the tube. The left panel is for the emergence of an untwisted flux tube, the right for a twisted flux tube with  $\lambda = 0.5$ . Comparison of the two cases shows that the rise of a twisted flux tube is much more efficient at transporting magnetic flux into and above the photosphere.

emerged. The dash-dotted line ( $\Phi_{\text{esc}}$ ) in the left panel is barely visible because almost all of the flux that emerges into the photosphere is either trapped there, or is recirculated back into the convection zone. Compare this scenario with that of an emerging, twisted flux tube. In the right panel of Fig. 4.6, we find that the fraction of flux in the photosphere increases between  $t = 7$  min and  $t = 12$  min. The maximum amount of the flux at any time residing in the photosphere is about  $0.7\Phi_0$ . Thereafter,  $\Phi_{\text{photo}}$  decreases steadily for two reasons. Firstly, part of the emerged flux is drawn into the developing downflows and is returned to the convection zone. This behaviour is similar to the case for an untwisted tube. Secondly, some of the emerged flux rises through the upper boundary of the domain and escapes. This is indicated by the increase in  $\Phi_{\text{esc}}$  after  $t = 11$  min. At  $t = 24$  min, about 50% of the initial longitudinal flux of the tube has escaped the domain through the upper boundary.

The previous comparison suggests that the higher the level of twist in the initial flux tube, the larger the fraction of flux that can emerge at the visible surface. We have carried out additional simulation runs at intermediate levels of twist (between  $\lambda = 0$  and  $\lambda = 0.5$ ) to see whether there is a systematic trend. Since, at any time, the emerged flux can be residing either in the photosphere or above the top domain boundary, the appropriate quantity for comparison between the runs is the maximum of  $\Phi_{\text{photo}} + \Phi_{\text{esc}} = 1 - \Phi_{\text{conv}}$  over the time interval of the emergence event ( $0 \leq t \leq 24$  min). Fig. 4.7 shows this quantity as a function of the initial twist of the flux tube. Clearly, the maximum fraction of flux above the visible surface is an increasing function of  $\lambda$ . What is the physics behind this trend? Firstly, we point out that the twist of magnetic field lines counter-acts the splitting of the tube into a pair of vortex rolls. A more twisted, and consequently more coherent tube, maintains a greater amount of buoyancy. Thus a twisted tube, upon emergence at the surface, is able to overshoot further into the photosphere than

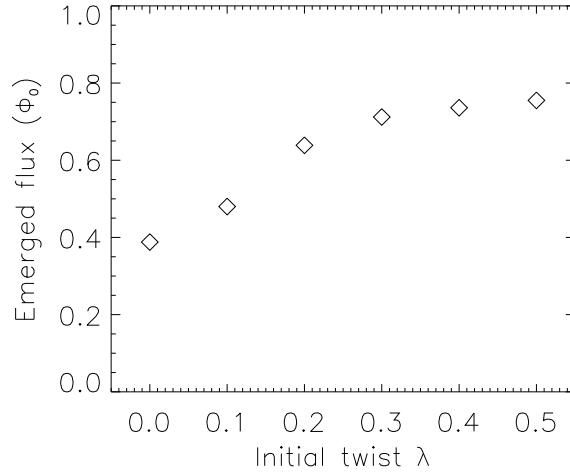


Figure 4.7: The maximum fraction of longitudinal magnetic flux above the visible surface ( $\tau_{\text{Ross}} = 1$ ) as a function of the initial twist of the flux tube.

an untwisted tube.

The suppression of vertical motions by the stably stratified photosphere may be insufficient to halt the further rise of the magnetic field. Consider a subadiabatically stratified, hydrostatic layer in the absence of magnetic fields. Gravity acts to counteract perturbations in the vertical velocity. Now imagine that we introduce a horizontal magnetic structure of finite thickness such that the layer remains static and mechanical equilibrium is maintained. This requires a reduction of the internal density of the magnetic layer, creating a top-heavy configuration at the interface between the top of the magnetic layer and the original stratification.

Using the linear stability analysis of Acheson (1979, originally carried out for the flux sheet configuration mentioned above), Archontis et al. (2004) have pointed that, given a sufficiently strong field, a magnetic buoyancy instability can develop from perturbations of the vertical velocity despite a subadiabatic stratification. Furthermore, they pointed out that perturbations which bend the field lines are more destabilizing than perturbations which do not. The reason is that in the former case, mass in the crests of the perturbed magnetic structure can drain down along the field lines, effectively enhancing the buoyancy of the rising parts of the magnetic structure. In the context of these two points, they explained why a high magnetic field strength and the presence of a transverse component of the field (i.e. twist) aid the rise of a magnetic flux tube beyond the photosphere in their 3D simulations. Previous 2D flux emergence simulations by Shibata et al. (1989) and by Magara (2001) have also identified magnetic buoyancy instabilities as mechanisms that allow magnetic structures to emerge past the photosphere into the chromospheric and coronal layers.

# 5 Photospheric flux emergence: 3-dimensional simulations

In Chapter 4, we presented a study of photospheric flux emergence using 2D simulations. In that study, we considered the effects of radiative transfer on an emerging flux tube, but neglected the effects of convection. In this chapter, we extend our study by carrying out 3D numerical simulations including the effects of convection. Having included all the relevant physics, we are in a position to compare our simulation results with observations of flux emergence.

## 5.1 Simulation setup

### 5.1.1 Boundary conditions

Periodic boundary conditions are imposed on the vertical boundaries. The boundary conditions of the upper and lower boundaries used in these simulations here are identical to the one used for the 2D study. We refer the reader to Section 4.1.1 for details.

### 5.1.2 Initial conditions

In Chapter 3, we discussed the properties of the photosphere and the underlying near-surface convection in the absence of magnetic fields. For the present study, we have carried out a number of simulation runs, each modelling the emergence of an individual flux tube. To prepare the initial configuration for each simulation run, a snapshot from the purely hydrodynamic simulation was chosen as the background atmosphere. Recall that the domain has dimensions  $24 \times 12 \times 2.3 \text{ Mm}^3$ . In all subsequent discussion,  $t = 0$  refers to the moment when a flux tube is introduced into the sub-surface layers. The axis of the tube is located at  $[y, z] = [6, -1.35] \text{ Mm}$ . The longitudinal and transverse components of the magnetic field have the form given by Eqs. (4.7) and (4.8).

In principle, one would prefer to introduce the flux tube into the domain in such a way that the disturbance added to the system is minimized. The most appropriate way to do this is to introduce the tube, so that the distribution of divergence of the total stress tensor (Maxwell + pressure + viscous) remains unchanged. For this reason, the original gas pressure in the volume occupied by the tube is decreased. The modification of the gas pressure distribution is necessary in order to balance the Lorentz and pressure gradient forces. If, in addition, we keep the original velocity distribution in the field-free domain, we would satisfy the aforementioned criterion. We prefer, however, to begin a simulation

Label	$B_0$ (G)	$R_0$ (km)	$\lambda$	$\Phi_0$ ( $10^{19}$ Mx)	Entropy distribution
U1	8500	200	0.5	1	Uniform
U2	8500	200	0.25	1	Uniform
U3	8500	200	0	1	Uniform
U4	5250	200	0.5	0.66	Uniform
U5	2500	200	0.5	0.31	Uniform
L1	8500	200	0.5	1	Loop

Table 5.1: Initial properties of the individual magnetic flux tubes in each of the simulation runs. The label of each run is given in the leftmost column. Entries in the remaining columns indicate the magnitude of the longitudinal field at the tube axis ( $B_0$ ), the characteristic tube radius  $R_0$ , the twist parameter  $\lambda$ , the total longitudinal flux  $\Phi_0$ , and the initial specific entropy distribution.

with a flux tube that has its own initial identity. As a compromise between these two considerations, we use a tapering function to specify the initial velocity distribution. Let  $\mathbf{v}_{\text{orig}}$  be the original velocity distribution in the non-magnetic domain. The initial velocity distribution within the flux tube is such that,  $\mathbf{v}_{\text{tube}}(r) = (1 - e^{-r^2/R_0^2})\mathbf{v}_{\text{orig}}$ , where  $r$  is the radial distance from the tube axis and  $R_0$  the characteristic radius of the flux tube at  $t = 0$ . This tapering function makes the fluid on the tube axis stationary. With increasing radial distance from the axis, the fluid velocity approaches the original velocity distribution of the external convecting flow.

Following the simulation setup of the 2D study, we choose to specify the initial specific entropy distribution in the tube. Table 5.1 gives the values of the initial parameters in each of the simulations. In runs U1 to U5, the flux tube has a uniform initial specific entropy distribution. Throughout the tube, the value of the specific entropy is  $s_{\text{up}} = 6.0R^*$ , which is the average value of upflowing regions at the initial depth of the tube ( $z = -1.35$  Mm). This initial configuration is essentially the same as the one used for the 2D study. In simulation L1, the initial specific entropy distribution is chosen, in such a way that the initially horizontal flux tube develops into an  $\Omega$ -type loop. For details about the initial configuration of this last simulation run, see Section 5.4. The insight we gained from the 2D study facilitates us to analyze the 3D results and pick out features that are common to both studies. It also helps us to isolate effects in the 3D simulations that are due to convection and to variations in the third direction.

## 5.2 Influence of convection on flux emergence

Convection plays a key role in determining the properties of emerging flux. As discussed in Section 3.3.1, near-surface convection in the Sun consists of disjointed upwellings separated by a network of downflow lanes and vertices. An initially horizontally flux tube embedded in this setting will encounter both upflows and downflows. Whereas the upwellings aid the emergence of some segments of the tube, the downflows impede the rise of other segments. Given such an initial configuration, under what circumstances can we expect the tube to emerge intact without severe distortion by the downflows? In other words, what does it mean to have a ‘strong’ flux tube?



There are a number of comparisons we can make. First of all, let us compare the magnetic energy density of the tube with the kinetic energy density of the external flow. Given a characteristic fluid density  $\rho$  and a characteristic speed  $v$ , we define the *equipartition field strength*  $B_{\text{eq}}$  such that the magnetic energy density is equal to the kinetic energy density,

$$\frac{B_{\text{eq}}^2}{8\pi} = \frac{1}{2}\rho v^2. \quad (5.1)$$

From considerations of the energetics alone, we expect that in order for the magnetic field to evolve passively with the flow, the field strength within the tube must satisfy  $B_0 \ll B_{\text{eq}}$ . On the other hand, for the magnetic field to have the capacity to partially control the dynamics, the magnetic field strength  $B_0$  should satisfy

$$B \gtrsim B_{\text{eq}}. \quad (5.2)$$

A statement equivalent to (5.2) is that we require the Alfvén speed,  $v_A = B_0(4\pi\rho)^{-1/2}$ , to be larger than the characteristic fluid speed.

Consideration of the force balance on the tube allows us to determine a similar criterion (Fan et al. 2003). For the following analysis, let us suppose that the flux tube has uniform magnetic field strength,  $B_0$ , and uniform density deficit,  $\Delta\rho$ , with respect to the surroundings. Consider a cross-section of the flux tube that happens to be in the way of a downflow. Under a number of simplifying assumptions (see Section 2.4.2), the drag force experienced by the flux tube is given by:

$$F_{\text{drag}} = -\frac{C_D \rho v^2}{\pi R_0}, \quad (5.3)$$

where  $R_0$  is the radius of the tube and  $v$  the characteristic velocity of the downflow.  $C_D$  is the drag coefficient and has a magnitude of order unity for  $Re \gtrsim 50$ . The buoyancy force experienced by the tube is directed upwards and is given by

$$F_{\text{buoyancy}} = g\Delta\rho. \quad (5.4)$$

Using the relation that  $\Delta\rho/\rho \simeq \Delta p/p\gamma_1 = (\gamma_1\beta)^{-1}$ , we can express the density deficit in the tube as a function of the internal field strength. In order for the flux tube to accelerate upwards, the buoyancy force must overcome the drag force. For this to happen, the magnetic field strength in the tube must satisfy

$$B_0 \gtrsim \left(\frac{2C_D\gamma_1}{\pi}\right)^{1/2} \left(\frac{H_p}{R_0}\right)^{1/2} B_{\text{eq}}, \quad (5.5)$$

$$\lesssim \left(\frac{H_p}{R_0}\right)^{1/2} B_{\text{eq}}, \quad (5.6)$$

where  $H_p$  is the pressure scale height of the background. The factor  $2C_D\gamma_1/\pi$  is of order unity, which allows us to go from expression (5.5) to (5.6). This criterion is similar to (5.2) but is more stringent because it takes into account the radius of the tube. The radius is important because, given the same field strength, a flux tube with a larger radius has more buoyancy than a smaller tube. We should restrict our attention to cases where

$R_0 < H_p$  when using (5.6) for the reason that when  $R \gtrsim H_p$ , the drag force is no longer given by (5.3). What we learn from criterion (5.6) is that in order for the flux tube to rise against downflows, it is not enough for the flux tube to have an equipartition field strength. If the tube has a radius  $R_0 = 0.25H_p$ , then it must have a field strength of at least  $2B_{\text{eq}}$  in order to have sufficient buoyancy to rise against the drag of downflows. We should emphasize here that the foregoing derivation serves to provide estimates of the magnitudes of the different forces acting on a tube. Strictly speaking, the speed of the flow past the cylinder should have small Mach numbers for Eq. (5.3) to be valid. This assumption is violated by the strong downflows just beneath the solar surface. Despite this limitation, the simulation we will present in the following indicate that criterion (5.6) is indeed useful for understanding the qualitative behaviour of flux tubes in our simulations.

Fan et al. (2003) have studied the interaction of flux tubes with convection by means of 3D MHD simulations. They found that flux tubes with sub-equipartition fields strengths do indeed evolve passively with the convective flow. Even for flux tubes with a central field strength  $B_0 = B_{\text{eq}}$ , the evolution of the flux tube depends on the local conditions of segments of the tube. Segments of the tube aligned with upflows rise, whereas segments in the way of downflows are pinned down to the bottom boundary. As they increased the field strength beyond the value  $(H_p/R_0)^{1/2}B_{\text{eq}}$ , they found that the evolution of the flux tube approached the behaviour of flux tubes rising in static atmospheres.

The simulation results of the present study support the findings of Fan et al. (2003). Although our simulations also model the interaction of a horizontal magnetic flux tube with convection, there is an important difference. Our simulations were performed by solving the fully-compressible MHD equations whereas Fan et al. (2003) performed theirs under the *anelastic* approximation. This approximation is valid only for a flow with speeds much less than the sound speed, which means it is not suitable for simulating near-surface convection. For their study, they were able to introduce flux tubes with fields strengths up to 10 times the equipartition value because the speed of the downdrafts in their convecting layer were strongly subsonic. In contrast, the Mach number in the near-surface layers of the convection zone reach  $M \sim O(0.1) - O(1)$ . If we were to introduce a flux tube with a field strength many times  $B_{\text{eq}}$  for these strong flows, the total pressure within the tube would also be many times the external gas pressure. Such an initial condition is likely to be unphysical. Therefore, we are restricted to initial field strengths lower than, or comparable to  $B_{\text{eq}}$ . The value of the equipartition field strength is different for different depths. At the original depth of the flux tube ( $z = -1.35$  Mm), the ambient density is  $\rho = 4.2 \times 10^{-6}$  g cm $^{-3}$ . The typical vertical velocity of downflowing material at this depth is 4 – 8 km s $^{-1}$ . For this range of velocities, the corresponding range of equipartition field strengths is  $B_{\text{eq}} = 2900 - 5800$  G. Taking the typical values at the surface ( $\rho = 2.6 \times 10^{-7}$  g cm $^{-3}$ ,  $v = 2 - 4$  km s $^{-1}$ ), the equipartition field strength there is  $B_{\text{eq}} = 450 - 700$  G.

We now proceed to discuss our own simulation results. First we focus our attention on run U5. In this run, the initial field strength at the tube axis is  $B_0 = 2500$  G. The corresponding plasma- $\beta$  at the tube axis has a value of 22. The magnetic flux a cross-section of the tube is  $3.1 \times 10^{18}$  Mx. The tube is initially twisted ( $\lambda = 0.5$ ). The tube has an initial characteristic radius of  $R_0 = 200$  km  $\approx 0.4H_p$ . Criterion (5.6) tells us that the tube must have at least a field strength of  $(H_p/R_0)^{1/2}B_{\text{eq}} = 4600 - 9200$  G in order to rise against the downflows. Since the tube has only a central field strength of  $B_0 = 2500$  G

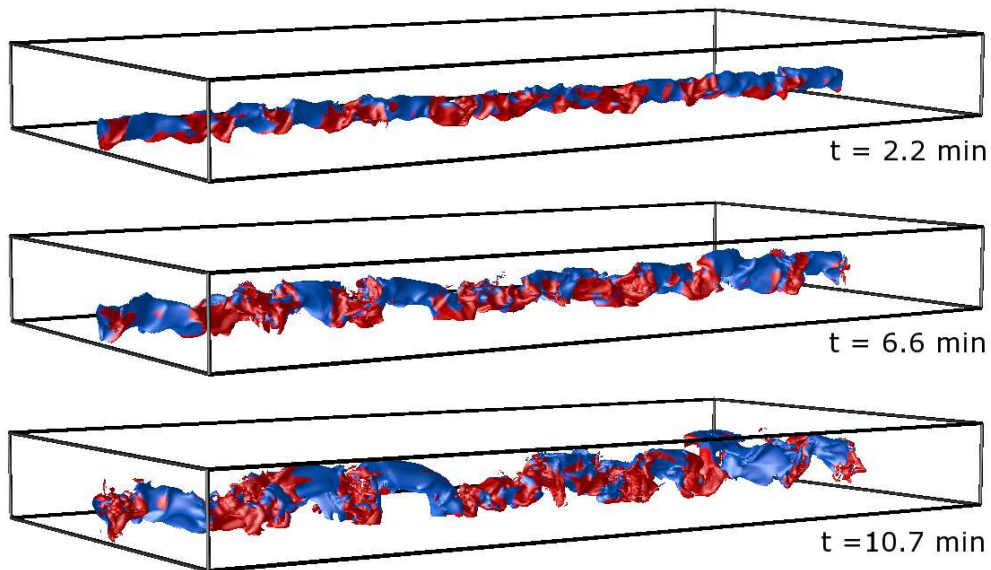


Figure 5.1: The passive evolution of a weak magnetic flux tube (run U5,  $B_0 = 2500$  G) with the convective flow. Shown above is a sequence of isosurfaces of  $|B| = 400$  G. On each isosurface, the blue (red) colour-coding indicates upflows (downflows). Segments of the tube co-incident with upflows are able to rise and emerge, whereas segments aligned with downflows are kept submerged.

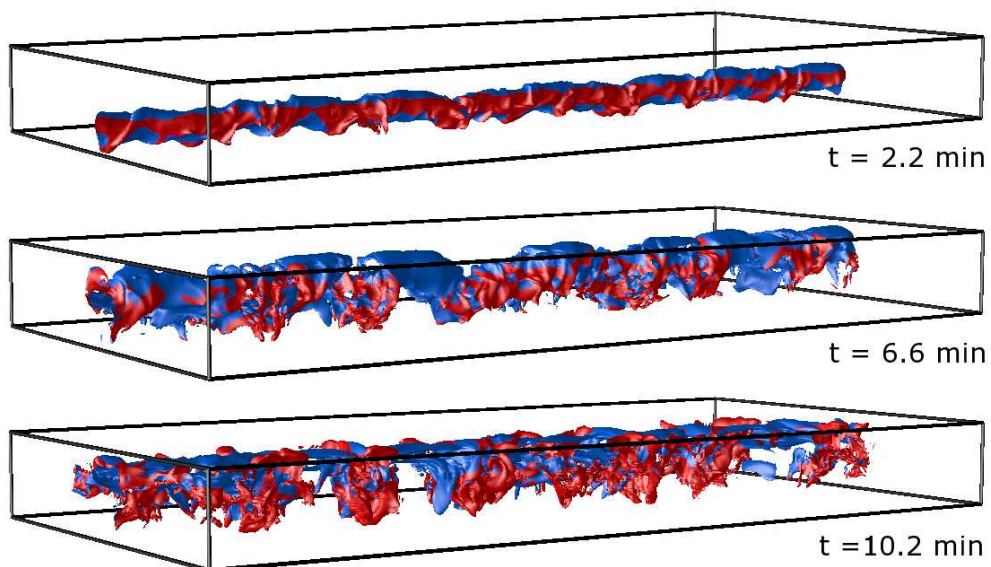


Figure 5.2: Same as Fig. 5.1 but for a flux tube with higher initial field strength (run U1,  $B_0 = 8500$  G). The isosurfaces here correspond to  $|B| = 700$  G. In this case, the convective flows do not completely control the dynamics of the flux tube.

(the average field strength over its cross-section is even smaller), we expect the evolution of the flux tube to be dominated by the convective flows. This is indeed what we find. Fig. 5.1 shows a time sequence of 3D isosurfaces of  $|B| = 400$  G. In all three panels, the blue (red) colour-coding indicates that the vertical velocity at the isosurface is upwards (downwards). Near the beginning of the simulation ( $t = 2.2$  min), we already find that the flux tube has been distorted by the convective flows. In subsequent snapshots, we find that the upflows have advected segments of the tube upwards, whereas the downflows have pinned down other segments below the surface. The shape of the flux tube resembles a *sea serpent*.

Figure 5.3 gives another illustration of how the flux tube in run U5 evolves passively with the convecting flow. The figure shows a sequence of snapshots of a cross-section of the simulation domain at  $x = 12$  Mm. The grey scale indicates the temperature distribution and the colour-coding indicates the absolute field strength  $|B|$ . The arrows indicate the components of the velocity field in the  $y-z$  plane at  $x = 12$  Mm. The purple line running near  $z = 0$  indicates the level of optical depth unity in the continuum at a wavelength of  $5000 \text{ \AA}$  ( $\tau_{5000} = 1$ ). At  $t = 0$  min, this particular segment of the tube is aligned with a downflow. In the following snapshot at  $t = 4.4$  min, we find that this segment of the tube has been displaced downwards. In the final two snapshots ( $t = 8.8$  min and  $t = 12.4$  min), we witness the tube segment being severely deformed by the shear in the velocity field at the interface between upflows and downflows. While the central part of the tube segment is pushed downwards, other parts of the tube segment are carried upwards.

We have carried out other simulation runs with higher initial field strengths. As expected, the ability of the convective flows to dominate the evolution of the tube lessens with increasing initial field strength. In run U1, the initial field strength on the axis of the tube is  $B_0 = 8500$  G, which is within the range of  $B_{\text{eq}}$  for the original depth of the tube and corresponds to a plasma- $\beta$  approximately equal to unity. The total longitudinal magnetic flux carried by the tube is  $10^{19}$  Mx. Fig. 5.2 shows a time sequence of isosurfaces of  $|B| = 700$  G for this run. Again, the colour-coding indicates upwards or downwards vertical velocity. In this case, the flux tube is not so weak, that it is simply advected by the convective flow. Nor is it sufficiently strong, that it rises as if it were embedded in an initially static medium. The behaviour of the tube is in an intermediate regime between these two extremes. On the one hand, the convective flow is able to deform the tube. On the other hand, the bulk of the tube finally does overcome the impeding downflows to emerge at the surface.

Fig. 5.4 helps emphasize the previous point. At  $t = 0$  min, the tube segment shown is aligned with a downflow. In run U5, this downflow advects the tube downwards. The situation in run U1 is very different. While the downflow is able to divert the tube slightly towards the right, it is unable to keep the tube beneath the surface. Instead, the tube is sufficiently buoyant that it overcomes the downflow and emerges. During emergence, the expansion of the tube drives two supersonic, horizontal outflows to the left and right sides of the emergence site. The expansion of the tube is strong enough, that shock fronts develop. We have already seen this behaviour in our 2D simulations of the emergence of flux tubes in an initially static atmosphere (see Section 4.2.1). In that case, the outflows to the left and to the right were exactly symmetric because the background atmosphere was initially plane-parallel. This symmetry is not found in the present case because the flux tube's rise is no longer purely vertical.

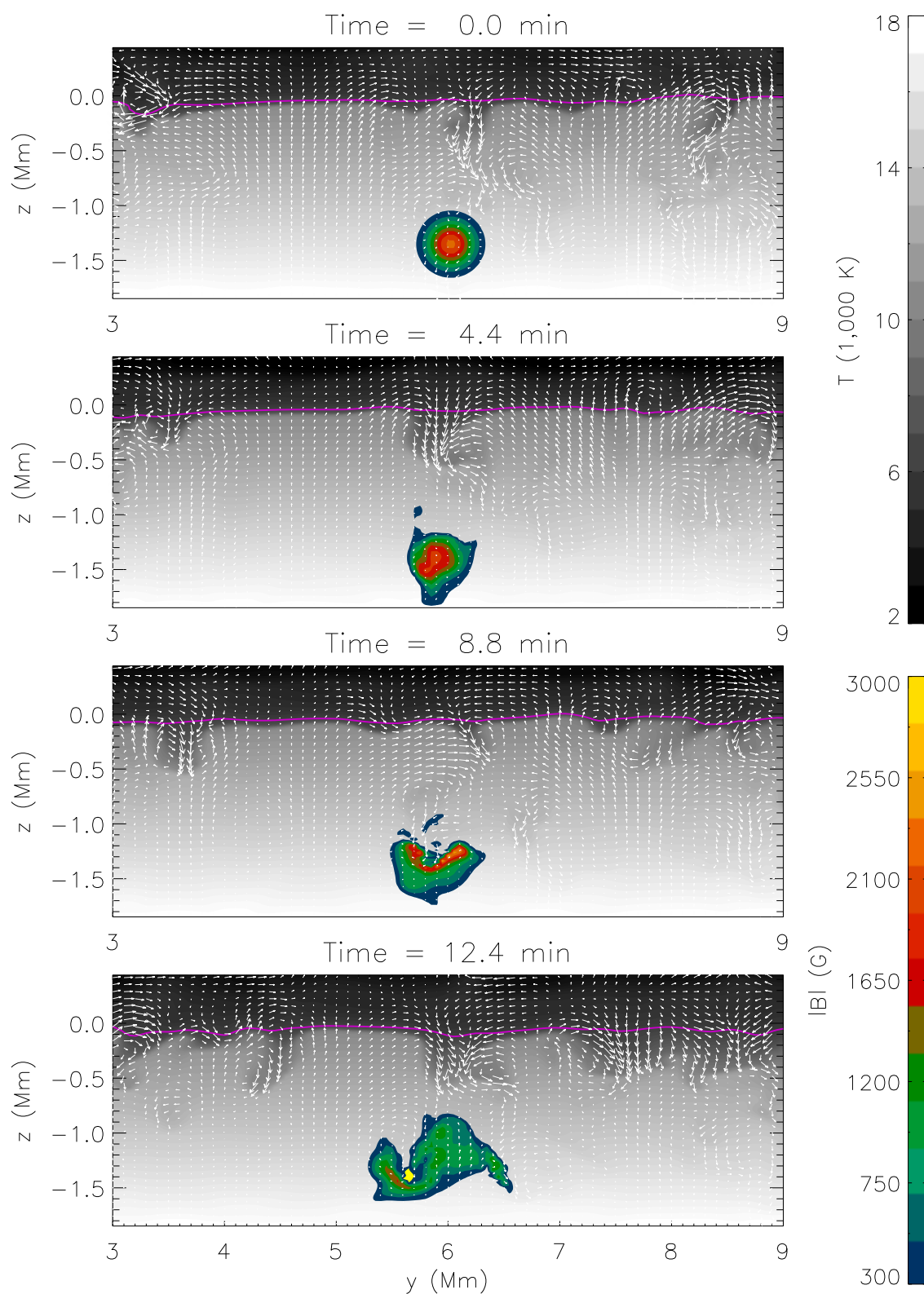


Figure 5.3: Time sequence of a cross-section of the simulation domain at  $x = 12$  Mm for run U5. The tube segment is passively advected by the convecting flow. The grey scale indicates the temperature distribution and the color-coding indicates the absolute field strength  $|B|$  distribution. The arrows show the components of the velocity field in the  $y - z$  plane at  $x = 12$  Mm. The purple line shows the  $\tau_{5000} = 1$  level.



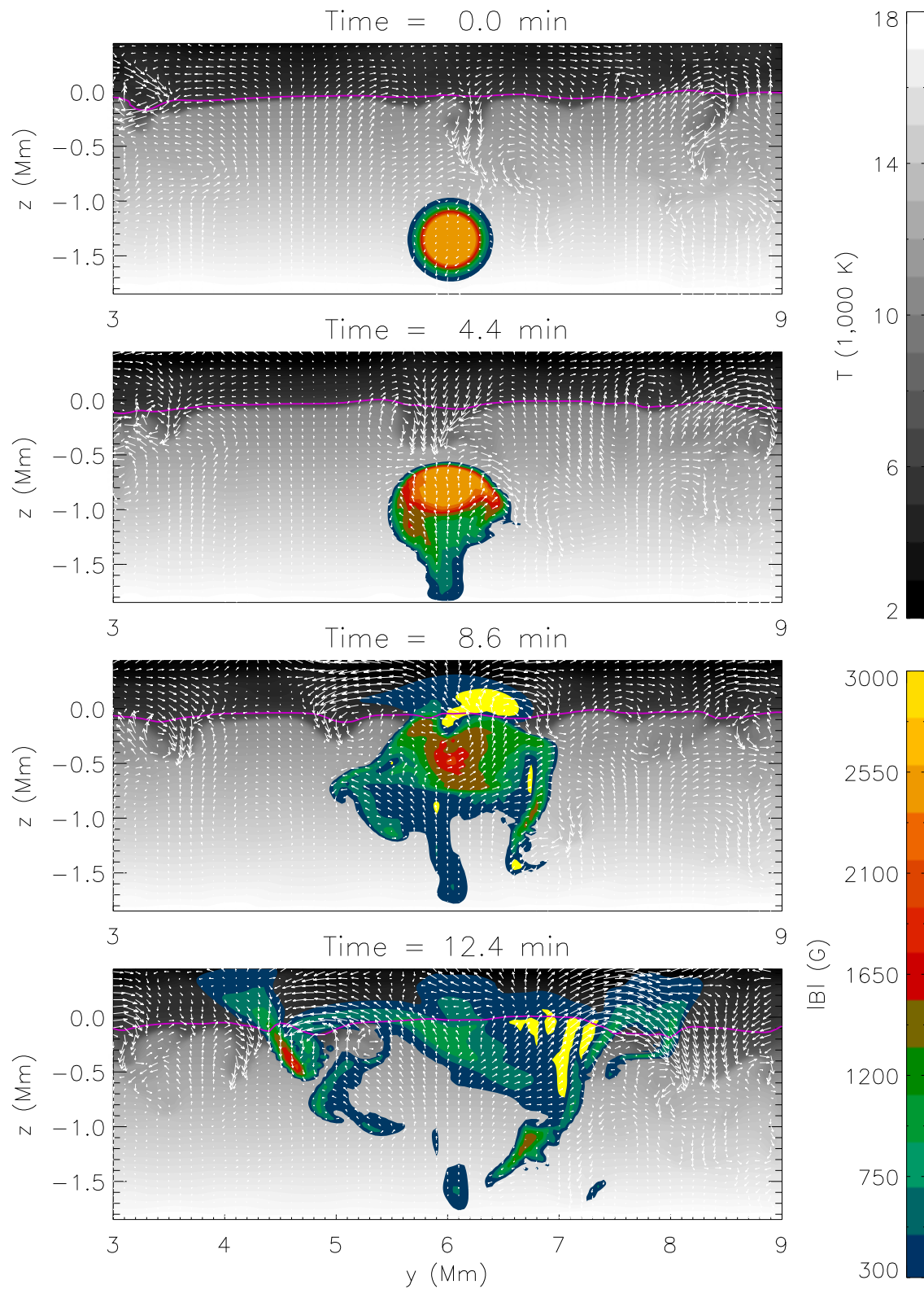


Figure 5.4: Same as Fig. 5.3 except for run U1, with  $B_0 = 8500$  G. In this run, the flux tube is sufficiently buoyant and the magnetic field sufficiently strong to rise against the drag of the downflow (see snapshot at  $t = 0$  min). The expansion of the rising magnetic complex drives horizontal flows away from the emergence site.

## 5.3 Observational signatures

In the following sections, we compare the simulation results with observations of flux emergence.

### 5.3.1 Quiescent flux emergence

The tube in run U5 evolves passively with the convective flow. Consequently, the emergence of magnetic flux does not lead to a severe disturbance in the appearance of the granulation in white light intensity images. For this reason, we refer to these flux emergence events as *quiescent*.

Figure 5.5 shows the emergence event in U5. In the left column, the grey scale indicates  $I_{5000}$ , the emergent continuum intensity at a wavelength of  $5000 \text{ \AA}$  calculated for vertical lines-of-sight ( $\mu = 1$ ). The overlaid arrows indicate the horizontal components of the surface velocity field at  $\tau_{5000} = 0.1$ . A vector with a length of one grid-spacing in the vector plot corresponds to a speed of  $4 \text{ km s}^{-1}$ . The right column shows the corresponding time sequence of *synthetic vector magnetograms*. Strictly speaking, a proper comparison between the simulation results with the observations would require us to first synthesize Stokes profiles using the simulation data, and then invert these synthetic profiles to retrieve the physical properties of the atmosphere. While this is certainly an interesting exercise, it is beyond the scope of this dissertation. Instead, we produce our synthetic magnetograms (and also synthetic Dopplergrams) by evaluating the values of the magnetic field at an optical depth of  $\tau_{5000} = 0.1$  for vertical lines-of-sight. The reason for choosing this optical depth is the following: The maxima of the contribution functions of many photospheric lines commonly used to probe surface magnetic fields (e.g. Fe I 6301, Fe I 6302) is located close to this optical depth. As such, we can expect that the information carried by the line to be representative of the physical quantities in this layer of the atmosphere.

In all eight panels of Fig. 5.5, the overlaid contours indicate the vertical component of the magnetic field ( $B_z$ ) at the levels  $\pm[50, 100, 200, 400] \text{ G}$ . Green and red contours correspond to positive and negative polarities respectively. The grey scale in panels in the left column indicates the absolute field strength  $|B|$  and the overlaid arrows in this column indicate the horizontal components of the magnetic field. A vector with a length of one grid-spacing in the vector plot corresponds to a magnitude of  $250 \text{ G}$ .

The flux tube is initially aligned in the  $x$ -direction along  $y = 6 \text{ Mm}$ . At  $t = 12.4 \text{ min}$ , we see the first signs of flux emergence into the photosphere. In this simulation run, the magnetic field always emerges within the interior of granules. In a granule where flux emerges, the magnetic field near the granular centre is predominantly horizontal. Towards the edge of the granule, the magnetic field becomes more vertical. This is in accordance with the fact the magnetic field threading a granule is forced to emerge in an arched configuration. One example of the above is the bipolar region emerging in the granule centered at  $[x, y] = [4, 7] \text{ Mm}$  (see snapshot at  $t = 12.4 \text{ min}$ ). At this particular instant, the flux contained in each polarity of this small-scale bipolar is  $8 \times 10^{17} \text{ Mx}$ . The flux contained in this small-scale bipole is at least an order of magnitude smaller than the flux contained in small ephemeral regions.

The vector plots of the horizontal velocity field in the left column of Fig. 5.5 show

that the granules are sites of horizontally diverging flow. The diverging flow has the effect of expelling the emerged flux to the intergranular network. This *flux expulsion* process is efficient and occurs on the granulation timescale, which is on the order of 5 min (see Chapter 3). At  $t = 17.7$  min (about 5 minutes after the first snapshot), the distribution of  $|B|$  and  $B_z$  show that the regions of strongest field are in the intergranular lanes. In comparison, the granule interiors have significantly weaker fields. The next snapshot at  $t = 22.1$  min also shows that the strongest fields are located in the intergranular lanes. Within the time interval already discussed, the surface field strength at  $\tau_{5000} = 0.1$  rarely exceeds the equipartition value of 450 G.

Weiss (1966) was the first to demonstrate the behaviour of flux expulsion from fluid eddies by carrying out 2D simulations in the kinematic regime (i.e. neglecting the back reaction of the magnetic field on the flow). More recent numerical simulations of self-consistent magneto-convection in 2D (Proctor and Weiss 1982, Hurlburt and Toomre 1988) and in 3D (Cattaneo et al. 2003) have demonstrated that flux expulsion is indeed a robust feature of magneto-convection. Typically, these simulations begin with a uniform vertical magnetic field embedded in initially convecting, stratified layer. The stratification may be idealized (such as that of a polytrope) or may be close to that of the near-surface layers (Bercik et al. 2003, Vögler et al. 2005). The latter authors have used the MURaM code to carry out magneto-convection simulations of the near-surface convection zone/photospheric layers. Their simulation setup is very similar to the one we use for the flux emergence simulations in this study. The one crucial difference is in the choice of initial conditions. In their magneto-convection simulations, Vögler et al. imposed a uniform distribution of purely vertical magnetic field of one polarity. Thus their initial condition has a net signed flux crossing the visible surface. Our initial condition involves a initially submerged magnetic structure with a predominantly horizontal field. The initial total vertical flux crossing any horizontal surface is zero. They also found flux expulsion to be an important feature of their simulations. Given that the magnetic field is not so strong that it suppresses convective motion, most of the vertical flux is expelled into the intergranular network within a few granulation timescales.

How do our simulation results compare with observations? Using the Swedish Vacuum Tower Telescope, De Pontieu (2002) has been able to obtain high cadence and high resolution observations of an emerging flux region (EFR). From a 3.5 hr time series of this EFR, he identified seven individual small-scale emergence events. His two key findings relevant for this discussion are: **(a)** that magnetic concentrations emerge in the interior of granules; and **(b)** that within 10 – 15 min of initial appearance, the flux concentrations are quickly dispersed by the granular flow. He estimates the average flux density of the emerging magnetic concentrations to be about  $200 \pm 30$  Mx  $\text{cm}^{-1}$ . If one were to interpret his estimate of the flux densities as an estimate of the actual magnetic field strength, one comes to the conclusion that the emerging fields have sub-equipartition strength ( $B_{\text{eq}} \approx 450$  G), a finding that is consistent with **(a)** and **(b)**. De Pontieu also gives estimates for the average flux of the emerging concentrations, which turn out to be  $(9 \pm 4) \times 10^{17}$  Mx. This is the same order of magnitude as what we find for individual polarities of emerging flux concentrations in run U5.

De Pontieu suggested that the small-scale emergence events he detects may be related to the so-called horizontal internetwork fields (HIFs, Lites et al. 1996). According to Lites et al., HIFs are *predominantly horizontal* magnetic structures with length and time scales



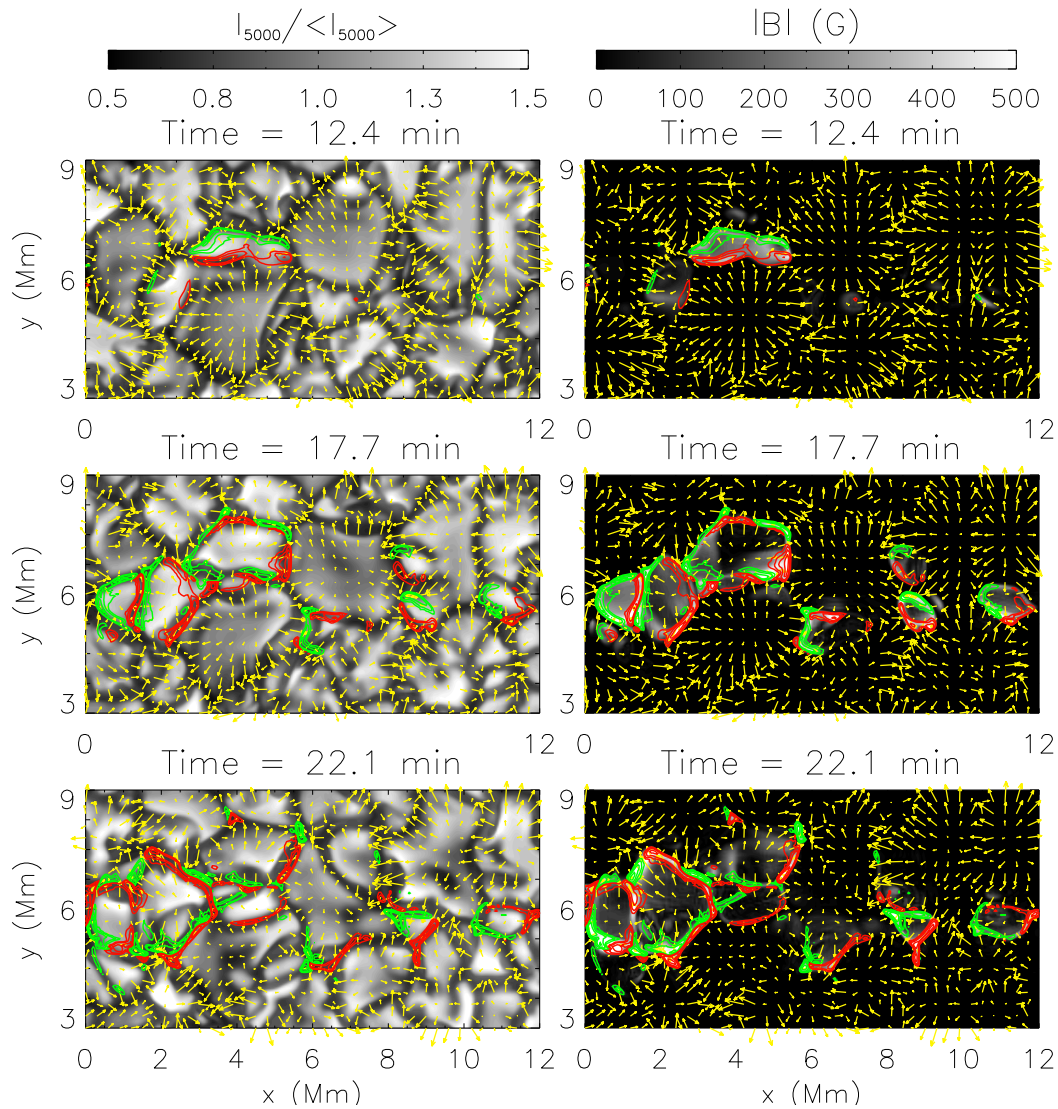


Figure 5.5: Emergence of magnetic field into the photosphere in run U5. The left column shows a time sequence of the emergent continuum intensity  $I_{5000}$ . The vector overlays in the left column indicate the horizontal components of the velocity field at  $\tau_{5000} = 0.1$ . The right column shows the corresponding time sequence of synthetic vector magnetograms. The grey scale indicates the absolute field strength  $|B|$  and the vector overlays indicate the horizontal components of the magnetic field, both taken at  $\tau_{5000} = 0.1$ . In both columns, the contour overlays indicate the distribution of the vertical component of the magnetic field at  $\tau_{5000} = 0.1$ . Green (red) contours indicate magnetic field directed out of (into) the visible surface.

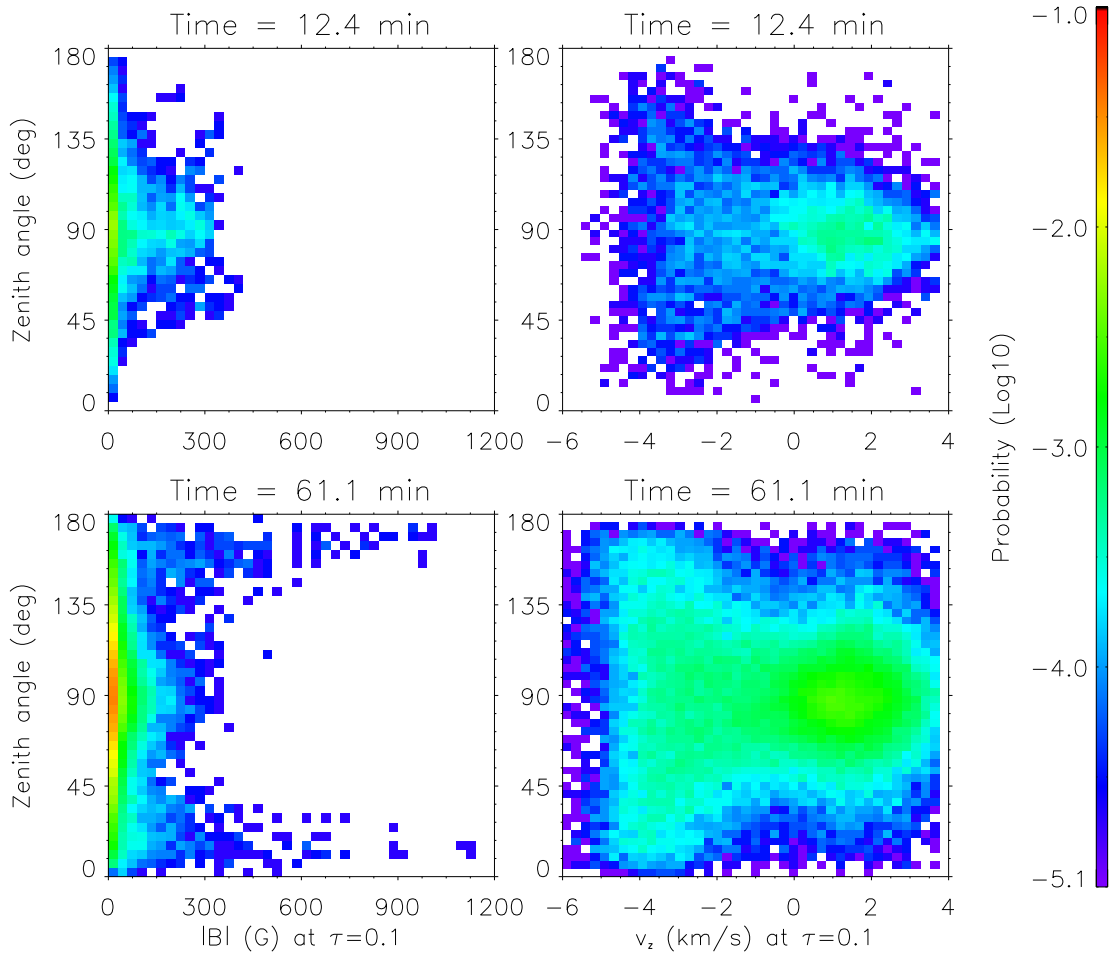


Figure 5.6: *Left column*: Joint probability distribution functions (JPDFs) of the zenith angle of the magnetic field vector against the absolute field strength  $|B|$ . Both quantities have been evaluated for the  $\tau_{5000} = 0.1$  level. *Right column*: JPDF between the zenith angle and the vertical fluid velocity. The colour coding indicates the logarithm of the probability. The upper and lower rows respectively show the JPDFs at  $t = 12.4$  min and  $t = 61.1$  min for run U5.

of  $1 - 2''$  and 5 min respectively. The existence of HIFs are inferred from the distinctive signals in the Stokes Q and U profiles of relatively quiet regions of the solar surface. The strength of these signals indicate that HIFs are generally weak with  $|B| \lesssim 600$  G. HIFs are usually detected in regions where the spectral lines are slightly blueshifted, indicating the association with HIFs with upflows. Both Lites et al. and De Pontieu interpret these as signatures of the crests of magnetic loops emerging through granules.

We have analyzed simulation run U5 to check whether this interpretation is tenable. Fig. 5.6 shows joint probability distribution functions (JPDFs) between different surface quantities in the simulation run for times  $t = 12.4$  min (upper row) and  $t = 61.1$  min (lower row). The left column shows JPDFs between the *zenith angle*  $\gamma$  of the magnetic field against the absolute field strength  $|B|$ , both evaluated at  $\tau_{5000} = 0.1$ . The zenith

angle is defined as the angle between  $\mathbf{B}$  and the  $z$ -axis. As such, magnetic field vectors with  $\gamma = 0^\circ$  and  $\gamma = 180^\circ$  correspond to purely vertical magnetic field that points out of and into the plane respectively. Purely horizontal fields have  $\gamma = 90^\circ$ . The right column shows JPDFs between the zenith angle and  $|B|$ . The left column shows JPDFs between zenith angle and the vertical fluid velocity (for surface regions with  $|B| > 0$ ). Recall from Fig. 5.5 that flux begins to emerge approximately at  $t = 12.4$  min. The JPDFs at this time indicate the existence of predominantly horizontal field with strengths of up to  $|B| \approx 400$  G. These horizontal fields mainly have rise velocities of  $1 - 2 \text{ km s}^{-1}$ , which is typical of granular upflows. This finding is compatible with the scenario proposed by Lites et al. and by De Pontieu (2002) for the explanation of HIFs.

Now, let us proceed to study the JPDFs at a much later time of  $t = 61.1$  min. We find a distinctly different shape for the JPDF between the zenith angle and  $|B|$ . There exists a pair of horn-like features that indicate the existence of some strong vertical fields of up to 1 kG. We will return to this point in the following section. For the moment, we are interested in the existence of horizontal fields. Indeed, we find at this time that there is a continuous distribution of nearly horizontal fields with strengths of up to 300 G. The accompanying JPDF between the zenith angle and  $v_z$  indicates that the majority of horizontal fields reside within upflow regions (granules). In fact, the JPDF between the zenith angle and  $|B|$  at  $t = 61.1$  min resembles those found by Vögler (2003), who studied magneto-convection in the near-surface layers with the MURaM code. In his simulations, the initial condition consisted of a uniformly vertical field instead of an initially submerged field. What this comparison tells us, is that the abundance of weak horizontal fields in granule interiors is a feature of the process of magneto-convection and not necessarily associated with emerging flux.

### 5.3.1.1 Surface evolution of emerged field: cancellation, coalescence and secondary emergence

In run U5, the morphology of the emerged field bears little resemblance to the initial horizontal flux tube structure. The arrangement of the surface field some minutes after initial flux emergence (see snapshots at  $t = 17.7$  and  $22.1$  min in Fig. 5.5) looks a bit like the *salt and pepper* pattern of quiet Sun magnetic fields observed by Domínguez Cerdeña et al. (2003). Our results and their observational results are similar in that we both have a mixture of positive and negative small-scale flux in the intergranular network. Their observations have a cadence of 50s, which enabled them to study the dynamic evolution of these small-scale flux concentrations. The time series of intensity images and magnetograms in Fig. 10 of their paper show the ability of the granular flow to disperse and to advect the existing flux concentrations horizontally. Furthermore, there are instances when flux concentrations of like polarities meet, and appear to coalesce (to within the resolution limit). In another instance, which they explicitly point out in the caption to Fig. 10, there appears to be a flux cancellation event due to the encounter of opposite polarities. In our simulation (run U5), we also find instances of both these types of events. In the following, we focus on one particular coalescence event between two flux concentrations.

Fig. 5.7 shows an example of such a coalescence event. At time  $t = 47.9$  min, we find a number of magnetic flux concentrations of both polarities. The most prominent

feature is centered at  $[x, y] = [2.5, 9]$  Mm. This feature resides at a downflow vertex between intergranular lanes and has a flux of  $1.5 \times 10^{18}$  Mx. The core of the feature has a maximum vertical field strength of  $B_z = 1,200$  G (at  $\tau_{5000} = 0.1$ ). A few minutes later, at  $t = 52.1$  min, we find a small bipolar pair emerging through a granule, which is located just to the right of the pre-existing flux concentration. The bipole is oriented such that the pole closest to the pre-existing flux concentration has the same polarity (positive). The horizontal velocity field at this time shows how the newly emerged flux is expelled to the intergranular network. When the newly emerged positive feature has been expelled, it encounters the pre-existing feature and the two coalesce into a larger flux concentration. The flux concentration resulting from the coalescence has a total flux of  $2.6 \times 10^{18}$  Mx, comparable to the longitudinal flux of the horizontal flux tube at the beginning of the simulation.

This particular example is interesting for a number of reasons. Firstly, the new bipole emerges at a relatively late stage of the calculation. The emergence of this bipole occurs many granulation times (40 min) after the initial appearance of flux at the surface (see Fig. 5.5). Its emergence location is also unusual. In Fig. 5.5, we see that almost all the flux emerges within a horizontal distance of 2 Mm away  $y = 6$  Mm (the original position of the tube axis at the beginning of the simulation). The new bipole, however, emerges significantly further away, at  $y \approx 9$  Mm. These two points are consistent with the fact that, when a section of a flux tube is passively carried by an upwelling, not all the flux contained in the tube emerges in one single event. The material near the edge of an upwelling may overturn before it reaches the surface. Consequently, the magnetic field threading this material fails to emerge on first attempt. This magnetic field may then continue to travel downwards, or may get caught up in another upwelling and travel upwards again. From this consideration, we can argue that although some magnetic field fails to emerge on first attempt, the convective flows *may* eventually bring it to the surface after some convective turnover times. The emergence of the bipole in Fig. 5.7 is one such example. The magnetic field associated with this bipole has overturned several times before it eventually reaches the  $\tau_{5000} = 0.1$  surface. Considering that it had been caught up in different upflows and downflows, it is not surprising that its emergence location is about 1 Mm further afield.

The coalescence event shown in Fig. 5.7 is interesting for another reason. We have already mentioned that the pre-existing positive flux concentration at  $t = 47.9$  min resides in a downflow vertex. This flux concentration is not as dark as the average intergranular lane or vertex. After coalescence, the resulting concentration appears even brighter. To explain this, we make reference to Fig. 5.8. Let us first look at the top row of this figure. The panels in this row show joint probability distribution functions (JPDFs) between the value of  $|B_z|$  at a horizontal plane of constant geometrical height  $\langle z_{0.1} \rangle$  and its value evaluated at optical depth  $\tau_{5000} = 0.1$  (for line-of-sights with  $\mu = 1$ ). The height  $\langle z_{0.1} \rangle$  corresponds to the average geometric height of the  $\tau_{5000} = 0.1$  surface in the absence of magnetic fields. On average, the  $\tau_{5000} = 0.1$  surface is higher than the  $\tau_{5000} = 1.0$  surface by about 160 km (i.e.  $\langle z_{0.1} \rangle - \langle z_{1.0} \rangle = 160$  km). We first focus on the distribution of field strengths at the horizontal plane  $z = \langle z_{0.1} \rangle$  (i.e. ignore the  $y$ -axis). A few minutes after the initial appearance of flux at the surface ( $t = 17.7$  min), the vertical field strengths do not exceed 500 G. Some time later, at  $t = 34.6$  min, a small fraction of the vertical flux concentrations have field strengths of up to 700 G in the horizontal plane  $z = \langle z_{0.1} \rangle$ . At



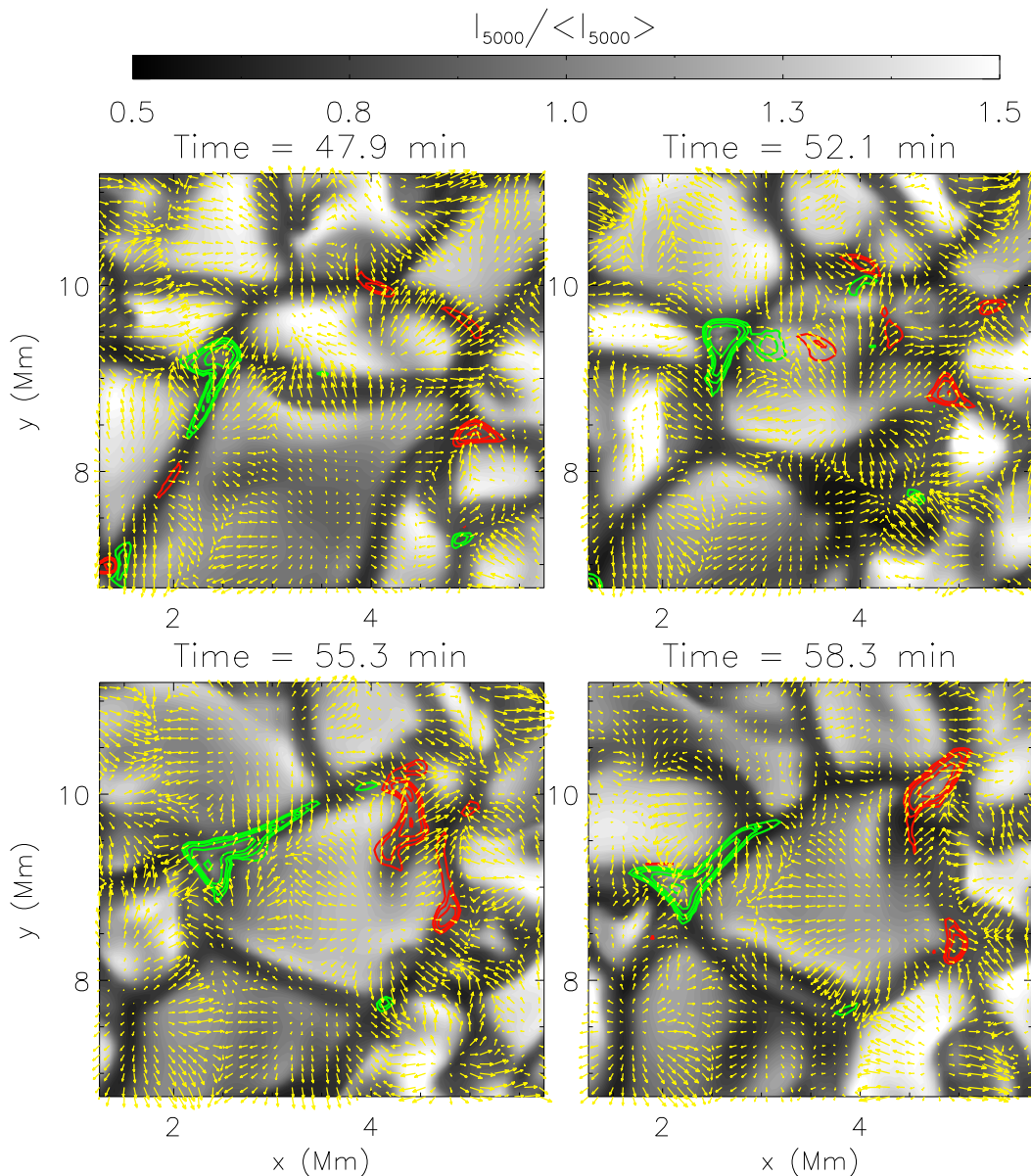


Figure 5.7: This time sequence shows the coalescence of newly emerged magnetic concentrations with pre-existing surface field. The grey scale in each panel indicates the normalized continuum intensity at  $5000 \text{ \AA}$  ( $I_{5000} / \langle I_{5000} \rangle$ ). The vector overlays indicate the horizontal velocity field at optical depth  $\tau_{5000} = 0.1$  and the contour overlays indicate  $B_z$  at the same optical depth at the levels  $\pm[100, 200, 400, 800, 1600] \text{ G}$ . Green (red) contours correspond to positive (negative) polarities. At  $t = 47.9 \text{ min}$ , a bipole centered at  $[x, y] = [3.5, 9.2] \text{ Mm}$  is emerging through a granule. Flux expulsion leads to a coalescence between the pre-existing positive flux with the positive part of the newly emerged flux.

$t = 61.1$  min, we find even stronger fields, approaching  $|B_z| = 1$  kG at  $z = \langle z_{0.1} \rangle$ .

The appearance of stronger magnetic fields several granulation timescales after the initial emergence of flux suggests that some type of *convective intensification* mechanism may be operating. From our synthetic magnetograms from run U5, we find that the maximum value of  $|B_z|$  that exists within a vertical magnetic bundle with a flux  $\Phi$  is an increasing function of  $\Phi$ . In order to identify individual flux bundles from our magnetograms, we choose some threshold,  $B_{\text{threshold}}$ . For each discrete region in the magnetogram with  $|B_z| \geq B_{\text{threshold}}$ , we measured the value of the maximum value of  $|B_z|$  in the region as well as the amount of flux contained within the region. A scatter plot of these two quantities are shown in Fig. 5.9. The crosses, diamonds and squares indicate values from magnetograms taken at  $t = 17.7$ ,  $t = 34.6$  and  $t = 61.1$  min respectively. The threshold used for this plot was  $B_{\text{threshold}} = 50$  G. The scatter plot clearly shows that larger flux bundles can support stronger internal field strengths. This trend is not sensitive to the threshold value used. Our finding is compatible with the work of Venkatakrishnan (1986), who predicted the radiative heating of flux tubes by their surroundings inhibits the intensification of the flux tubes. The observational study by Solanki et al. (1996) also supports his prediction. We must point out, however, that the various types of diffusion present in the simulation have effects which are more prominent for smaller flux bundles. For instance, a flux bundle with a mean field strength of 100 G and a flux of  $10^{16}$  Mx has a radius of about 50 km, which is the horizontal grid spacing used in our simulations. We must therefore keep in mind, that the trend in the scatter plot in the range  $\Phi \lesssim 10^{17}$  Mx are influenced by diffusion.

In the same vertical flux concentrations, the value of  $|B_z|$  evaluated at  $\tau_{5000} = 0.1$  is actually larger, approaching 1 kG. The reason for this apparent discrepancy is simply that the  $\tau_{5000} = 0.1$  level in the stronger field regions have been displaced downwards. This effect is indicated by the second row in Fig. 5.8, which consists of JPDFs of  $z_{0.1} - \langle z_{0.1} \rangle$  against  $|B_z|$  at  $\tau_{5000} = 0.1$ . The quantity  $z_{0.1} - \langle z_{0.1} \rangle$  is the displacement of the local  $\tau_{5000} = 0.1$  level from the mean geometrical height of this optical depth (i.e. *Wilson depression*). We find that at  $t = 34.6$  min, the regions with the strongest fields suffer the deepest depression (of the  $\tau_{5000} = 0.1$  surface).

The aforementioned effect is even more pronounced at  $t = 61.1$  min. At this instant, we find even stronger field strengths than before. The discrepancy between the value of  $|B_z|$  at  $z = \langle z_{0.1} \rangle$  and its value at  $\tau_{5000} = 0.1$  is even greater. The maximum field strength at  $z = \langle z_{0.1} \rangle$  is 1 kG. This is not very surprising if we compare the magnetic pressure of a 1 kG magnetic field with the horizontally averaged gas pressure in that plane. The two values are almost equal. This comparison tells us that, if there exists a totally evacuated magnetic structure with a field strength higher than 1 kG at the height  $z = \langle z_{0.1} \rangle$ , it would tend to expand in order to maintain pressure balance with its surroundings. The expansion would then weaken the field strength. Now, when we look at the distribution of  $|B_z|$  at  $\tau_{5000} = 0.1$  at  $t = 61.1$  min, we find field strengths approaching 1.5 kG. Again, the reason for the discrepancy is the depression of surfaces of constant optical depth inside strong magnetic fields. This depression is a consequence of the partial evacuation of vertical flux concentrations leading to a modification of the internal temperature and density structure. As a result, the  $\tau_{5000} = 0.1$  (or 1 etc) level is located geometrically deeper in vertical magnetic regions. This means that the distribution of  $|B_z|$  evaluated at this optical depth samples the deeper layers of the magnetic flux concentrations, where

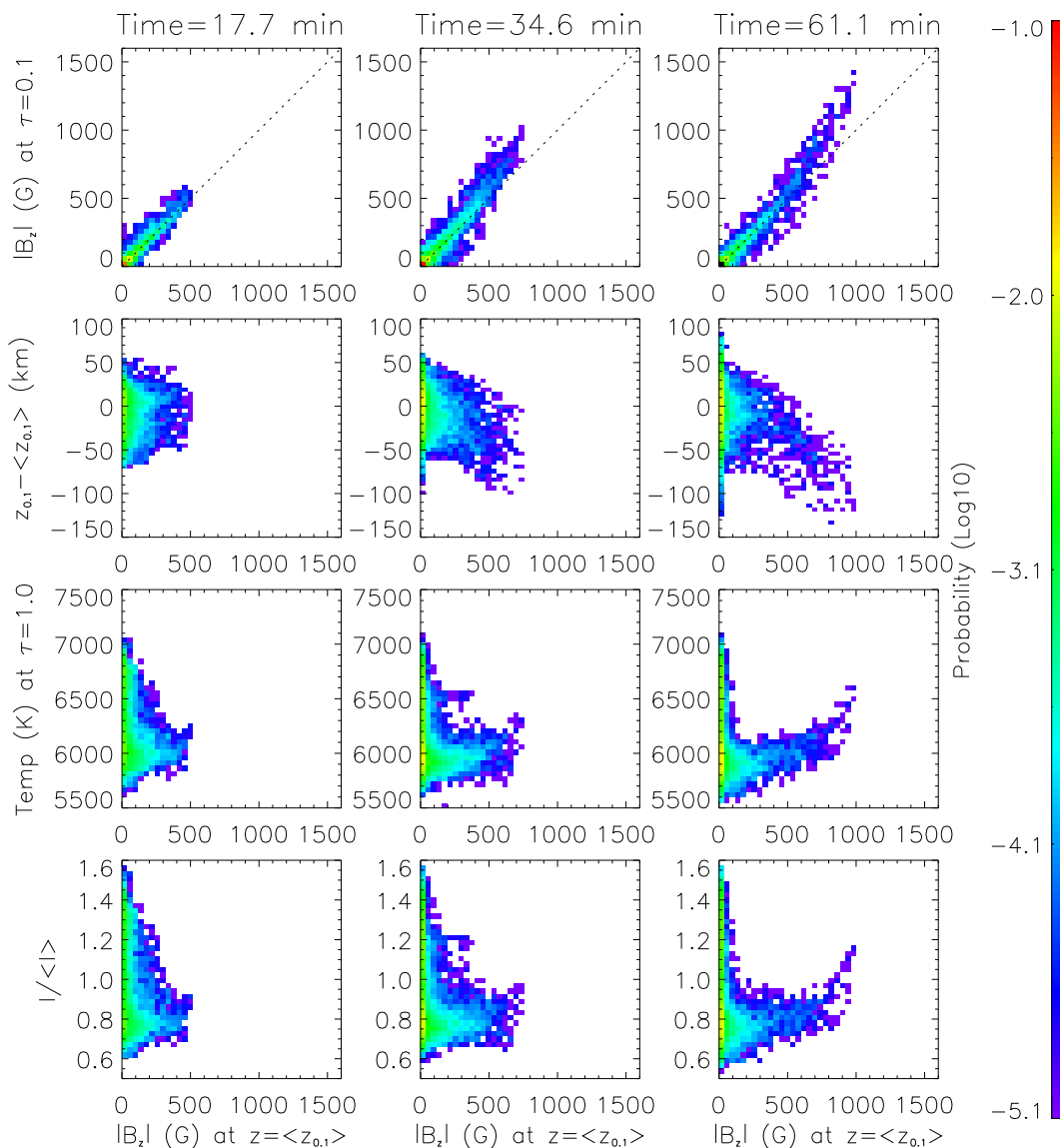


Figure 5.8: Joint probability distribution functions (JPDFs) for different surface quantities in run U5. *First row*: JPDF between the value of  $|B_z|$  at a plane of constant geometrical height  $z = \langle z_{0.1} \rangle$  and its value evaluated at  $\tau_{5000} = 0.1$ . *Second row*: JPDF between the value of  $|B_z|$  at  $z = \langle z_{0.1} \rangle$  and the local vertical displacement of the  $\tau_{5000} = 0.1$  surface from the mean geometrical height of the surface corresponding to this optical depth ( $z_{0.1} - \langle z_{0.1} \rangle$ ). *Third row*: JPDF between  $|B_z|$  at  $z = \langle z_{0.1} \rangle$  and the temperature at  $\tau_{5000} = 1.0$ . *Fourth row*: JPDF between  $|B_z|$  at  $z = \langle z_{0.1} \rangle$  and the normalized emergent continuum intensity at  $5000 \text{ \AA}$ . The three columns show the JPDFs at three different times. The color coding indicates the logarithm of the probability.

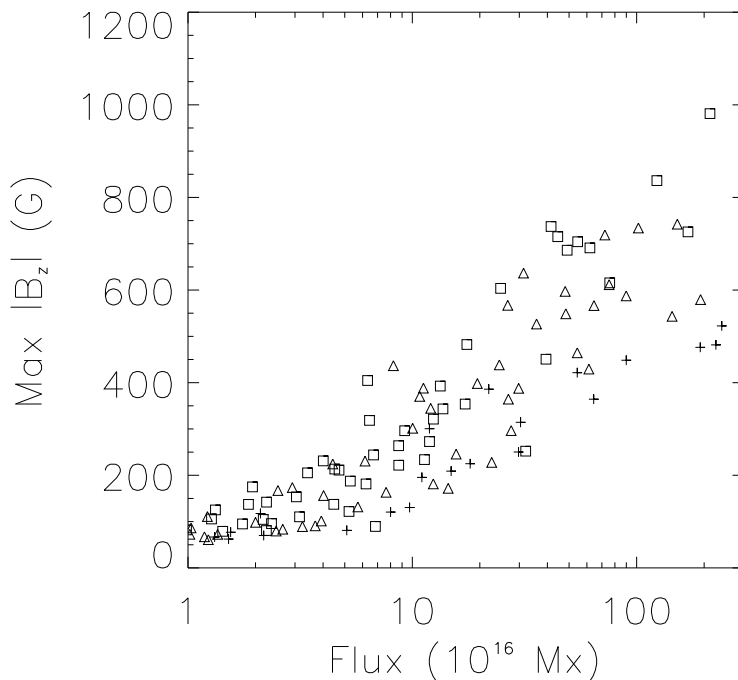


Figure 5.9: Scatter plot of the maximum value of  $|B_z|$  in an individual magnetic flux concentration against the amount of vertical flux contained in the flux concentration. The values of  $|B_z|$  were evaluated at the plane of constant geometrical height,  $z = \langle z_{0.1} \rangle$ . The crosses, diamonds and squares indicate values from magnetograms taken at  $t = 17.7$ ,  $t = 34.6$  and  $t = 61.1$  min respectively.

the flux concentrations are more compact, and thus have enhanced field strengths.

The partial evacuation of vertical flux concentrations lead to another observational signature. From the Eddington-Barbier relation, we know that the emergent intensity at  $\mu = 1$  is approximately given by the source function at  $\tau = 1$ . The panels in the third row of Fig. 5.8 show JPDFs between  $|B_z|$  at  $z = \langle z_{0.1} \rangle$  and the temperature at  $\tau_{5000} = 1.0$ . The temperature at optical depth unity is higher in strong field regions. This explains why the brightness of vertical flux tubes increases with  $|B_z|$  (see fourth row of Fig. 5.8). We will return to the topic of convective intensification in Section 5.4.1, where we describe in detail the physical mechanism of the intensification process for a particular example.

### 5.3.2 Emergence of strong magnetic field

In this section we discuss the observational signatures of the emerging flux tube with  $B_0 = 8500$  G (run U1), which is strong enough to resist being passively deformed and advected by the convective flow. When it emerges, its expansion leads to a modification of the granulation pattern. Fig. 5.10 shows a time sequence of the emergent continuum intensity throughout the emergence event (grey scale). The vector overlays indicate the horizontal components of the velocity field at  $\tau_{5000} = 0.1$ . Fig. 5.11 shows accompanying



synthetic magnetograms for this emergence event.

We have seen that the emergence morphology of the field in run U5 is dictated by the convective motion of the near-surface layers. In run U1 (where the magnetic field is several times stronger), the convection still has an appreciable influence on the emergence morphology. Comparison of the magnetogram and the intensity image at  $t = 8.6$  min clearly shows that magnetic flux emerges preferentially within the interior of granules. The accompanying magnetograms show mainly positive (negative) polarity flux in the upper (lower) half of the field of view. This is due to the twist in the tube, which is also indicated by the vector plot of the horizontal field.

Having pointed out the importance of convection on the emergence morphology, we must also point out the influence of the emerging magnetic field on the local granulation pattern. The intensity image at  $t = 8.6$  min shows that granules coincident with the emerging flux are somewhat aligned along the direction of the tube axis. Furthermore, these granules are relatively large (covering an area of up to  $9 \text{ Mm}^2$ ). The disturbance of the granulation by the emerging magnetic field is most prominent at  $t = 11.2$  min. The intensity image at this time shows a darkening which extends the full horizontal extent of the simulation domain. This darkening is extended but is not coherent along its entire length. There exist bright patches on either side of the darkening but their shapes are distinctly different from that of normal granules. As is shown in Fig. 5.4, the expansion of the emerging tube drives horizontal outflows away from the emergence site. These outflows can be seen in the vector plots in the central panel of Fig. 5.10. The synthetic magnetogram for the same instant shows that much of the emerged flux already resides in the intergranular lanes.

At  $t = 16.9$  min, we no longer find an extended darkening along the length of the domain. Rather, the region formerly occupied by the extended dark lane is replaced by the usual granulation pattern. These granules are generally elongated in the  $y$ -direction because of the horizontal outflows driven by the expanding tube. In the accompanying synthetic magnetogram, we find that the emerged magnetic flux outlines the boundaries of these new granules. The  $y$ -component of the magnetic field is on average pointed towards the positive  $y$ -direction. This is just the opposite to what we see in the magnetogram at  $t = 8.6$  min. This reversal of the sign of  $B_y$  within this time span is expected. In the earlier snapshot, the  $\tau_{5000} = 0.1$  surface intersects with the upper half of the flux tube. The twist of the field lines within the tube is such that  $B_y < 0$  in this part of the tube. In the latter snapshot, the lower half of the tube has emerged at the surface, and so the synthetic magnetogram shows field with predominantly  $B_y > 0$ .

### 5.3.2.1 The relation between field strength and zenith angle

Lites et al. (1998) have observed several emerging flux regions using the Advanced Stokes Polarimeter. The acquisition of the full Stokes profiles have allowed them to carry out inversions to obtain vector magnetograms of these regions. Based on their observations, Lites et al. (1998) described the following scenario for flux emergence: Magnetic flux emerges at the surface in the form of horizontal field, with field strengths of 200–600 G (in any case, sub-kilogauss). After emergence, the field quickly migrates away from the emergence site. In the process, the field becomes vertical. Only when the field has become vertical, do the fields obtain field strengths exceeding one kilogauss. The observational

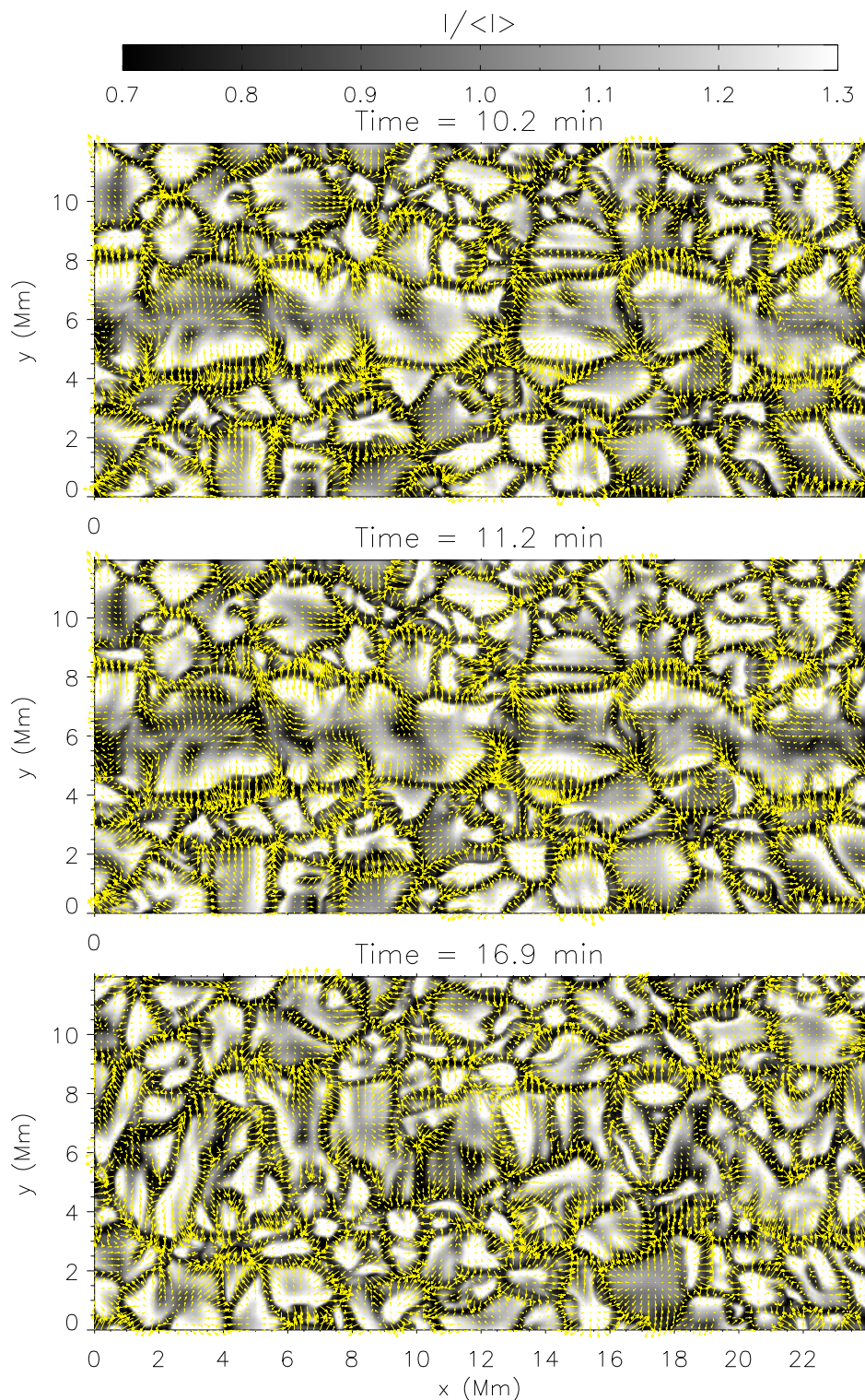


Figure 5.10: The emergence of the flux tube in run U1 ( $B_0 = 8500$  G) temporarily disturbs the granulation pattern. Shown above is a time sequence of the emergent continuum intensity at  $5000 \text{ \AA}$ . The vector overlays indicate the horizontal components of the velocity at  $\tau_{5000} = 0.1$ . A vector of length corresponding to one grid-spacing on the vector plot corresponds to a magnitude of  $v = 3 \text{ km s}^{-1}$ . The appearance of a transient darkening along the length of the domain marks the site of emergence.

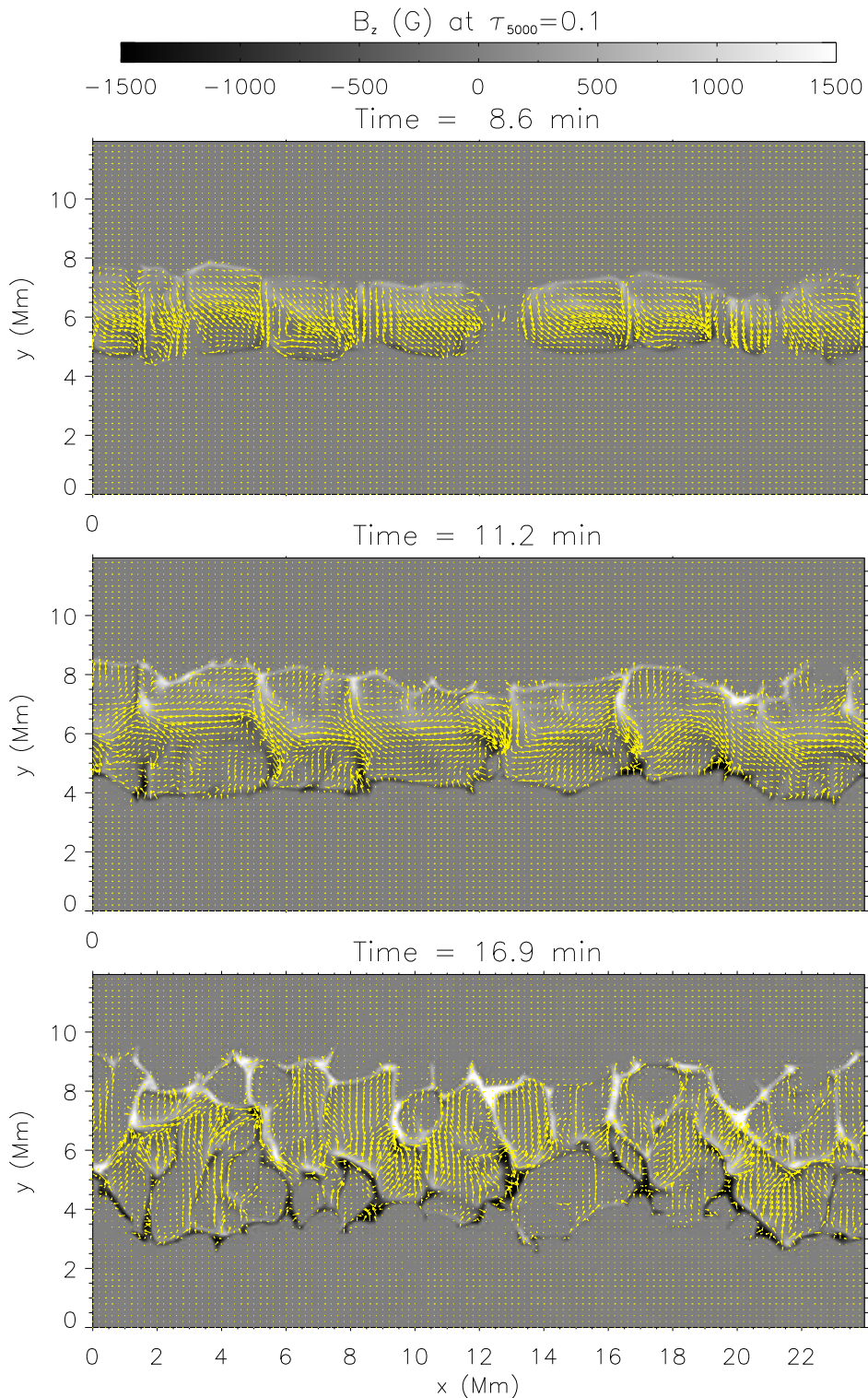


Figure 5.11: Synthetic magnetograms accompanying Fig. 5.10. The vertical and horizontal components of the magnetic field at  $\tau_{5000} = 0.1$  are indicated by the grey scale and vector overlays respectively. A vector with a length of one grid-spacing on the vector plot corresponds to a field strength of  $|B| = 400$  G.



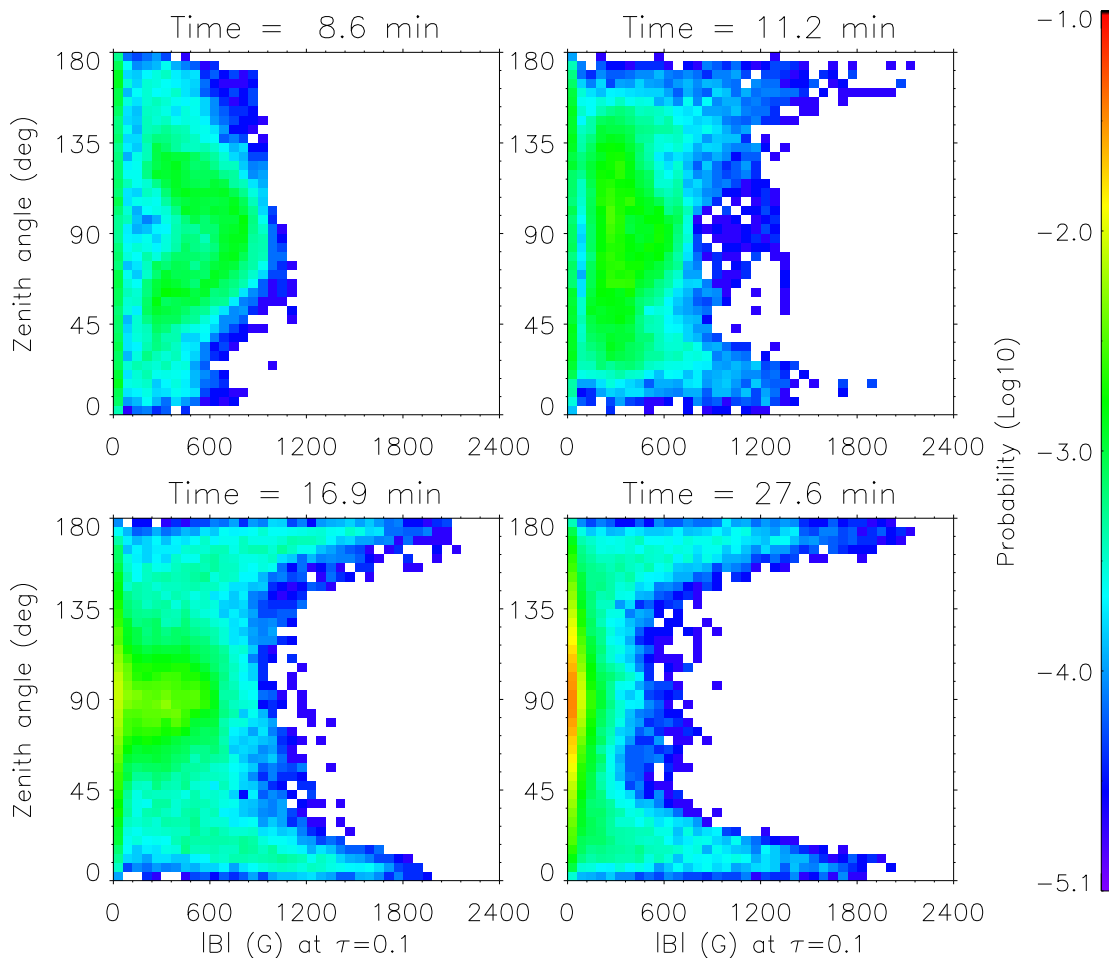


Figure 5.12: Joint probability distribution functions (JPDFs) of the zenith angle of the magnetic field vector versus the absolute field strength  $|B|$ . Both quantities have been evaluated at the  $\tau_{5000} = 0.1$  level. A zenith angle of  $90^\circ$  corresponds to a purely horizontal field. The four panels show the JPDFs at four different times. At  $t = 8.6$  min, the flux tube is emerging at the surface and the strongest fields are predominantly horizontal. Kilogauss fields are almost exclusively vertical.

study by Kubo et al. (2003) also supports these findings.

At  $t = 8.6$  min in Figs. 5.10 and 5.11, the flux tube is just emerging at the surface. The JPDF at this time reflects the fact that the flux tube is still coherent. The horizontal fields are stronger than the vertical fields. Although a tiny fraction of the horizontal fields have kilogauss field strengths, most are confined within the range  $400 \leq |B| \leq 1,000$  G. Just five minutes later, at  $t = 11.2$  min, the distribution in the JPDF looks very different. The appearance of two ‘horns’ in the JPDF near  $\gamma = 0^\circ$  and  $\gamma = 180^\circ$  indicates the effect of the granular flow on the emerged field. As the emerged field is advected to the boundaries of granules (i.e. flux expulsion), it is also rotated so that it becomes predominantly vertical. As the simulation progresses in time, the two horns in the JPDF become more distinct. At  $t = 27.6$  min, nearly all the field with  $|B| \geq 600$  G are vertical. There is actually an

abundance of horizontal fields, however, these are confined to strengths of less than 600 G. The shape of the JPDF at this time is similar to the scatter plots of zenith angle vs.  $|B|$  measured in emerging flux regions by Lites et al. (1998) and by Kubo et al. (2003).

### 5.3.2.2 Anomalous transient dark lane

The physical properties of the extended dark lane is distinctly different from those of normal intergranular lanes. In the quiet Sun in the absence of magnetic flux emergence, the intergranular lanes are dark and associated with cold downflowing material (see Section 3.3). The anomalous dark lane that results from the emergence of the flux tube in run U1 is associated with *upflowing* material for a substantial fraction of the dark lane's lifetime (several minutes). Fig. 5.13 shows the normalized emergent continuum intensity at  $t = 11.2$  min (same as the central panel in Fig. 5.7). Overplotted on the grey scale image are contours of the vertical component of the velocity at  $\tau_{5000} = 0.1$  for magnetic regions ( $|B| \geq 400$  G). The green contours indicate upflows with  $v_z = [0.5, 1]$  km s<sup>-1</sup> and the red contours indicate downflows with  $v_z = [-1, -0.5]$  km s<sup>-1</sup>. There is a substantial overlap of the green contours with regions on the surface comprising the dark lane. The correlation between upflows and low emergent intensity in the dark lane is also illustrated in Fig. 5.14. Plotted in this figure are average profiles of the normalized emergent continuum intensity and the vertical velocity at  $\tau_{5000} = 0.1$  across the dark lane (in the  $y$ -direction). The plotted values are averages taken along the  $x$ -direction at time  $t = 11.2$  min. Away from the emergence site, there is a clear correlation between bright regions ( $I_{5000}/\langle I_{5000} \rangle > 1$ ) and upflows ( $v_z > 0$ ). Again, we see that within the emergence site ( $y \sim 6$  Mm), the darkening ( $I_{5000}/\langle I_{5000} \rangle \approx 0.93$ ) is co-spatial with upflowing material ( $v_z = 0.5 - 1$  km s<sup>-1</sup>).

The lifetime of the extended dark lane is about 10 minutes, which is comparable to the granulation time. For the first few minutes of the dark lane's lifetime, the regions of lower brightness are associated with upflowing material with rise speeds of up to 1 km s<sup>-1</sup>. This is substantially lower than the typical rise speed ( $v \approx 2 - 4$  km s<sup>-1</sup>) of magnetic material when it is just emerging at the visible surface. In the last few minutes of the dark lane's lifetime, the dark lane splits up into spatially separated, dark elongations with length of about 2 Mm (see intensity image at  $t = 16.9$  min in Fig. 5.10). The vertical velocities of these dark elongations are negative, indicating regions of downflows.

The presence or absence of a transient dark lane as an observational signature of flux emergence depends on the initial field strength as well as the initial twist carried by the tube. When the initial flux tube is sufficiently weak that it has relatively small buoyancy (as is the case with run U5), a dark lane does not appear. The reason for this is simple: In order for the dark lane to appear, the emerging field must be strong enough that its evolution is not completely controlled by the convective flow. However, the flux tube having a strong field is not a sufficient criterion. The amount of initial twist is also important. We have carried out simulation runs with the same initial conditions for the flux tube as in run U1, varying only the amount of the initial twist. We found that for a flux tube with twist parameter  $\lambda = 0$ , there is no transient dark lane marking the emergence site of the tube. For a flux tube with a moderate amount of twist,  $\lambda = 0.25$ , we find the transient appearance of some dark patches within the granules where the emergence occurs. These patches, however, do not exhibit a clear alignment or coherence as is the case in run U5

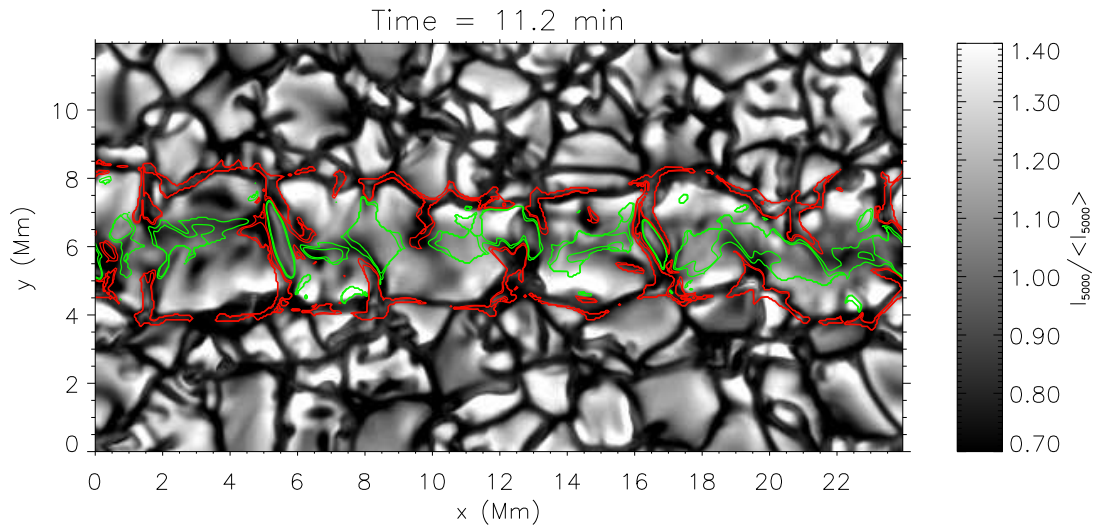


Figure 5.13: The anomalous dark lane ( $y \sim 6$  Mm) that appears in run U1 is roughly coincident with upflowing material. The grey scale in this image indicates the normalized emergent continuum intensity at  $t = 11.2$  min. The green (red) contours indicate the vertical velocity at the levels  $+(-)$   $[0.5, 1]$   $\text{km s}^{-1}$ .

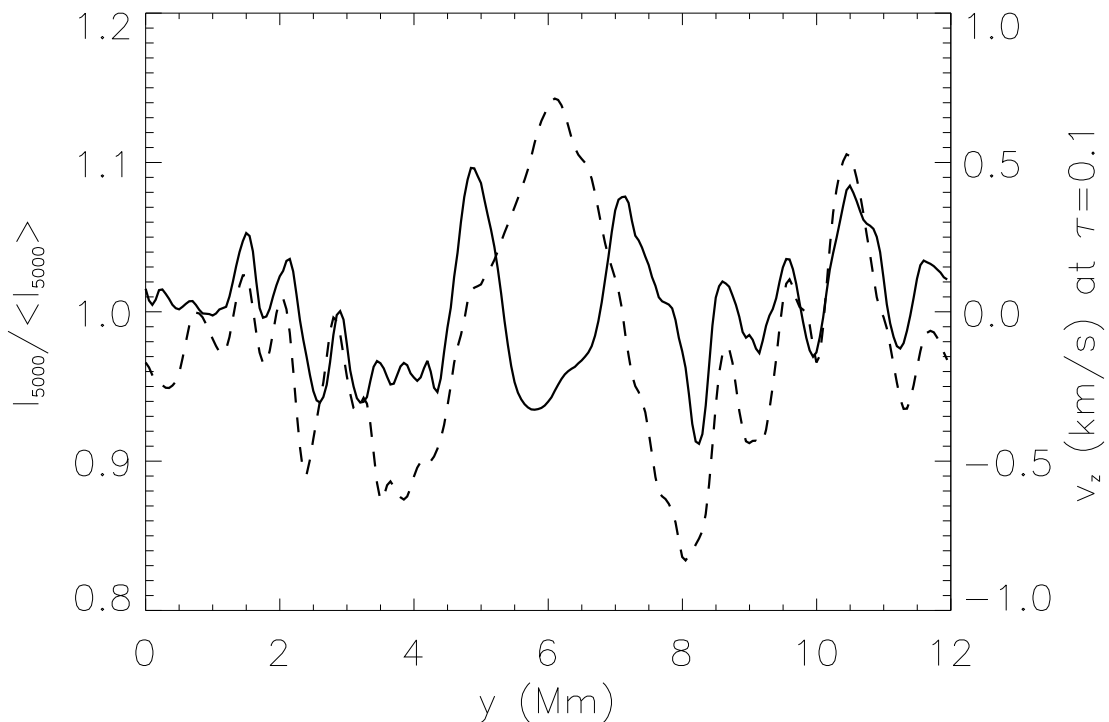


Figure 5.14: Average profiles of the normalized continuum emergent intensity (solid line) and vertical velocity at  $\tau_{5000} = 0.1$  (dashed line) across the dark lane at  $t = 11.2$  min. The values indicated are averages over the  $x$ -direction.

(where  $\lambda = 0.5$ ).

The following explanation accounts for the properties we have presented above: When a flux tube (with a flux of, say,  $\Phi_0 = 10^{19}$  Mx) reaches the surface, it has a rise speed of  $2 - 4$  km s<sup>-1</sup>. As we found out in Section 4.2.3, the amount of twist in the tube determines whether it can remain a coherent structure (large  $\lambda$ ) or break up into vortex fragments (small  $\lambda$ ). As the flux tube emerges and cools by radiation, the flux tube loses buoyancy. Nevertheless, the emerged magnetic material may still overshoot. If the flux tube is sufficiently twisted, its core will remain largely intact and overshoot into the photosphere. This happens despite the flux tube having lost its buoyancy by radiative cooling. As the emerged magnetic material of the tube overshoots, its upwards motion is braked by the stable stratification. This is why the synthetic Dopplergram in Fig. 5.13 shows upwards velocities limited to  $0.5 - 1$  km s<sup>-1</sup> within the dark lane. The coolness of the magnetic material at optical depth unity accounts for the lane's darkness. The arrangement of the cool and dense material in an extended lane configuration is not stable to perturbations introduced by granular dynamics. Within a few minutes, the extended dark lane breaks up into shorter elongations with lengths comparable to those of intergranular lanes. The acceleration of the dense material by gravity either leads to the birth of new downflows, or feeds pre-existing downflows in the intergranular network. The influence of the granular dynamics on its evolution explains why the dark lane has a lifetime comparable to the granulation timescale.

Transient appearance of dark alignments in emerging flux regions (EFRs) have been reported by a number of observational studies (Bray et al. 1984, Brants and Steenbeek 1985, Zwaan 1985, Strous and Zwaan 1999). The darkening occurs in both the continuum as well as in the core of a spectral line, and is spatially coincident with upflows beyond  $0.5$  km s<sup>-1</sup>. The orientation of the alignment is roughly parallel to the axis connecting the two developing polarities of the active region. Strous and Zwaan (1999) have identified 111 individual emergence events in an EFR and have carried out a statistical analysis of these events. They find that transient darkenings in the line core and in the continuum, lasting about 10 minutes, are robust signatures of emergence events. The typical length of the darkenings is about 2 Mm and they are aligned roughly parallel to the axis connecting the two developing polarities of the active region. Their analysis also establishes that the darkenings are associated with upflows of about  $0.5$  km s<sup>-1</sup>. All these properties are in agreement with the simulation results from U5. In addition, Strous and Zwaan (1999) also report that the darkenings, on average, rotate counterclockwise at about  $0.5^\circ$  min<sup>-1</sup>. In run U5, we do find that some of the dark elongations rotate during the breakup of the dark lane. However, we do not find any systematic direction in which the rotation occurs.

## 5.4 Emergence of an arched magnetic flux tube

So far, we have only considered simulations of flux tubes which were initially imparted with a uniform specific entropy distribution (which is closely related to a uniform buoyancy distribution). These simulations have taught us much about the physics of photospheric flux emergence and have explained many of their observed properties. We have found that, despite the flux tube being uniformly buoyant along its axis, the surrounding upflows and downflows introduced undulations along the tube so that it consists of an al-

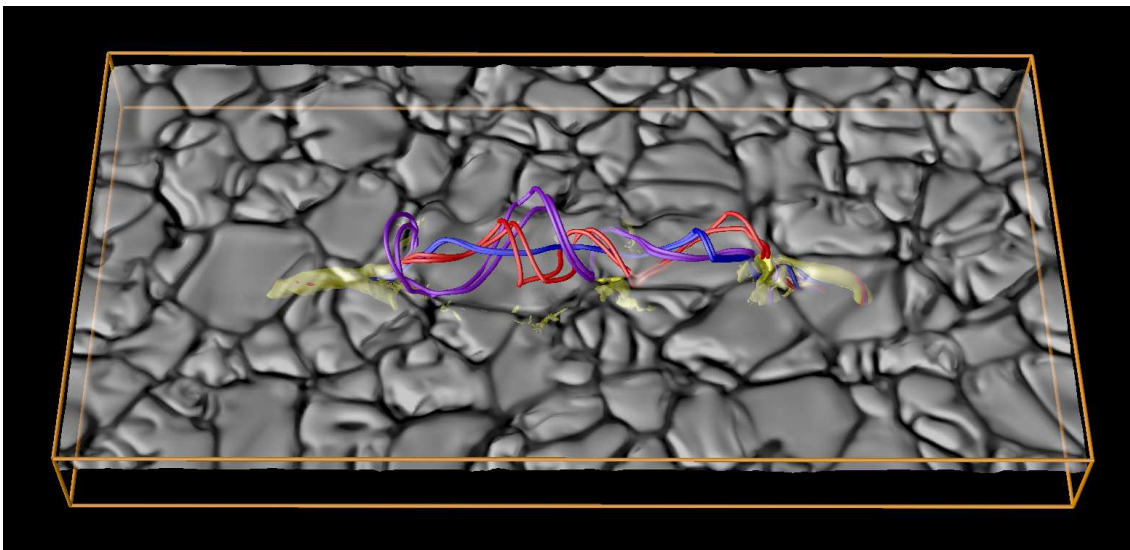


Figure 5.15: 3D rendering of the arched flux tube in run L1 at  $t = 11.8$  min. The grey scale shaded surface indicates the vertical velocity (within the range  $\pm 3 \text{ km s}^{-1}$ ) at optical depth  $\tau_{5000} = 1$ . The subsurface trunks of the arched flux tube are indicated by the yellow isosurfaces of  $|B| = 2000 \text{ G}$ . The winding of the different field lines around the axis of the tube shows the inherent twist within the tube.

ternating series of crests and troughs. The typical wavelength of this undulation is about  $1 - 2 \text{ Mm}$ , which is the characteristic length scale for the granulation itself. For this reason, the magnetic field of the tube emerges at the surface as an alignment of loops with the horizontal tops of the loops emerging through the centres of granules. In this sense, we can say that magnetic fields emerge at the surface as arched loops. However, bipolar magnetic regions are observed to emerge all over the surface with the property that the final separation between the two poles is much greater than the size of a granule (Zwaan 1985). The most extreme example is that of large active regions, whose polarities can be up to hundreds of Mm apart. Then there are smaller bipolar regions, such as ephemeral regions, whose bipoles can be separated by a few to tens of Mm (Hagenaar 2001). This property points to a larger-scale undulation of the subsurface structure of emerging flux bundles.

Motivated by the discussion above, we have carried out a simulation to study how an arched flux tube emerges at the surface (run L1). For this simulation, the initial specific entropy within the tube varies along the axial direction of the tube according to the profile

$$s(x) = s_0 + (s_{\text{up}} - s_0) \cos^2 \left( \frac{[x - x_0]\pi}{L_x} \right), \quad (5.7)$$

where  $x_0 = 12 \text{ Mm}$  and  $L_x = 24 \text{ Mm}$  is the length of the domain in the  $x$ -direction. The distribution of  $s$  in each cross-section perpendicular to the tube axis is uniform. The cross-section of the tube at  $x = 0 \text{ Mm}$  is initially imparted with a specific entropy of  $s_0 = 5.1R^*$ , which is comparable to the value of  $s$  of anti-buoyant material near the visible surface. This implies that segments of the tube near  $x = 0 \text{ Mm}$  are anti-buoyant, and will tend to sink. In contrast, segments of the tube near  $x = 12 \text{ Mm}$  are buoyant because they have higher specific entropy. The maximum of the specific entropy profile



is located at  $x = 12$  Mm, where it takes a value  $s = s_{\text{up}}$ . By pre-loading the tube with a varying entropy distribution along the tube axis, we induce it to develop into an  $\Omega$ -type loop structure with the apex of the loop near  $x = 12$  Mm.

Apart from the initial specific entropy profile, the flux tube in run L1 has the same initial properties as the tube in run U1. In both cases, the field strength at the tube axis is  $B_0 = 8500$  G and the twist parameter is  $\lambda = 0.5$ . The longitudinal magnetic flux of the tube is  $10^{19}$  Mx. Fig. 5.15 shows a 3D rendering of the arched flux tube as it emerges into the photosphere ( $t = 11.8$  min). This image is intended to provide the reader with a 3D image of the emerging loop, which will facilitate the discussion in the following sections. The granulation pattern can be discerned from the grey scale shaded surface, which indicates the vertical velocity at optical depth unity. At this instant, the crest of the flux tube is just passing through the visible surface. The subsurface trunks of the arched flux tube is indicated by the yellow shaded isosurfaces of  $|B| = 2000$  G. The field lines show how the two trunks are connected. The winding of the field lines is due to the intrinsic twist of the tube ( $\lambda = 0.5$  initially).

#### 5.4.1 Appearance of bright grains at the footpoints of the loop

As mentioned in Section 5.3.2.2, Strous and Zwaan (1999) found that transient darkenings are robust observational signatures of emerging flux. In the same study, they also found that the transient darkenings are followed by the appearance of bright grains flanking the ends of the darkenings. The bright grains coincide with magnetic flux concentrations and downflows. In many cases, a single bright grain is found at one end of a darkening. Occasionally, both ends of the darkening are flanked by bright grains. In these cases, the flux concentrations associated with the pair of bright grains have the opposite polarity and the orientation of the pair is consistent with the larger-scale orientation of the two polarities of the developing active region. After their initial appearance, the bright grains separate with an average speed of  $1.4 \text{ km s}^{-1}$ . Based on these findings, Strous and Zwaan constructed a heuristic model, in which they interpret the transient darkening as the crest of an emerging loop and the bright grains at the flanks as the photospheric footpoints of the loop.

Our simulation of the emergence of an arched flux tube yields observational signatures that are compatible with this model. Fig. 5.16 shows a time sequence of the normalized continuum intensity over the course of the emergence event and Fig. 5.17 shows the accompanying synthetic vector magnetograms. The green (red) contours indicate the vertical velocity at levels of  $+ (-) [0.5, 1] \text{ km s}^{-1}$  for regions with  $|B| \geq 300$  G.

At  $t = 11.8$  min, we find the arched flux tube emerging through the surface. The magnetogram shows an elongated magnetic complex covering a surface area of about  $10$  by  $3 \text{ Mm}^2$ . At the left and right ends of the magnetic complex, we find predominantly positive and negative polarity flux, respectively. The interior of the complex is a region of predominantly upflowing material but does not appear like it consists of normal granules. The edge of the magnetic complex is outlined by downflows. Let us focus our attention on the negative flux concentration at the right end of the magnetic complex. This flux concentration resides in a downflow and appears relatively dark ( $I \approx 0.8 - 0.9 \langle I_{5000} \rangle$ ). A couple of minutes later, at  $t = 14.1$  min, the same feature has been displaced towards the right by about  $0.5$  Mm. In the meantime, it has brightened to an intensity of  $1.5 \langle I_{5000} \rangle$ .

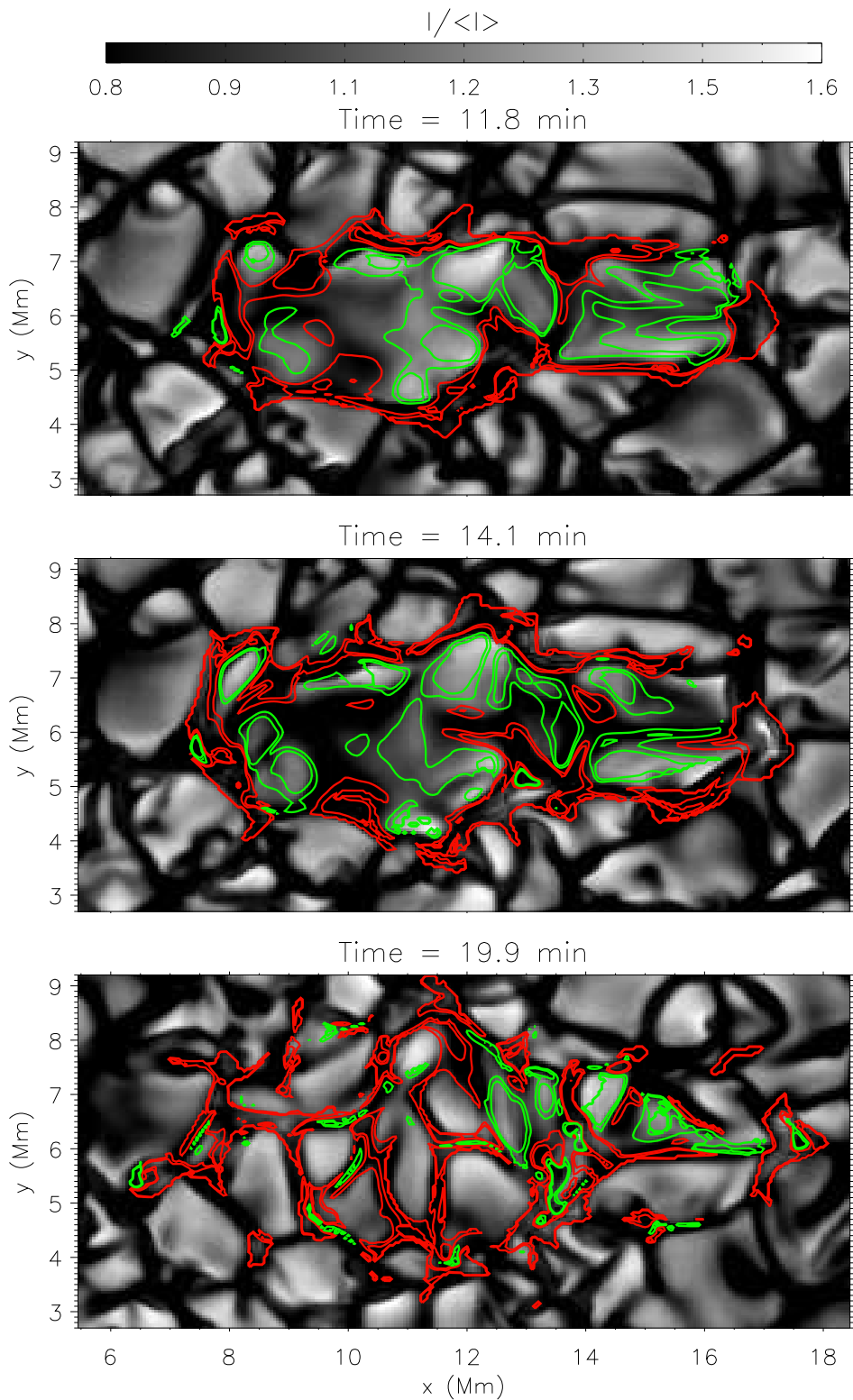


Figure 5.16: Time sequence of intensity images for the emergence of an arched flux tube (run L1). The green (red) contours indicate the vertical velocity at levels of + (–)  $[0.5, 1]$   $\text{km s}^{-1}$  for regions with  $|B| \geq 300$  G. At  $t = 14.1$  min, a bright grain with a peak intensity of  $I_{5000} = 1.6\langle I_{5000} \rangle$  appears at the right end of the magnetic complex. This bright grain coincides with a downflow in a magnetic concentration.

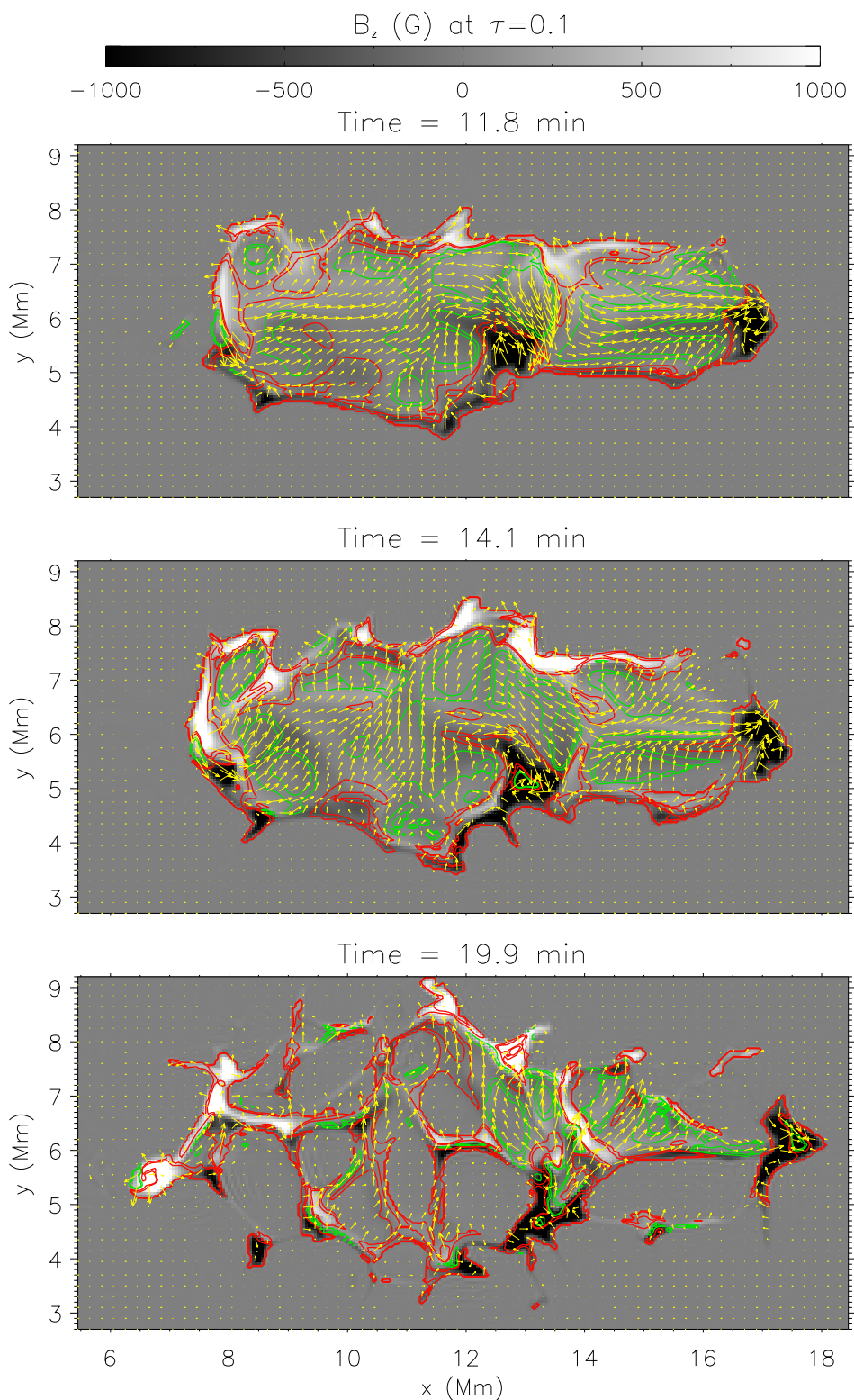


Figure 5.17: Accompanying synthetic vector magnetograms for Fig. 5.17. The grey scale indicates the vertical field  $B_z$  and the vector overlay indicates the horizontal components of the field. A vector with a length of one grid spacing on the vector plot has a magnitude of 300 G.

Immediately to the l.h.s. of this bright magnetic concentration is an example of the transient anomalous darkening we found in Section 5.3.2.2. This darkening has a length of about 2 Mm and is associated with upflowing material with a rise speed of  $0.5 - 1 \text{ km s}^{-1}$ . If we go back to the intensity image at  $t = 11.8 \text{ min}$ , we see that the darkening was already in progress at that time. In our simulation, the two footpoints of the loop (at the extreme left and right ends of the magnetic complex) separate with a speed of about  $3 - 4 \text{ km s}^{-1}$ , which also compares favorably with the result of Strous and Zwaan (1999).

The appearance of the bright grain is a consequence of a *convective intensification* of the flux concentration (Grossmann-Doerth et al. 1998). We refer to Fig. 5.18 to explain the underlying physical mechanism. The six panels in this figure show profiles of different quantities along a horizontal cut (at  $y = 6.1 \text{ Mm}$ ) through the magnetic flux concentration associated with the bright grain. The profiles are shown for three different times:  $t = 9.8 \text{ min}$  (dash-dotted lines),  $t = 11.8 \text{ min}$  (dashed lines) and  $t = 14.1 \text{ min}$  (solid lines). The top left panel shows the temperature structure within and around the flux concentration *after* intensification (at  $t = 14.1 \text{ min}$ ).

The intensification proceeds as follows: radiative cooling ( $Q_{\text{rad}} < 0$ ) of material in the surface layers of the magnetic concentration drives a downflow, which partially evacuates the predominantly vertical magnetic concentration. This causes a lateral compression of the magnetic concentration, which increases the field strength at the core of the concentration from a value of about 700 G to 1,200 G at the horizontal level  $z = \langle z_{0.1} \rangle$ . The downflow and the radiative cooling modify the temperature structure within the magnetic concentration so that, at the same geometrical height, the tube is cooler than its surroundings. The temperature deficit also means a reduction of the internal opacity, which causes a local depression of surfaces of constant optical depth. At  $t = 11.8 \text{ min}$ , the  $\tau_{5000} = 1.0$  level in the core of the concentration is already lowered from the average level by about 150 km. At  $t = 14.1 \text{ min}$ , the surfaces of constant optical depth are even lower. At this time, the  $\tau_{5000} = 1.0$  level in the flux concentration is 300 km below  $z = \langle z_{1.0} \rangle$ . The  $\tau_{5000} = 0.1$  level in the flux concentration is displaced downwards by a similar amount. This vertical displacement is comparable to about two pressure scale heights at the surface. We can crudely estimate that, over such a vertical displacement, the magnetic pressure would increase by a factor of about  $e^2$  and the magnetic field strength to increase by a factor of  $e$ . In fact, the field strength evaluated at  $\tau_{5000} = 0.1$  at  $t = 14.1 \text{ min}$  is  $|B_z| = 2500 \text{ G}$ , approximately 2.1 times the value at  $z = \langle z_{0.1} \rangle$ .

The partial evacuation and cooling of the flux concentration means that the  $\tau_{5000} = 1.0$  surface probes deeper into the flux concentration. The lateral radiative heating of the interior of the magnetic concentration from the sidewalls is crucial for the brightening of the structure. Without this lateral heating, the magnetic concentration would become dark. Such is the situation for larger magnetic concentrations such as micropores, pores and sunspots. Such large vertical flux concentrations have a sufficiently large radii, that their interiors are effectively shielded from radiative heating from their sidewalls. In the present case, the modification of the temperature structure within the magnetic concentration is such that the temperature at optical depth unity is  $T = 7,000 \text{ K}$  (almost 1,000 K higher than the average surface temperature of the quiet Sun). Consequently, the magnetic concentration has a brightness above the average. Its peak brightness of  $I = 1.6 \langle I_{5000} \rangle$ , however, cannot be maintained indefinitely. At  $t = 14.1 \text{ min}$ , the material within the magnetic concentration is cooling excessively, with a value as negative

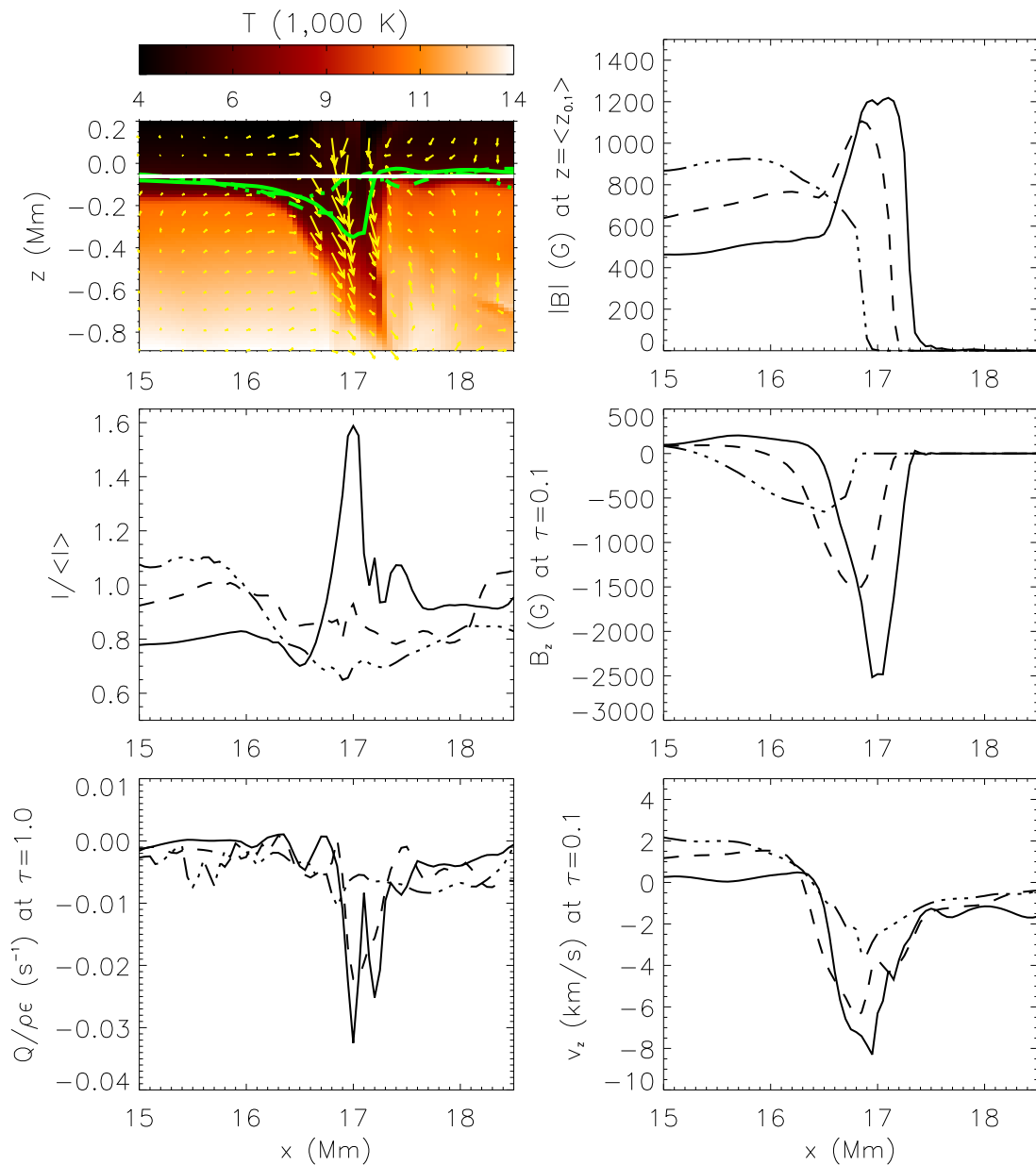


Figure 5.18: Convective intensification of the flux concentration leads to its brightening. Profiles of various quantities are shown for three different times:  $t = 9.8$  min (dash-dotted lines),  $t = 11.8$  min (dashed lines) and  $t = 14.1$  min (solid lines). *Top left*: The colour-coding indicates the temperature structure in and around the magnetic concentration at  $t = 14.1$  min. The green curves in this panel indicate the  $\tau_{5000} = 1$  level for the three different times. The horizontal white line shows the average geometrical height of this optical depth surface in the absence of magnetic fields (i.e.  $z = \langle z_{1.0} \rangle$ ). The overlaid arrows show the components of the velocity field in the  $x$ - $z$  plane at  $t = 14.1$  min. An arrow with a length of one grid-spacing corresponds to a speed of  $10 \text{ km s}^{-1}$ . *Top right*:  $|B|$  at  $\langle z_{0.1} \rangle$ . *Middle left*: Normalized emergent continuum intensity at  $5000 \text{ \AA}$ . *Middle right*:  $B_z$  at  $\tau_{5000} = 0.1$ . *Lower left*: The radiative heating  $Q_{\text{rad}}$  divided by the internal energy density  $\rho\epsilon$ . *Lower right*: Vertical velocity at  $\tau_{5000} = 0.1$ .



as  $Q_{\text{rad}}/\rho\epsilon \approx -0.02 \text{ s}^{-1}$ . If the material in the tube maintains this rate of cooling, then the timescale required for the internal energy to be depleted is, to order of magnitude,  $|Q_{\text{rad}}/\rho\epsilon|^{-1} \sim 1 \text{ min}$ . This estimate is consistent with the simulation result, that within a few minutes of reaching its peak intensity of  $I = 1.6\langle I_{5000} \rangle$ , the magnetic concentration dims to  $I = 1.3\langle I_{5000} \rangle$ . Thereafter, the magnetic flux concentration is in approximate radiative equilibrium with its surroundings ( $Q_{\text{rad}} \sim 0$ ) and its brightness is maintained within the range  $(1.0 - 1.3)\langle I_{5000} \rangle$ .

Let us now turn our attention to the other photospheric footpoint of the arched flux tube. In Fig. 5.17, this feature is located at the l.h.s. of the magnetic complex and has positive polarity. This magnetic concentration also brightens, albeit with a lower peak intensity, and at a later time than its counterpart. At  $t = 14.1 \text{ min}$ , this magnetic concentration is still dark. At  $t = 19.9 \text{ min}$ , its brightness has increased to  $I = 1.3\langle I_{5000} \rangle$ , which is already significantly brighter than non-magnetic downflows. The same physical mechanism that we just described is responsible for the brightening of this magnetic flux concentration.

#### 5.4.2 Detection of an ephemeral region

The results presented thus far have shown us the importance of convection for the morphology of the surface field during and after emergence. When we look at the magnetograms in Fig. 5.17, we do not find a clean bipolar region consisting of two distinct polarities neatly separated from one another. Of course, there is a predominance of positive polarity field in the top-left half of the field-of-view, complemented by mainly negative polarity field in the other half. The detailed morphology of the magnetic region, however, shows a complexity that is the legacy of the interaction between the flux tube and the granular flow.

How do our simulation results compare with observational studies (e.g. Hagenaar 2001) of ephemeral regions? To address this question, we investigate how the appearance of the surface flux following the emergence of an arched flux tube depends on factors such as the spatial resolution and noise level of an instrument. For reference, we use the synthetic magnetograms directly from the simulation, which have pixel sizes of  $50 \times 50 \text{ km}^2$ . Given a reference magnetogram, a degraded magnetogram with lower resolution is produced in two steps. Firstly, the reference magnetogram is convolved with a normalized 2D Gaussian kernel of the form  $K(x, y) \propto \exp[-(x^2 + y^2)/w^2]$ , where  $w$  is the characteristic width of the kernel. In order to avoid the influence of the horizontal periodicity on the convolution integral, the reference magnetogram is bordered with layers of zero-value pixels. Once we have convolved the padded reference magnetogram with the kernel, the resulting array is resampled so that each pixel in the degraded magnetogram has a pixel size of  $(0.5w)^2$ . In other words, the resampling is done so that a resolution element corresponds to  $2 \times 2$  pixels. From hereon, we refer to the value of  $w$  as the effective spatial resolution. To emulate the effect of different levels of noise in the degraded magnetograms, pixels in the resampled magnetogram with absolute values smaller than a specified threshold are set to zero.

Figure 5.19 shows a set of three synthetic magnetograms from the arched flux tube simulation at  $t = 37.7 \text{ min}$ . The top panel is the reference magnetogram directly from the simulation. The middle and bottom panels show the magnetogram degraded to effec-

tive spatial resolutions of 0.8 Mm and 1.6 Mm, respectively. These effective resolutions correspond to pixels sizes of 0.4 Mm and 0.8 Mm, respectively. A common grey scaling applies to all three magnetograms. For the reference magnetogram, the grey scale indicates the actual value of the vertical magnetic field at  $\tau_{5000} = 0.1$ . In the smoothed magnetograms, the grey scale at each pixel indicates the flux density. The flux density has units of  $\text{Mx cm}^{-2}$ , which is formally equivalent to the unit of G. For this figure, we specified a threshold for the flux density to be  $10 \text{ Mx cm}^{-2}$ .

Our choice of effective spatial resolution and threshold is motivated by the instrumental characteristics of the Michelson Doppler Imager (MDI) on board the spacecraft *SOHO*. MDI provides magnetograms in full-disk and in high-resolution mode. Magnetograms in the full-disk mode have a pixel size of  $2''$ , corresponding to 1.45 Mm at the disk centre. The pixel size in high resolution mode is  $0''.61$ , corresponding to about 0.435 Mm at the disk centre. The noise level of individual magnetograms is estimated to be  $14 \text{ Mx cm}^{-2}$  (Scherrer et al. 1995, Hagenaar 2001). If *SOHO* were to observe our simulated flux emergence event in high resolution mode, it would provide a magnetogram similar to the one we synthesized in the middle panel of Fig. 5.19. A magnetogram with a resolution intermediate between MDI full-disk and high resolution mode should appear like the one in the bottom panel of Fig. 5.19.

The effect of increasing the width of the smoothing kernel is the gradual loss of small-scale structure below the resolution limit. As expected, a magnetogram with a spatial resolution of 0.8 (or even 1.6) Mm does not reveal any information about the structuring of the surface flux by the granulation. For example, one is unable to discern that the patch of positive flux centered at  $[x, y] = [6, 6]$  Mm is actually concentrated in the downflow lanes around a single granule. Since the magnetic region has mixed-polarity fields, a decrease in the spatial resolution also leads to an apparent cancellation of flux. For instance, in the reference magnetogram, the flux (above the threshold) of a given polarity integrated over the field-of-view is  $2.0 \times 10^{19} \text{ Mx}$ . The corresponding values of the integrated flux in the middle and lower magnetograms are  $1.5 \times 10^{19} \text{ Mx}$  and  $1.3 \times 10^{19} \text{ Mx}$  respectively. The use of a threshold level introduces imbalances between the integrated flux of opposite signs at levels up to a few percent.

The magnetogram with a resolution of 1.6 Mm in Fig. 5.19 shows two patches of flux of opposite polarity, whose centres are separated by about 9 Mm. In Fig. 5 of her paper, Hagenaar (2001) shows examples of bipolar regions which were identified as ephemeral regions based on her selection criteria. These bipolar regions do not consist of two distinct polarities, each with roughly circular shapes. Instead, the bipolar regions appear somewhat like the one we have in the bottom magnetogram in Fig. 5.19. A time sequence of synthetic magnetograms of the simulated emergence event is shown in Fig. 5.20. In this figure, all the magnetograms have an effective resolution of 1.6 Mm and noise level of  $10 \text{ Mx cm}^{-2}$ . The sequence shows the emergence of a bipolar region at  $t = 9.8$  min. At this time, the two patches of opposite polarity are each elongated roughly in the  $x$ -direction. Between  $t = 9.8$  min and  $t = 37.7$  min, the expansion speed of the outer borders of the bipolar region in the smoothed magnetograms is approximately  $2 \text{ km s}^{-1}$ . This value compares favorably to the expansion speeds of the outer borders of ephemeral regions as measured by Harvey (1993) and by Hagenaar (2001). The two authors report expansion speeds within the ranges  $1 - 3 \text{ km s}^{-1}$  and  $1.4 - 3 \text{ km s}^{-1}$ , respectively.

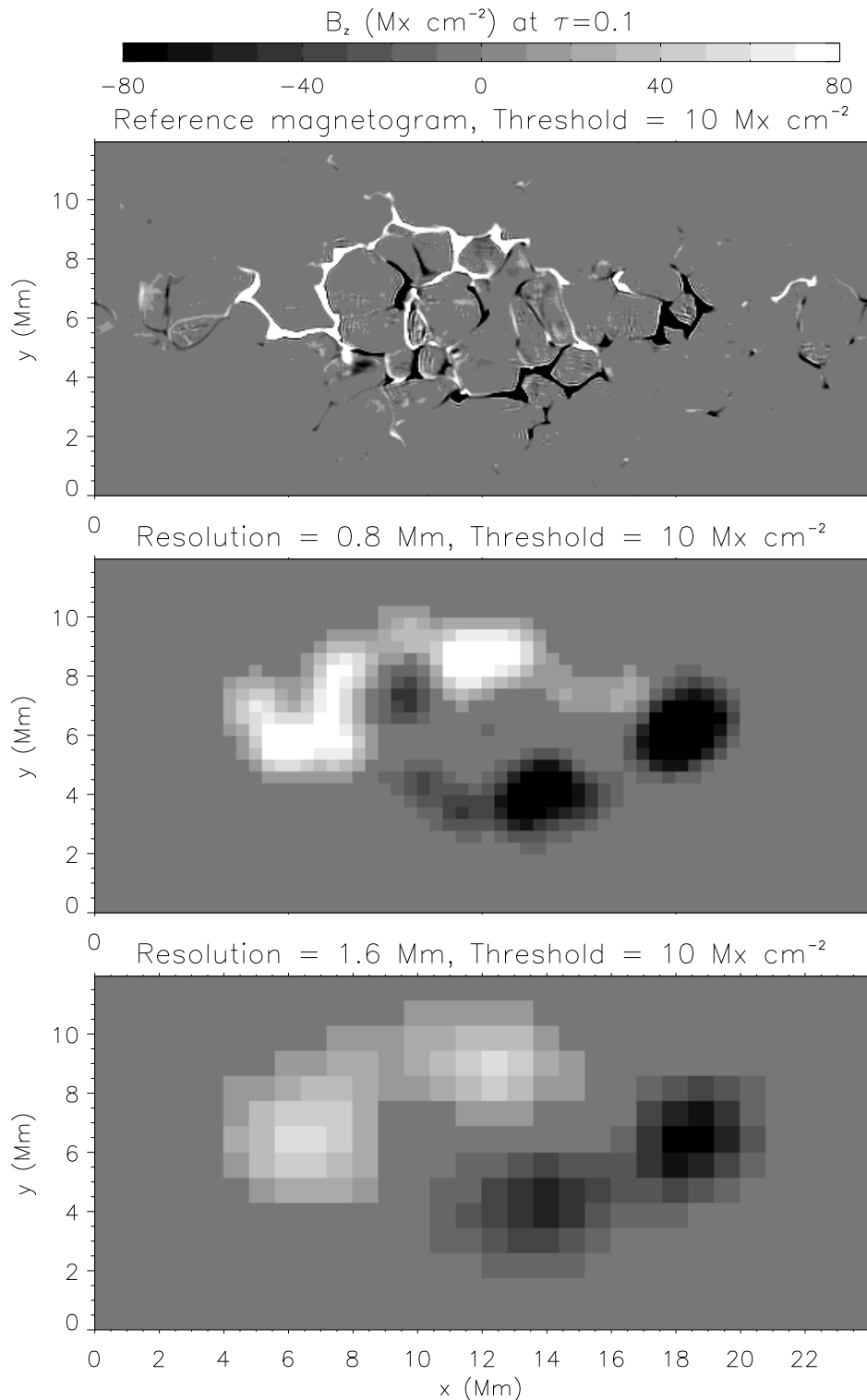


Figure 5.19: Synthetic magnetograms of the surface magnetic field at  $t = 37.7$  min at different effective spatial resolutions. *Top*: Unsmoothed synthetic magnetogram. *Middle*: Magnetogram smoothed to a resolution of  $0.8 \text{ Mm}$ . *Bottom*: Magnetogram smoothed to a resolution of  $1.6 \text{ Mm}$ . The grey scale indicates the flux density in units of  $\text{Mx cm}^{-2}$ .



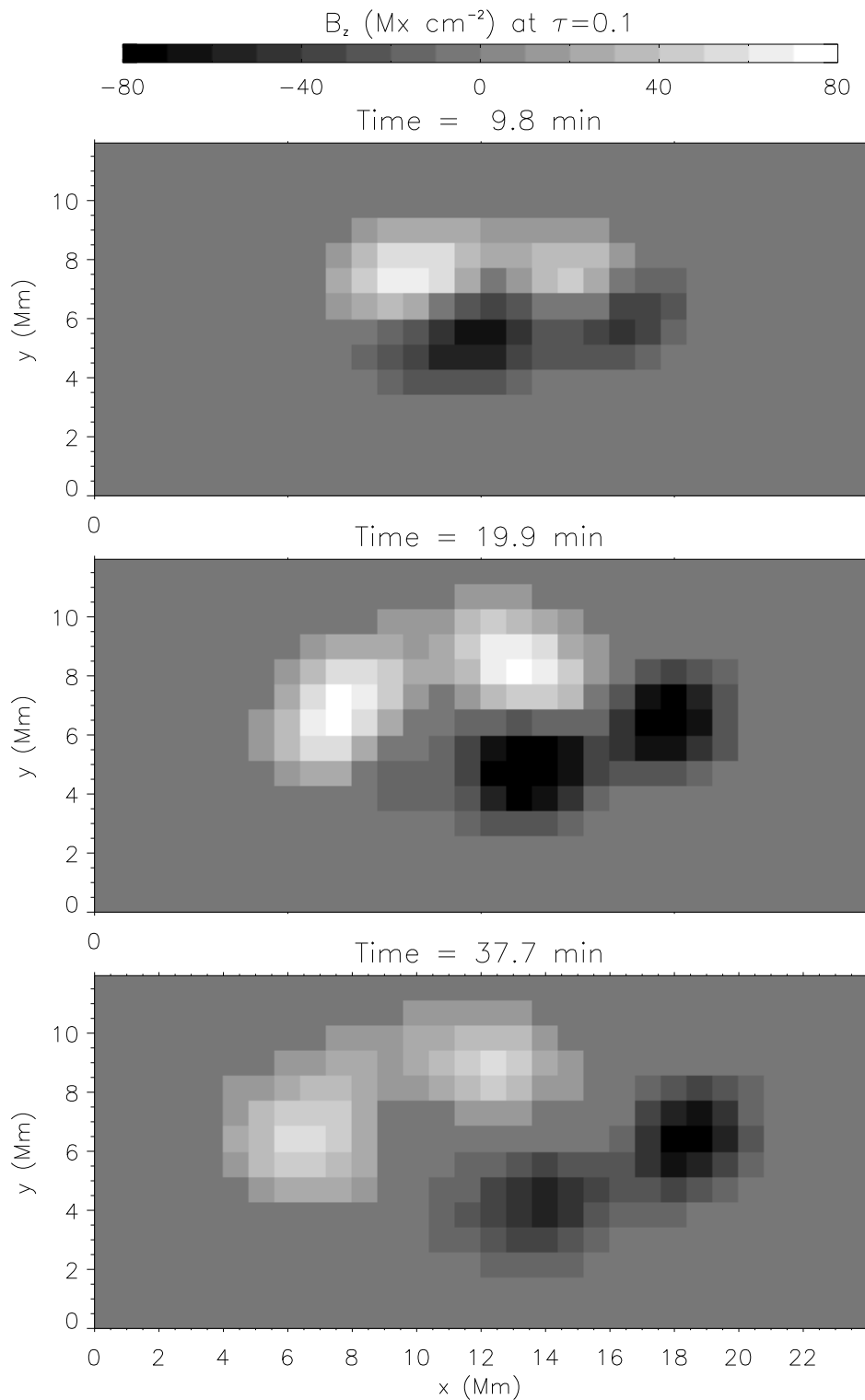


Figure 5.20: Sequence of smoothed synthetic magnetograms with an effective spatial resolution of 1.6 Mm. The threshold used is  $10 \text{ Mx cm}^{-2}$ . The grey scale indicates the flux density in units of  $\text{Mx cm}^{-2}$ .

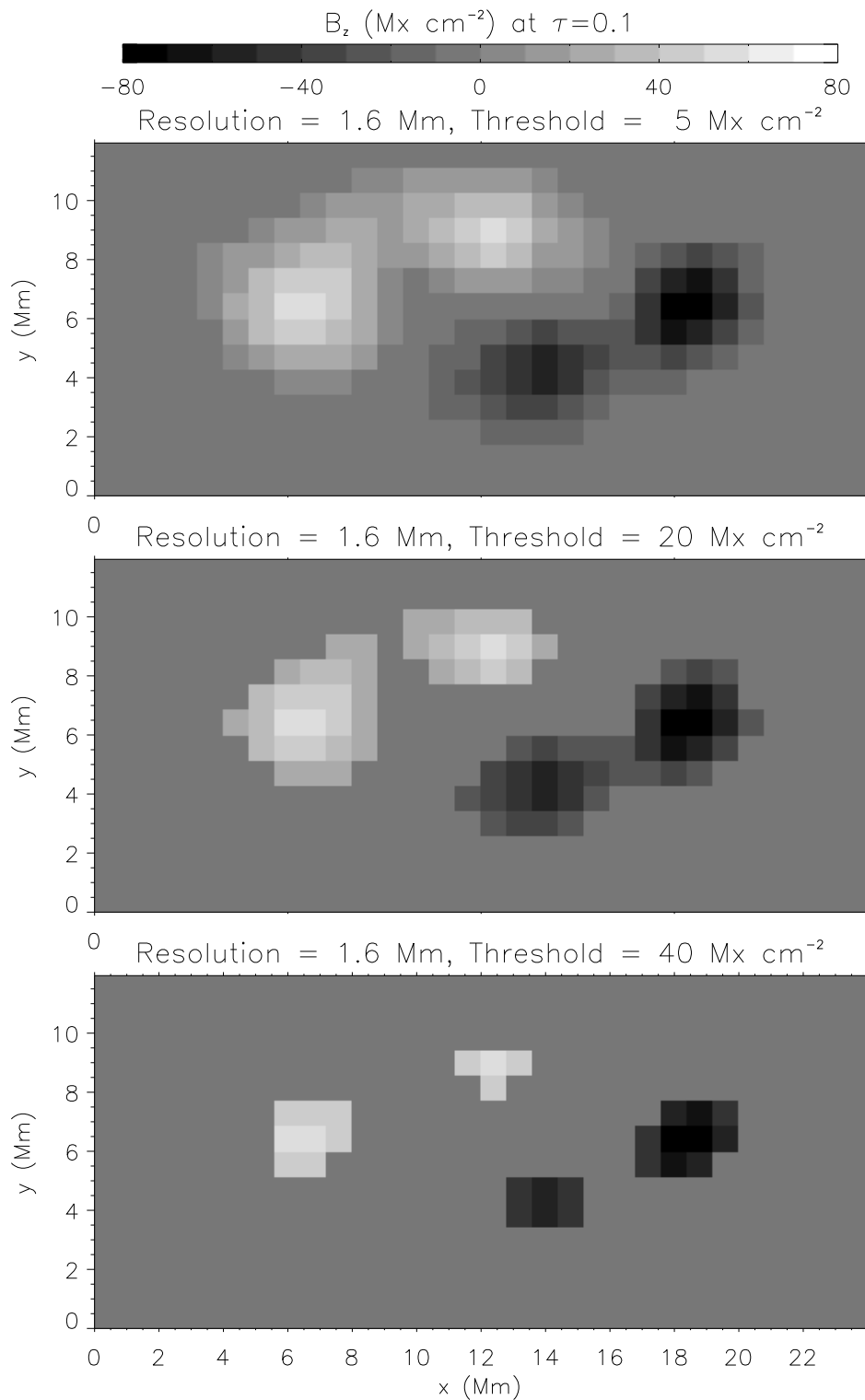


Figure 5.21: Synthetic magnetograms of the surface magnetic field at  $t = 37.7$  min at the same resolution (1.6 Mm) but with different thresholds. The grey scale indicates the flux density in units of  $\text{Mx cm}^{-2}$ .

Depending on the threshold we choose for our smoothed synthetic magnetograms, the magnetic region may appear as one or two bipole pairs. Fig. 5.21 shows synthetic magnetograms with the same effective spatial resolution (1.6 Mm) but for different values of the threshold. For values of the threshold up to  $10 \text{ Mx cm}^{-2}$  (see top panel of Fig. 5.21 and bottom panel of Fig. 5.19), the magnetic regions appear like a single bipole. For a threshold of  $20 \text{ Mx cm}^{-2}$ , there appears to exist two discrete positive polarity regions and one single negative polarity region. As we increase the threshold to  $40 \text{ Mx cm}^{-2}$ , the negative polarity region splits into two, so that we end up with two bipole pairs.

We have produced synthetic magnetograms of our simulation of the emergence of an arched flux tube for various spatial resolutions and for different values of the threshold. We found that, given a sufficiently low spatial resolution, a dispersed patch of flux on the solar surface may appear as an individual flux concentration in the synthetic magnetogram. In the case of our simulation, this effect can smooth out the detailed surface morphology of a magnetic complex consisting of mixed-polarity field, so that the magnetic complex appears like an ephemeral region in low-resolution magnetograms. Given this finding, let us do the following thought experiment. Suppose we identify an ephemeral region in an MDI magnetogram. How may we expect the same ephemeral region to appear given magnetograms of better quality and resolution? What we found out in this section, is that at higher resolution, the apparently discrete magnetic concentrations comprising ephemeral regions may simply be fragments of dispersed, smaller-scale flux concentrations of like polarity. Even in MDI magnetograms, Hagenaar (2001) finds that some ephemeral regions fragment as their outer borders expand. At higher resolution, the fragmentation events will become more readily detectable. The Solar Optical Telescope (SOT) on board the upcoming Solar-B space mission will provide magnetograms with pixel sizes of 60 km, delivering a spatial resolution of about 100 km. This level of resolution will reveal the richness of the morphology of ephemeral region fields at sub-granular scales.



## 6 Concluding remarks

In this dissertation, we studied the dynamics of the buoyant rise of magnetic flux tubes, with a special emphasis on their emergence into the photosphere. The emergence simulations we presented in Chapter 5 are ‘realistic’ in two senses. Firstly, the simulations take into account the effects of non-local radiative energy exchange, partial ionization and magneto-convection, all of which are important for a proper treatment of the problem.

Secondly, the simulations yield observational signatures of magnetic flux emergence that are in qualitative and quantitative agreement with observations of emerging flux regions (EFRs). Due to the limited size of our simulation domain, we are restricted to simulations beginning with individual flux tubes, each carrying a longitudinal magnetic flux of up to  $10^{19}$  Mx. This value is comparable to the longitudinal flux contained in a small ephemeral region, but is a few orders of magnitude smaller than the magnetic flux contained in large active regions. Nevertheless, our emergence simulations captures observational properties pertaining to ephemeral regions as well as to the EFRs of active regions during their development phase. For instance, take our simulation of the emergence of an arched flux tube (see Section 5.4). In Section 5.4.2, we showed that at sufficiently low spatial resolution ( $\sim 1$  Mm), the morphology and evolution of the surface field in the magnetograms of this emergence event are akin to those of ephemeral regions (Hagenaar 2001). In the same simulation, we found distinct observational signatures (e.g. transient darkening coincident with upflows, followed by the bright grains flanking the ends of the darkening) that are observed in EFRs of active regions (see, for example Strous and Zwaan 1999).

The common ground between small ephemeral regions and active regions is the following: An active region does not result from the emergence of a monolithic flux bundle. Instead, the magnetic flux of an active region builds up as the result of the emergence of many smaller flux bundles. The amount of flux contained in each flux bundle is estimated to be about  $10^{19}$  Mx (Born 1974, Brants and Steenbeek 1985). From our simulations, we know that flux tubes a longitudinal flux of  $10^{19}$  Mx are able to disturb the granulation pattern as they emerge. The emergence of such flux tubes leads to conspicuous observational signatures such as dark alignments and bright grains (see Section 5.3.2).

Magnetic flux tubes with less longitudinal flux (say,  $10^{18}$  Mx) are not sufficiently buoyant to rise coherently against the convective flows. The emergence events associated with these smaller and weaker flux tubes are inconspicuous, in the sense that the granulation pattern in the quiet Sun is not disturbed (see Section 5.3.1). The small spatial scales ( $\sim 1$  Mm) and short temporal scales (5 min) of such events make their detection difficult. Although detections of these events have been reported (De Pontieu 2002), it is unknown how much flux emerges at the surface in this form.

In Section 5.3.1.1, we provided an example of the secondary emergence of a bipole.

This bipole (with a flux of  $10^{18}$  Mx in each polarity) is peculiar for two reasons. Firstly, it emerged in a location that is far away from the emergence site of other bipoles. Secondly, it emerged several granulation time scales after the initial appearance of flux at the surface. This secondary emergence event is the result of the recirculation and overturning of material in the near-surface layers of the convection zone. It suggests to us that, at least a fraction of small-scale flux emergence events on the solar surface could result from recirculation of material in the convection zone.

# Bibliography

- Acheson, D. J.: 1979, *Sol. Phys.* **62**, 23
- Archontis, V., Moreno-Insertis, F., Galsgaard, K., Hood, A., and O'Shea, E.: 2004, *ApJ* **441**, 886
- ASCI Center for Thermonuclear Flashes,: 2003, *FLASH2.3 User Manual*
- Balthasar, H., Grosser, H., Schroeter, C., and Wiehr, E.: 1990, *A&A* **235**, 437
- Batchelor, G.: 1967, *An Introduction to Fluid Dynamics*, Cambridge: Cambridge University Press
- Baumann, I., Schmitt, D., Schüssler, M., and Solanki, S. K.: 2004, *A&A* **426**, 1075
- Bercik, D. J., Nordlund, A., and Stein, R. F.: 2003, in *ESA SP-517: GONG+ 2002. Local and Global Helioseismology: the Present and Future*, pp 201–206
- Born, R.: 1974, *Sol. Phys.* **38**, 127
- Brants, J. J. and Steenbeek, J. C. M.: 1985, *Sol. Phys.* **96**, 229
- Bray, R. J., Loughhead, R. E., and Durrant, C. J.: 1984, *The solar granulation (2nd edition)*, Cambridge and New York, Cambridge University Press, 1984, 270 p.
- Caligari, P., Moreno-Insertis, F., and Schüssler, M.: 1995, *ApJ* **441**, 886
- Cattaneo, F., Emonet, T., and Weiss, N.: 2003, *ApJ* **588**, 1183
- Chandrasekhar, S.: 1957, *An introduction to the study of stellar structure.*, [New York] Dover Publications [1957]
- Charbonneau, P.: 2005, *Living Reviews in Solar Physics* **2**, 2
- De Pontieu, B.: 2002, *ApJ* **569**, 474
- Domínguez Cerdeña, I., Sánchez Almeida, J., and Kneer, F.: 2003, *A&A* **407**, 741
- D'Silva, S. Z. and Choudhuri, A. R.: 1991, *Sol. Phys.* **136**, 201
- Eddy, J. A.: 1976, *Science* **192**, 1189
- Emonet, T. and Moreno-Insertis, F.: 1998, *ApJ* **492**, 804



- Emonet, T., Moreno-Insertis, F., and Rast, M. P.: 2001, *ApJ* **549**, 1212
- Espagnet, O., Muller, R., Roudier, T., Mein, N., and Mein, P.: 1995, *A&AS* **109**, 79
- Evans, J. W. and Catalano, C. P.: 1972, *Sol. Phys.* **27**, 299
- Fan, Y.: 2004, *Living Rev. Solar Phys.* **1**, 1
- Fan, Y., Abbett, W. P., and Fisher, G. H.: 2003, *ApJ* **582**, 1206
- Fan, Y., Fisher, G. H., and Deluca, E. E.: 1993, *ApJ* **405**, 390
- Fan, Y., Fisher, G. H., and McClymont, A. N.: 1994, *ApJ* **436**, 907
- Fan, Y., Zweibel, E. G., and Lantz, S. R.: 1998a, *ApJ* **493**, 480
- Fan, Y., Zweibel, E. G., Linton, M. G., and Fisher, G. H.: 1998b, *ApJ* **505**, L59+
- Ferriz-Mas, A., Schüssler, M., and Anton, V.: 1989, *A&A* **210**, 425
- Forbes, T. G. and Priest, E. R.: 1984, *Sol. Phys.* **94**, 315
- Granzer, T., Schüssler, M., Caligari, P., and Strassmeier, K. G.: 2000, *A&A* **355**, 1087
- Grossmann-Doerth, U., Schuessler, M., and Steiner, O.: 1998, *A&A* **337**, 928
- Hagenaar, H. J.: 2001, *ApJ* **555**, 448
- Hagenaar, H. J., Schrijver, C. J., and Title, A. M.: 2003, *ApJ* **584**, 1107
- Hale, G. E.: 1908, *ApJ* **28**, 315
- Hale, G. E., Ellerman, F., Nicholson, S. B., and Joy, A. H.: 1919, *ApJ* **49**, 153
- Harvey, K. L.: 1993, *Ph.D. Thesis*
- Hirsch, C.: 1990a, *Numerical computation of internal and external flows. Vol. 1 - Fundamentals of Numerical Discretization*, Chichester, England and New York, John Wiley & Sons
- Hirsch, C.: 1990b, *Numerical computation of internal and external flows. Vol. 2 - Computational methods for inviscid and viscous flows*, Chichester, England and New York, John Wiley & Sons
- Holzwarth, V. and Schüssler, M.: 2003a, *A&A* **405**, 291
- Holzwarth, V. and Schüssler, M.: 2003b, *A&A* **405**, 303
- Hughes, D. W. and Falle, S. A. E. G.: 1998, *ApJ* **509**, L57
- Hurlburt, N. E. and Toomre, J.: 1988, *ApJ* **327**, 920
- Isobe, H., Miyagoshi, T., Shibata, K., and Yokoyama, T.: 2005, *Nature* **434**, 478

- Kippenhahn, R. and Weigert, A.: 1994, *Stellar Structure and Evolution*, Stellar Structure and Evolution, XVI, 468 pp. 192 figs.. Springer-Verlag Berlin Heidelberg New York. Also Astronomy and Astrophysics Library
- Komm, R., Mattig, W., and Nesis, A.: 1991, *A&A* **252**, 812
- Kubo, M., Shimizu, T., and Lites, B. W.: 2003, *ApJ* **595**, 465
- Kucera, A., Rybak, J., and Woehl, H.: 1995, *A&A* **298**, 917
- Landau, L. D. and Lifshitz, E. M.: 1980, *Statistical physics. Pt.1, Pt.2*, Course of theoretical physics, Pergamon International Library of Science, Technology, Engineering and Social Studies, Oxford: Pergamon Press, 1980|c1980, 3rd rev.and enlarg. ed.
- Leenaarts, J. and Wedemeyer-Böhm, S.: 2005, *A&A* **431**, 687
- Leighton, R. B.: 1964, *ApJ* **140**, 1547
- Leighton, R. B., Noyes, R. W., and Simon, G. W.: 1962, *ApJ* **135**, 474
- Linton, M. G., Longcope, D. W., and Fisher, G. H.: 1996, *ApJ* **469**, 954
- Lites, B. W., Leka, K. D., Skumanich, A., Martinez Pillet, V., and Shimizu, T.: 1996, *ApJ* **460**, 1019
- Lites, B. W., Skumanich, A., and Martinez Pillet, V.: 1998, *A&A* **333**, 1053
- Longcope, D., Fisher, G., and Arendt, S.: 1996, *ApJ* **464**, 999
- Magara, T.: 2001, *ApJ* **549**, 608
- Maunder, E. W.: 1922, *MNRAS* **82**, 534
- Moreno-Insertis, F., Caligari, P., and Schüssler, M.: 1994, *Sol. Phys.* **153**, 449
- Moreno-Insertis, F. and Emonet, T.: 1996, *ApJ* **472**, L53
- Parker, E. N.: 1955, *ApJ* **121**, 491
- Parker, E. N.: 1974, *ApJ* **191**, 245
- Parker, E. N.: 1975, *ApJ* **198**, 205
- Parker, E. N.: 1979, *Cosmical magnetic fields: Their origin and their activity*, Oxford, Clarendon Press; New York, Oxford University Press, 1979, 858 p.
- Petrovay, K., Marik, M., Brown, J. C., Fletcher, L., and van Driel-Gesztelyi, L.: 1990, *Sol. Phys.* **127**, 51
- Proctor, M. R. E. and Weiss, N. O.: 1982, *Reports of Progress in Physics* **45**, 1317
- Rast, M. P., Nordlund, A., Stein, R. F., and Toomre, J.: 1993, *ApJ* **408**, L53

- Rast, M. P. and Toomre, J.: 1993a, *ApJ* **419**, 224
- Rast, M. P. and Toomre, J.: 1993b, *ApJ* **419**, 240
- Roberts, B. and Webb, A. R.: 1978, *Sol. Phys.* **56**, 5
- Robinson, F. J., Demarque, P., Li, L. H., Sofia, S., Kim, Y.-C., Chan, K. L., and Guenther, D. B.: 2003, *MNRAS* **340**, 923
- Rutten, R. J., de Wijn, A. G., and Sütterlin, P.: 2004, *A&A* **416**, 333
- Scherrer, P. H., Bogart, R. S., Bush, R. I., Hoeksema, J. T., Kosovichev, A. G., Schou, J., Rosenberg, W., Springer, L., Tarbell, T. D., Title, A., Wolfson, C. J., Zayer, I., and MDI Engineering Team: 1995, *Sol. Phys.* **162**, 129
- Schmitt, D., Schuessler, M., and Ferriz-Mas, A.: 1996, *A&A* **311**, L1
- Schrijver, C. J., DeRosa, M. L., and Title, A. M.: 2003, *ApJ* **590**, 493
- Schrijver, C. J. and Title, A. M.: 2001, *ApJ* **551**, 1099
- Schüssler, M.: 1979, *A&A* **71**, 79
- Schüssler, M.: 1990, in *IAU Symposium*, p. 161
- Schüssler, M., Caligari, P., Ferriz-Mas, A., and Moreno-Insertis, F.: 1994, *A&A* **281**, L69
- Schüssler, M., Caligari, P., Ferriz-Mas, A., Solanki, S. K., and Stix, M.: 1996, *A&A* **314**, 503
- Schüssler, M. and Rempel, M.: 2005, *A&A* **441**, 337
- Schwabe, H.: 1843, *Astron. Nachr.* **20**, 495
- Sheeley, N. R.: 2005, *Living Reviews in Solar Physics* **2**, 5
- Shibata, K., Tajima, T., Steinolfson, R. S., and Matsumoto, R.: 1989, *ApJ* **345**, 584
- Solanki, S. K., Zufferey, D., Lin, H., Rueddi, I., and Kuhn, J. R.: 1996, *A&A* **310**, L33
- Spörer, P.: 1890, *MNRAS* **50**, 251
- Spruit, H. C.: 1974, *Sol. Phys.* **34**, 277
- Spruit, H. C.: 1981, *A&A* **98**, 155
- Spruit, H. C., Nordlund, A., and Title, A. M.: 1990, *ARA&A* **28**, 263
- Steffen, M., Ludwig, H.-G., and Kruess, A.: 1989, *A&A* **213**, 371
- Stein, R. F. and Nordlund, A.: 1989, *ApJ* **342**, L95
- Stein, R. F. and Nordlund, A.: 1998, *ApJ* **499**, 914

- Strous, L. H. and Zwaan, C.: 1999, *ApJ* **527**, 435
- Suemoto, Z., Hiei, E., and Nakagomi, Y.: 1987, *Sol. Phys.* **112**, 59
- Suemoto, Z., Hiei, E., and Nakagomi, Y.: 1990, *Sol. Phys.* **127**, 11
- Title, A. M., Tarbell, T. D., Topka, K. P., Ferguson, S. H., Shine, R. A., and SOUP Team: 1989, *ApJ* **336**, 475
- Toro, E. L.: 1997, *Riemann Solvers and Numerical Methods for Fluid Dynamics*, Springer-Verlag Berlin Heidelberg
- van Driel-Gesztelyi, L. and Petrovay, K.: 1990, *Sol. Phys.* **126**, 285
- Venkatakrishnan, P.: 1986, *Nature* **322**, 156
- Vögler, A.: 2003, *Three-dimensional simulations of magneto-convection in the solar photosphere*, Göttingen University, <http://webdoc.sub.gwdg.de/diss/2004/voegler/index.html>
- Vögler, A.: 2004, *A&A* **421**, 755
- Vögler, A., Shelyag, S., Schüssler, M., Cattaneo, F., Emonet, T., and Linde, T.: 2005, *A&A* **429**, 335
- Weiss, N. O.: 1966, *Royal Society of London Proceedings Series A* **293**, 310
- Zirin, H.: 1972, *Sol. Phys.* **22**, 34
- Zwaan, C.: 1978, *Sol. Phys.* **60**, 213
- Zwaan, C.: 1985, *Sol. Phys.* **100**, 397
- Zwaan, C.: 1987, *ARA&A* **25**, 83



# A Calculation of important thermodynamic quantities

In this Appendix, we explain how important thermodynamic quantities such as the specific entropy  $s$ , the specific heats ( $c_p$  and  $c_v$ ), the adiabatic temperature gradient  $\nabla_{\text{ad}}$  etc. can be calculated when the Equation of State (EOS) is given in the form  $T(\rho, \epsilon)$  and  $p(\rho, \epsilon)$ <sup>1</sup>.

## A.1 Specific entropy

The specific entropy  $s$  is a thermodynamic state function. Its differential is defined as

$$ds := \frac{dq}{T}. \quad (\text{A.1})$$

Using the 1st law of thermodynamics, we can write

$$ds = \frac{1}{T} \left[ d\epsilon + pd\left(\frac{1}{\rho}\right) \right]. \quad (\text{A.2})$$

Since we have the EOS in the form of look-up tables  $p(\rho, \epsilon)$  and  $T(\rho, \epsilon)$ , we can at once integrate Eq. (A.2) to evaluate the look-up table  $s = s(\rho, \epsilon)$ . The integration gives an arbitrary constant  $s_0$ . The value of this offset is not particularly important for our purposes since we are only interested in changes in  $s$ . For the work presented in this dissertation, we set  $s_0 = 0$  for  $\epsilon_0 = 2.0 \times 10^{11}$  erg g<sup>-1</sup> and  $\rho_0 = 1.0 \times 10^{-9}$  g cm<sup>-3</sup>.

## A.2 The Jacobian matrix

In terms of the independent thermodynamic variables density  $\rho$  and  $\epsilon$ , differential changes in temperature and pressure can be expressed as

$$\begin{pmatrix} dT \\ dp \end{pmatrix} = J \begin{pmatrix} d\rho \\ d\epsilon \end{pmatrix},$$

where

$$J = \begin{pmatrix} J_a & J_b \\ J_c & J_d \end{pmatrix} = \begin{pmatrix} \left(\frac{\partial T}{\partial \rho}\right)_\epsilon & \left(\frac{\partial T}{\partial \epsilon}\right)_\rho \\ \left(\frac{\partial p}{\partial \rho}\right)_\epsilon & \left(\frac{\partial p}{\partial \epsilon}\right)_\rho \end{pmatrix}$$

---

<sup>1</sup>These were the look-up tables used by Vögler et al. (2005)

is the Jacobian matrix (cf Landau and Lifshitz (1980)). On the other hand, we can write differential changes in  $\epsilon$  and  $\rho$  in terms of  $dT$  and  $dp$  by inverting  $J$ . Let us define  $K = J^{-1}$ , so that:

$$\begin{pmatrix} d\rho \\ d\epsilon \end{pmatrix} = K \begin{pmatrix} dT \\ dp \end{pmatrix},$$

where

$$\begin{aligned} K &= \begin{pmatrix} K_a & K_b \\ K_c & K_d \end{pmatrix} = \frac{1}{\det(J)} \begin{pmatrix} J_d & -J_b \\ -J_c & J_a \end{pmatrix} \\ &= \begin{pmatrix} \left(\frac{\partial\rho}{\partial T}\right)_p & \left(\frac{\partial\rho}{\partial p}\right)_T \\ \left(\frac{\partial\epsilon}{\partial T}\right)_p & \left(\frac{\partial\epsilon}{\partial p}\right)_T \end{pmatrix} \end{aligned}$$

Since  $J$  can be easily calculated from the look-up tables  $p(\epsilon, \rho)$  and  $T(\epsilon, \rho)$ , we can calculate the mixed derivatives in  $K$  without needing  $\epsilon(T, p)$  and  $\rho(T, p)$ <sup>2</sup>. In the following, expressions for the specific heats and adiabatic temperature gradient in terms of the basic thermodynamic variables ( $\epsilon, \rho, p$  and  $T$ ) and components of  $K$  are derived.

### A.3 Specific heats $c_v$ and $c_p$

In constant volume processes, the heat change in the system is equal to the change in specific internal energy. Thus:

$$c_v := \left(\frac{dq}{dT}\right)_\rho \tag{A.3}$$

$$= \left(\frac{\partial\epsilon}{\partial T}\right)_\rho, \tag{A.4}$$

$$= J_b^{-1} \tag{A.5}$$

$$= K_c + K_a \frac{J_a}{J_b}. \tag{A.6}$$

In constant pressure processes, the heat change in the system is equal to the change in enthalpy  $h = \epsilon + p/\rho$ . Thus, we can write  $c_p$  in the following way:

$$c_p := \left(\frac{dq}{dT}\right)_p, \tag{A.7}$$

$$= \left(\frac{\partial h}{\partial T}\right)_p, \tag{A.8}$$

$$= K_c - \frac{p}{\rho^2} K_a. \tag{A.9}$$

---

<sup>2</sup>Note that like  $J$ ,  $K$  is a Jacobian matrix, but for the inverse transformation. Since the EOS is smooth and well-behaved, we do not need to worry that  $J$  maybe singular.



## A.4 Adiabatic temperature gradient

To derive an expression for the adiabatic temperature gradient  $\nabla_{\text{ad}}$ , let us consider Eq. (A.2). Since  $\epsilon(T, p)$  and  $\rho(T, p)$  are functions of temperature and pressure, we can express  $d\epsilon$  and  $d\rho$  in terms of  $dT$  and  $dp$ , which yields:

$$ds = c_p d \ln T - \frac{p}{T} \left[ \frac{p}{\rho^2} K_b - K_d \right] d \ln p, \quad (\text{A.10})$$

where we have made use of Eq. (A.8). Setting  $ds = 0$ , we obtain the following expression for  $\nabla_{\text{ad}}$ :

$$\nabla_{\text{ad}} := \left( \frac{\partial \ln T}{\partial \ln p} \right)_s, \quad (\text{A.11})$$

$$= \frac{p}{c_p T} \left[ \frac{p}{\rho^2} K_b - K_d \right]. \quad (\text{A.12})$$

## A.5 Chandrasekhar's adiabatic exponents

Chandrasekhar's adiabatic exponents (Chandrasekhar 1957) are defined as

$$\gamma_1 := \left( \frac{\partial \ln p}{\partial \ln \rho} \right)_s, \quad (\text{A.13})$$

$$\gamma_2 := \left( 1 - \left[ \frac{\partial \ln T}{\partial \ln p} \right]_s \right)^{-1}, \quad (\text{A.14})$$

$$\gamma_3 := 1 + \left( \frac{\partial \ln T}{\partial \ln \rho} \right)_s. \quad (\text{A.15})$$

They satisfy the relation

$$\frac{\gamma_1}{\gamma_3 - 1} = \frac{\gamma_2}{\gamma_2 - 1}. \quad (\text{A.16})$$

The second adiabatic exponent is  $\gamma_2 = (1 - \nabla_{\text{ad}})^{-1}$ . Since we have already shown how to calculate  $\nabla_{\text{ad}}$ , calculating  $\gamma_2$  is trivial. The first adiabatic exponent gives the response of pressure to change in density in isentropic expansion/compression. It is a useful quantity because sound waves consisting of adiabatic perturbations propagate through the medium with a speed

$$c_s = \sqrt{\frac{\gamma_1 p}{\rho}}. \quad (\text{A.17})$$

To calculate this quantity, we follow the strategy of § A.2 and make use of inversions of the Jacobian matrix. Here, we use  $\rho$  and  $\epsilon$  as the fundamental thermodynamic variables. The differentials of specific entropy and pressure are given by

$$\begin{pmatrix} ds \\ dp \end{pmatrix} = L \begin{pmatrix} d\rho \\ d\epsilon \end{pmatrix},$$

where

$$L = \begin{pmatrix} L_a & L_b \\ L_c & L_d \end{pmatrix} = \begin{pmatrix} \left( \frac{\partial s}{\partial \rho} \right)_\epsilon & \left( \frac{\partial s}{\partial \epsilon} \right)_\rho \\ \left( \frac{\partial p}{\partial \rho} \right)_\epsilon & \left( \frac{\partial p}{\partial \epsilon} \right)_\rho \end{pmatrix}.$$

Let  $M = L^{-1}$  be the inverse of the Jacobian matrix  $L$ . Then

$$M = \begin{pmatrix} M_a & M_b \\ M_c & M_d \end{pmatrix} = \frac{1}{\det(L)} \begin{pmatrix} L_d & -L_b \\ -L_c & L_a \end{pmatrix}$$

$$= \begin{pmatrix} \left(\frac{\partial \rho}{\partial s}\right)_p & \left(\frac{\partial \rho}{\partial p}\right)_s \\ \left(\frac{\partial \epsilon}{\partial s}\right)_p & \left(\frac{\partial \epsilon}{\partial p}\right)_s \end{pmatrix}.$$

Given that we have the functions  $s = s(\rho, \epsilon)$  and  $p = p(\rho, \epsilon)$ , we can calculate  $M$ . By the definition of  $\gamma_1$ , we have

$$\gamma_1 = \frac{\rho}{pM_b}. \quad (\text{A.18})$$

One can use Eqn. (A.16) to calculate  $\gamma_3$ . Alternatively, one can express the differentials  $ds$  and  $dT$  in terms of  $d\epsilon$  and  $d\rho$  and the relevant partial derivatives, and then invert the resulting Jacobian matrix to find  $\gamma_3$ .

## B Diffusion of a magnetic structure with a Gaussian profile

In the absence of motion and for constant magnetic diffusivity  $\eta$ , the Induction Equation (3.1) reduces to

$$\frac{\partial \mathbf{B}}{\partial t} = -\eta \nabla \times \nabla \times \mathbf{B}, \quad (\text{B.1})$$

$$= \eta \nabla^2 \mathbf{B}, \quad (\text{B.2})$$

where  $\nabla^2$  is the Laplacian operator. This equation establishes the fact that the diffusion of each of the cartesian components of  $\mathbf{B}$  is decoupled from the other two components. In other words, we have a scalar diffusion equation for each cartesian component.

Consider a magnetic flux tube with the longitudinal component of the magnetic field described by the Gaussian profile

$$B_l(r, t = 0) = B_0 e^{-\frac{r^2}{R_0^2}}. \quad (\text{B.3})$$

The diffusion of the longitudinal component is not influenced by the transverse components of the field. We seek a self-similar solution of the form:

$$B_l(r, t) = \frac{\Phi_0}{\pi R(t)^2} e^{-\frac{r^2}{R(t)^2}}, \quad (\text{B.4})$$

where  $\Phi_0 = \int_0^\infty \int_0^{2\pi} B_l(r, 0) r d\theta dr = \pi R_0^2 B_0$  is the longitudinal flux of the tube. Substitution of (B.4) into Eq. (B.2) yields the simple ordinary differential equation for  $R(t)$

$$R \frac{dR}{dt} = 2\eta, \quad (\text{B.5})$$

which has the solution

$$R(t) = \sqrt{4\eta t + R_0^2}. \quad (\text{B.6})$$

The field strength at core of the flux tube ( $r = 0$ ) follows

$$\frac{B_l(r = 0, t)}{B_0} = \frac{1}{1 + \frac{4\eta t}{R_0^2}}. \quad (\text{B.7})$$

This equation describes the weakening field strength due to diffusion. In order for diffusive effects *not* to weaken the tube significantly within a specified time interval  $\tau$ , we

require that

$$\frac{B_0 - B_l(r = 0, t = \tau)}{B_0} \ll 1 \quad (\text{B.8})$$

$$\rightarrow \eta \ll \frac{R_0^2}{4\tau}. \quad (\text{B.9})$$

# C Magnetic field extrapolation

In the study of solar magnetic fields, one is often restricted to measurements of the vertical component of the field on the solar surface. However, one would like to know how the magnetic field is structured in the chromosphere or corona. By assuming that the magnetic field above the surface is potential or force-free, one can extrapolate the field to the higher layers of the atmosphere.

## C.1 Potential field

Consider the vertical component of the magnetic field distributed over the plane  $z = 0$ . We assume that the field distribution is periodic in the  $x$  and  $y$  directions with periods  $L_x$  and  $L_y$ , respectively. If we assume that the magnetic field at and above the surface ( $z \geq 0$ ) is potential, we can write

$$\mathbf{B}(x, y, z) = -\nabla\Phi \quad (\text{C.1})$$

where  $\Phi$  is a scalar potential. To find  $\Phi$ , we take the divergence of the previous equation:

$$\nabla^2\Phi = 0, \quad (\text{C.2})$$

and solve it subject to the boundary conditions

$$-\frac{\partial\Phi}{\partial z} = B_z(x, y, z = 0). \quad (\text{C.3})$$

and  $\mathbf{B} \rightarrow 0$  as  $z \rightarrow \infty$ . Since the magnetic field is periodic in the horizontal directions, we use Fourier transforms to solve this problem. Let

$$F(k_x, k_y) = \mathcal{FT}\{f(x, y)\} \quad (\text{C.4})$$

$$= \int \int f(x, y)e^{-i(k_x x + k_y y)} dx dy \quad (\text{C.5})$$

denote the two-dimensional Fourier transform of the spatial function  $f(x, y)$ . Inverse Fourier transforms are denoted by the symbol  $\mathcal{FT}^{-1}$ .

Let us make the following Ansatz for the scalar potential  $\Phi$ :

$$\Phi(x, y, z) = \mathcal{FT}^{-1}\left\{\frac{A(k_x, k_y)}{|k|}e^{-|k|z}\right\}, \quad (\text{C.6})$$

where  $A(k_x, k_y)$  is a function over Fourier-space  $(k_x, k_y)$  and  $|k| = \sqrt{k_x^2 + k_y^2}$  the wavenumber. Applying boundary condition (C.3), we obtain

$$A(k_x, k_y) = \mathcal{FT}\{B_z(x, y, z = 0)\}, \quad (\text{C.7})$$

and therefore

$$\Phi(x, y, z) = \mathcal{FT}^{-1} \left\{ \frac{\mathcal{FT}\{B_z(x, y, z=0)\}}{|k|} e^{-|k|z} \right\}. \quad (\text{C.8})$$

We don't actually need to evaluate  $\Phi$  to calculate the magnetic field components. Substitution of (C.8) into (C.1) gives

$$B_x(x, y, z) = \mathcal{FT}^{-1} \left\{ \mathcal{FT}\{B_z(x, y, z=0)\} \frac{-ik_x}{|k|} e^{-|k|z} \right\}, \quad (\text{C.9})$$

$$B_y(x, y, z) = \mathcal{FT}^{-1} \left\{ \mathcal{FT}\{B_z(x, y, z=0)\} \frac{-ik_y}{|k|} e^{-|k|z} \right\}, \quad (\text{C.10})$$

$$B_z(x, y, z) = \mathcal{FT}^{-1} \left\{ \mathcal{FT}\{B_z(x, y, z=0)\} e^{-|k|z} \right\}. \quad (\text{C.11})$$

The factor  $e^{-|k|z}$  in these equations tells us that small-scale features in the surface field are smoothed out with increasing height.

## C.2 Linear force-free field

A force-free field is one such that the Lorentz force  $\mathbf{j} \times \mathbf{B}/c$  vanishes. A potential magnetic field configuration is an example of a force-free field. *Linear force-free fields* are magnetic field configurations satisfying the condition:

$$\nabla \times \mathbf{B} = \alpha \mathbf{B}, \quad (\text{C.12})$$

where  $\alpha$  is constant. As such, linear force-free fields are also called constant- $\alpha$  fields in the literature. Given the appropriate boundary conditions on a boundary  $\partial R$  enclosing the volume  $R$ , one can solve for the force-free field enclosed in the volume. In the same manner as section C.1, suppose we are given a vertical field  $B_z(x, y, z=0)$  distribution over the  $x$ - $y$  plane. This field is periodic in both horizontal directions with periods  $L_x$  and  $L_y$ . Furthermore,  $\mathbf{B} \rightarrow 0$  as  $z \rightarrow \infty$ .

Now we make the following Ansatz for the solution:

$$B_n(x, y, z) = \mathcal{FT}^{-1} \left\{ A_n(k_x, k_y) e^{-|k|z} \right\}, \quad (\text{C.13})$$

where

$$A_n(k_x, k_y) = \mathcal{FT}\{B_n(x, y, z=0)\}. \quad (\text{C.14})$$

For the moment, we do not specify the exact form of  $|k|$ . Since  $B_z(x, y, z=0)$  is given as a boundary condition,  $A_z(k_x, k_y)$  is known. So our goal is to solve for  $A_x$  and  $A_y$  such that the field given by Eq. (C.13) satisfies the linear force-free condition. Substitution of Eq. (C.13) into Eq. (C.12) gives:

$$\epsilon_{srn} A_n \frac{\partial}{\partial x_r} \left[ e^{i(k_x x + k_y y) - |k|z} \right] = \alpha A_s e^{i(k_x x + k_y y) - |k|z}, \quad (\text{C.15})$$

where  $\epsilon_{srn}$  is the Levi-Civita symbol. Writing out the three equations explicitly, we have:

$$\begin{pmatrix} \alpha & -|k| & -ik_y \\ |k| & \alpha & ik_x \\ ik_y & -ik_x & \alpha \end{pmatrix} \begin{pmatrix} A_x \\ A_y \\ A_z \end{pmatrix} = \begin{pmatrix} 0 \\ 0 \\ 0 \end{pmatrix} \quad (\text{C.16})$$

Eq. (C.16) is a system of three linear equations in two unknowns (since  $A_z$  is an imposed boundary condition). In order for this system of equations to be consistent, the determinant of the matrix must be zero. This is equivalent to the constraint

$$|k|^2 = k_x^2 + k_y^2 - \alpha^2. \quad (\text{C.17})$$

For a decaying solution (i.e.  $\mathbf{B} \rightarrow 0$  as  $z \rightarrow \infty$ ), we require that  $|k|$  be real and non-negative for all possible values of  $k_x$  and  $k_y$ . This restricts the solution space to values of  $\alpha$  satisfying  $\alpha^2 \leq \min\{L_x^{-2}, L_y^{-2}\}$ . Another restriction is that the net vertical flux through the plane  $z = 0$  be zero (i.e.  $A_z = 0$  for  $k_x = k_y = 0$ ). The solution to the problem is

$$A_x = \frac{-i(|k|k_x - \alpha k_y)}{k_x^2 + k_y^2} A_z, \quad (\text{C.18})$$

$$A_y = \frac{-i(|k|k_y + \alpha k_x)}{k_x^2 + k_y^2} A_z. \quad (\text{C.19})$$

For the case  $\alpha = 0$ , we obtain the potential field solution.





# Publications

## Publications in refereed scientific journals

- M. C. M. Cheung, F. Moreno-Insertis & M. Schüssler, “Moving magnetic tubes: fragmentation, vortex streets and the limit of the approximation of thin flux tubes”, *Astronomy & Astrophysics*, in press.
- J. L. Caswell, N. M. McClure-Griffiths, N. M. & Cheung, M. C. M., “Supernova remnant G292.2-0.5, its pulsar, and the Galactic magnetic field”, *Monthly Notices of the Royal Astronomical Society*, Volume 352, Issue 4, pp. 1405-1412.

## Contributed papers in conference proceedings

- M. C. M. Cheung, M. Schüssler & F. Moreno-Insertis, “Flux emergence at the photosphere”, in: J. Leibacher, H. Uitenbroek and B. Stein (eds.) *Solar MHD: Theory and Observations - a High Spatial Resolution Perspective*, ASP Conf. Ser., in press.
- M. Cheung, M. Schüssler & F. Moreno-Insertis, “3D magneto-convection and flux emergence in the photosphere”, in: D. Danesy (ed.) *Chromospheric and Coronal Magnetic Fields*, ESA SP-596.



# Acknowledgements

I would like to thank the Max Planck Institute for Solar System Research (MPS) and the International Max Planck Research School (IMPRS) for giving me the opportunity and the financial support to carry out the research presented in this dissertation.

I am indebted to my supervisors Prof. Manfred Schüssler and Prof. Fernando Moreno-Insertis (IAC, Tenerife) for their continued support, their patience and for all the stimulating discussions that nurtured my fascination of solar physics.

I wish to thank Prof. Franz Kneer for accepting me as his student at the University of Göttingen and for always being helpful. I have learned a great deal from my discussions with him.

I must thank the coordinator of the IMPRS, Dieter Schmitt, for keeping the research school in such good order. This is one fine place to do a PhD.

Special thanks goes to Alexander Vögler and Robert Cameron. Both have taken a barrage of questions from me about MHD and numerical codes. The occasional sarcastic comment spurred me on.

A big thank you and a big hug to all the nice people in Lindau. Lindau is bearable (even wonderful!) because of you. Tien and I will never forget the bouquet you gave us. I want to finish this dissertation so I can only name a few: Katerina, Durgesh, Fu, Hebe and Luciano, Shibu & Co., Monica and Martin T.

I thank my parents for their support through the years. I appreciate the freedom you have given me to pursue my studies in physics.

Finally, I want to thank my wife Tien for showing me all the love and support I need.



# Lebenslauf

Name: Chun Ming Mark Cheung

Geburt: Am 02.04.1982 in Hong Kong

Staatsbürgerschaft: Australisch

Schulbildung: 06/1996 bis 11/1998 Norwood Morialta High School, Adelaide  
South Australian Certificate of Education

Studium: 03/1999 bis 11/2002 Physikstudium an der University of Adelaide  
Bachelor of Science (Honours)  
Honours Dissertation:  
“Supernova remnants and the interstellar medium”

02/2003 bis 02/2006 Doktorarbeit  
Während dieser Zeit Tätigkeit als  
wissenschaftlicher Mitarbeiter am Max-Planck-  
Institut für Sonnensystemforschung  
in Katlenburg-Lindau